

**THE INFLUENCE OF MICROFILLER ADDITION ON THE FLEXURAL AND  
IMPACT BEHAVIOR OF CARBON FIBER REINFORCED PHENOLIC**

A Thesis Submitted to the  
College of Graduate and Postdoctoral Studies  
In Partial Fulfillment of the Requirements  
For the Degree of Master of Science  
In the Department of Mechanical Engineering  
University of Saskatchewan  
Saskatoon

By  
Ibraheem Adekunle Abdulganiyu

© Copyright Ibraheem Adekunle Abdulganiyu, October 2020. All rights reserved.  
Unless otherwise noted, copyright of the material in this thesis belongs to the author

## **PERMISSION TO USE**

In presenting this thesis in partial fulfillment of the requirements for a Postgraduate degree from the University of Saskatchewan, I agree that the Libraries of this University may make it freely available for inspection. I further agree that permission for copying of this thesis in any manner, in whole or in part, for scholarly purposes may be granted by Prof. Akindele Odeshi, the professor who supervised my thesis work or in his absence, by the Head of the Department or the Dean of the College in which my thesis work was done. It is understood that any copying or publication or use of this thesis or parts thereof for financial gain shall not be allowed without my written permission. It is also understood that due recognition shall be given to me and to the University of Saskatchewan in any scholarly use which may be made of any material in my thesis.

Requests for permission to copy or to make other uses of materials in this thesis in whole or part should be addressed to:

Head of the Department of Mechanical Engineering  
University of Saskatchewan  
57 Campus Drive  
Saskatoon, Saskatchewan S7N 5A9  
Canada.

OR

Dean  
College of Graduate and Postdoctoral Studies  
University of Saskatchewan  
116 Thorvaldson Building, 110 Science Place  
Saskatoon, Saskatchewan S7N 5C9  
Canada.

## ABSTRACT

In this study, the effects of microfiller addition on flexural and dynamic impact behavior of carbon fiber reinforced phenolic matrix composites were investigated. The composite materials were produced using 2D woven PAN-based carbon fibers and two variants of phenolic resins (HRJ-15881 and SP-6877). The resins have the same phenol and solid content but differ in their viscosities and HCHO (formaldehyde) content. Colloidal silica and silicon carbide (SiC) microparticles were used as fillers and were added to the phenolic matrix in four weight fractions; namely 0.5 wt.%, 1.0 wt.%, 1.5 wt.%, and 2.0 wt.%. Thermogravimetric analysis (TGA) was used for thermal analysis of the phenolic resins. The flexural properties were determined using a three-point bending test, while the dynamic impact properties were determined using the Split Hopkinson pressure bar (SHPB). The damage evolutions under both loading conditions were investigated using optical and scanning electron microscopy.

Thermal analysis results indicated that a cross-linking reaction occurred in both phenolic resins in the temperature range 110-130 °C and decomposition of the resin to form amorphous carbon began around 450 °C. The reinforcement of HRJ-15881 and SP-6877 phenolic resins with carbon fibers increased their flexural strength by 508% and 909%, respectively. The flexural strength of the carbon fiber reinforced phenolic (CFRP) composites further increased with the addition of SiC particles up to 1 wt.% SiC, but decreased with further increase in the amount of SiC particles added. On the other hand, the flexural modulus of the composites generally decreased with the addition of SiC microfiller. Both the flexural strength and flexural modulus of the composites did not improve with the addition of colloidal silica microfiller. The decrease in flexural properties was caused by the agglomeration of the microfillers at higher filler content, with colloidal silica particles exhibiting more tendency for agglomeration than SiC particles. Microscopic evaluation of the fractured specimens revealed fiber breakage, matrix cracking, and delamination under flexural loading. The tendency for cracking and fragmentation worsened at a microfiller loading of 1.5 wt.% and above.

Two impact momenta were applied in the dynamic impact testing of the fabricated CFRP: 15 kg m/s and 28 kg m/s. At an impact momentum of 15 kg m/s, the dynamic impact strength increased with SiC addition for HRJ-15881 resin up to 1.5 wt.% and up to 0.5 wt.% for SP-6877 resin. At an impact momentum of 28 kg m/s, the dynamic impact strength increased at all SiC addition for

SP-6877 resin, and up to 0.5 wt.% for HRJ-15881 resin. However, the impact strength deteriorated with colloidal silica addition for both phenolic resins and at both impact momentums. For CFRP with and without microfiller addition, no specimen fragmentation occurred at the impact momentum of 15 kg m/s. However, the CFRP without microfillers failed at an impact momentum of 28 kg m/s. Failure was observed to occur only in CFRP containing not more than 1 wt.% SiC addition. For composites containing colloidal silica addition, failure only occurred at a higher filler content of 2 wt.%. In all cases, with and without microfiller, the damage modes under the impact loading consist of fiber bundle rupture, matrix cracking, and delamination.

XRD analysis results suggested that the microfillers were intercalated in the phenolic matrix of the CFRP. The addition of the SiC microfiller improved the crystallinity of both neat (unreinforced) phenolics and CFRP, irrespective of the phenolic resin used. However, with colloidal silica addition, improvement in crystallinity was only obtained for the HRJ-1881 resin, and CFRP made with this resin. For the SP-6877 resin, there was a decrease in the crystallinity of the phenolic and the CFRP made with the colloidal silica.

## ACKNOWLEDGEMENTS

My sincere appreciation goes to my supervisor, Prof. Akindele Odeshi, for giving me the opportunity to undertake this M.Sc study under his tutelage. His unparalleled kindness, patience, time, insightful feedback, words of encouragement created an atmosphere that fostered learning and development, even beyond research work. The valuable contributions of my advisory committee members, Prof. Ike Oguocha, Prof. Shafiq Alam, and Prof. Jerzy Szpunar, are greatly appreciated. I thank Prof. Ike Oguocha for his insightful scientific contributions and valuable feedback in the course of carrying out this research project.

I would also like to thank Mr. Nan Fang Zhao, Dr. Majid Soleimani, and Dr. Ahmed Tiamiyu for their technical support in the form of training on the use of equipment. The support received from Prof. O.A Ojo of the University of Manitoba is deeply appreciated, and I am sincerely grateful to him for his help since coming to Canada for my graduate studies. I thank SI Group and Washington Mills for their support in providing me with the phenolic resins and SiC microfiller used in my research, respectively. The financial supports received from the University of Saskatchewan in the form of Graduate Teaching Fellowship (GTF), the Mechanical Engineering Devolved Scholarship, and the Graduate Students Association (GSA) bursary scheme are greatly appreciated.

The efforts of my loving parents, Alhaji and Alhaja A. Abdulganiyu, cannot be quantified. Thank you for being the wind beneath my wings, the prayers, and soothing words of love and encouragement. I beseech the Almighty God to grant you the strength and longevity to enjoy the fruits of your labor in good health. To my wonderful siblings; Bayonle, Adeola, and Eniola, I thank you for your love, support, and prayers.

To my wonderful friends: Raheem Elemuren, Emmanuel Adejumo, Ope Fadele, Taiwo Dada, Niyi Ajiteru, Mary Bajomo, Nnaemeka Ugodilinwa, Francis Amushi, Emmanuel Awoyele, Victor Adedeji, Felipe Serafim, Wahab Alabi, Kazeem Sulaiman, and Chao Peng, thank you for your contributions and moral support towards completion of my MSc program.

## **DEDICATION**

**To God,**

“Your Lord is going to give you beyond your imaginations, and you will be satisfied with it”

**To my loving parents,**

For the gift of education.

Truly, after patience, beautiful things await.

## TABLE OF CONTENTS

<b>PERMISSION TO USE.....</b>	<b>i</b>
<b>ABSTRACT.....</b>	<b>ii</b>
<b>ACKNOWLEDGEMENTS.....</b>	<b>iv</b>
<b>DEDICATION.....</b>	<b>v</b>
<b>TABLE OF CONTENTS.....</b>	<b>vi</b>
<b>LIST OF TABLES.....</b>	<b>ix</b>
<b>LIST OF FIGURES.....</b>	<b>x</b>
<b>LIST OF ABBREVIATIONS AND SYMBOLS.....</b>	<b>xiv</b>
<b>CHAPTER 1: INTRODUCTION.....</b>	<b>1</b>
1.1 Overview.....	1
1.2 Motivation.....	2
1.3 Research Objectives.....	3
1.4 Expected Research Contributions.....	4
1.5 Thesis Arrangement.....	4
<b>CHAPTER 2: LITERATURE REVIEW.....</b>	<b>5</b>
2.1 Composite Materials.....	5
2.2 Reinforcements.....	6
2.2.1 Particles.....	6
2.2.2 Whiskers.....	6
2.2.3 Fibers.....	6
2.3 Classification of Composite Materials.....	8
2.3.1 Metal matrix composites (MMCs).....	9
2.3.2 Ceramics matrix composites (CMCs).....	9
2.3.3 Polymer matrix composites (PMCs).....	10
2.4 Phenolic Resin and Phenolic Matrix Composites.....	11
2.4.1 Phenolic resin.....	11
2.4.2 Phenolic matrix composites.....	12
2.5 Manufacturing Process for Fiber-Reinforced Plastic.....	12
2.5.1 Filament winding.....	13

2.5.2	Pultrusion .....	13
2.5.3	Resin transfer molding .....	14
2.5.4	Autoclave processing .....	14
2.6	Damage in FRP Structures .....	15
2.7	Fillers.....	16
2.7.1	Carbon-based fillers .....	17
2.7.2	Metallic fillers .....	18
2.7.3	Ceramic fillers .....	19
2.8	Method of Fillers Dispersion .....	19
2.9	Evaluation of Filler Dispersion .....	20
2.10	Effect of Filler Addition on Properties of Phenolic Resin and Carbon Fiber Reinforced Phenolic.....	22
2.11	Applications of Carbon Fiber Reinforced Phenolic Matrix Composites.....	23
2.12	Summary .....	24
<b>CHAPTER 3: MATERIALS AND METHODOLOGY .....</b>		<b>25</b>
3.1	Materials .....	25
3.2	Manufacturing of Carbon Fiber Reinforced Phenolic .....	26
3.2.1	Dispersion of colloidal silica in phenolic resin .....	27
3.2.2	Dispersion of SiC in phenolic resin.....	27
3.2.3	Fabrication of carbon fiber reinforced phenolic .....	29
3.3	Materials Characterization .....	31
3.3.1	Thermogravimetric analysis .....	31
3.3.2	Fourier transform infrared spectroscopy analysis .....	31
3.3.3	X-ray diffraction (XRD).....	32
3.3.4	Flexural tests (3-point bending test).....	34
3.3.5	Dynamic impact test .....	36
3.3.6	Microstructure examination.....	38
3.3.7	Statistical analysis.....	41
<b>CHAPTER 4: RESULTS AND DISCUSSION .....</b>		<b>42</b>
4.1	Fourier-Transform Infrared Spectroscopy (FTIR).....	42
4.2	Thermal Analysis.....	44

4.3	Microstructural Examination of As Manufactured Carbon Fiber Reinforced Phenolic	.47
4.4	Flexural Properties	48
4.5	Dynamic Impact Properties	54
4.5.1	Dynamic impact response at impact momentum of 15 kg m/s	54
4.5.2	Dynamic impact response at impact momentum of 28 kg m/s	58
4.6	Statistical Analysis	61
4.7	X-ray Diffraction Analysis	62
4.7.1	Crystallinity	71
4.8	Fracture Analysis of the CFRP under Mechanical Loading	74
4.8.1	Three-point flexural loading	74
4.8.2	Dynamic impact loading	79
<b>CHAPTER 5: SUMMARY, CONCLUSIONS AND RECOMMENDATIONS</b>		<b>84</b>
5.1	Summary	84
5.2	Conclusions	85
5.3	Recommendations for Future Work	87
<b>REFERENCES</b>		<b>88</b>
<b>APPENDIX A</b>		<b>99</b>
	CALIBRATION OF THE SHPB	99
<b>APPENDIX B</b>		<b>102</b>
	RAMP AND SOAK PROGRAM OF THE AUTOCLAVE USED FOR THE CFRP	102

## LIST OF TABLES

Table 2.1	Common synthetic fibers: advantages and disadvantages.....	8
Table 3.1	Chemical analysis of the phenolic resins used in this study.....	26
Table 4.1	FTIR spectra functional group assignment.....	43
Table 4.2	Results of TGA showing mass loss (in %) of the phenolic resins with temperature increase.....	45
Table 4.3	ANOVA test results for flexural properties of the carbon fiber reinforced phenolic (CFRP) containing microfillers.....	62
Table 4.4	ANOVA test results for impact strength of the CFRP containing microfillers..	62
Table 4.5	Amorphous and crystalline fraction of cured resin and composites.....	73
Table 4.6	The results of the visual examination of impacted CFRP specimens showing whether fracture occurred or not.....	79
Table B.1	Ramp and soak program of the CFRP used for manufacturing.....	102

## LIST OF FIGURES

Figure 2.1	Classification of composite materials.....	9
Figure 2.2	Polymer classification and structures: (a) Thermosets (b) Thermoplastics ....	11
Figure 2.3	Different forms of distribution of filler particles in polymer resins: (a) inhomogenous and non-uniform distribution (b) fairly homogenous and fairly uniform distribution, and (c) uniform and homogenous distribution....	20
Figure 3.1	Manufacturing process flow chart for carbon fiber reinforced phenolic .....	26
Figure 3.2	Photograph showing stages in microfiller dispersion and CFRP manufacturing: (a) SiC microfillers (MF) (b) SiC MF + ethanol absolute (c) ultrasonication (d) phenolic resin added (e) ultrasonication, and (f) ultrasonicated mixture.....	28
Figure 3.2 continued	Photographs showing stages in microfiller dispersion and CFRP manufacturing: (g) magnetic stirring (h) homogenous mixture (i) mold sprayed with release agent (j) carbon fiber lay-up (k) phenolic resin infiltration, and (l) autoclave curing.....	29
Figure 3.3	Curing cycle for the carbon fiber reinforced phenolic.....	30
Figure 3.4	TA instrument Q5000 used in this study.....	31
Figure 3.5	Renishaw Raman InVia Raman microscope used in this study.....	32
Figure 3.6	Photograph of ground composite sample used for XRD in this study.....	33
Figure 3.7	Rigaku Ultima IV X-ray Diffractometer used in this study.....	33
Figure 3.8	Photograph of flexural test samples.....	34
Figure 3.9	Schematic representation of the geometry of the flexural test specimen and dimensions.....	34
Figure 3.10	Instron™ universal testing machine (Model 5500R) showing three-point bend testing of the composites.....	35
Figure 3.11	Schematic representation of the Split Hopkinson pressure bar used in this study.....	37
Figure 3.12	Photograph of dynamic impact test samples.....	38
Figure 3.13	Nikon eclipse MA 1500 microscope used in this study.....	39
Figure 3.14	Nikon optihot stereomicroscope used in this study.....	39

Figure 3.15	JEOL-JSM-6010LV scanning electron microscope (SEM) used in this study	40
Figure 3.16	Edward S150B sputter coater used in this study.....	40
Figure 4.1	FTIR spectra obtained for the cured phenolic resins.....	42
Figure 4.2	TG analysis of the as-received phenolic resins.....	44
Figure 4.3	DTG plots obtained for the as-received phenolic resins.....	45
Figure 4.4	TG analysis of cured phenolic resins.....	47
Figure 4.5	Optical micrographs of the manufactured carbon fiber reinforced phenolic matrix composite without fillers.....	47
Figure 4.6	SEM micrographs of the manufactured carbon fiber reinforced phenolic matrix composite without fillers.....	48
Figure 4.7	Flexural stress-strain curves for unreinforced cross-linked phenolic (a, b), carbon fiber reinforced phenolic without microfiller (c, d) and carbon fiber reinforced phenolic containing microfiller (e, f).....	49
Figure 4.8	Effect of carbon fiber reinforcement on (a) flexural strength and (b) flexural modulus of cross-linked phenolic resin.....	51
Figure 4.9	Flexural properties of CFRP composites with SiC microfiller addition: (a) flexural strength, and (b) flexural modulus.....	52
Figure 4.10	(a) flexural strength and (b) modulus of CFRP, with and without colloidal silica addition.....	53
Figure 4.11	SEM micrograph showing colloidal silica agglomeration in a CFRP containing colloidal silica microfiller.....	53
Figure 4.12	True stress-strain curve obtained for CFRPs without microfillers at an impact momentum of 15 kg m/s.....	54
Figure 4.13	True stress-strain curves obtained for CFRPs containing SiC microfiller at an impact momentum of 15 kg m/s: (a) HRJ-15881 (b) SP-6877.....	55
Figure 4.14	Maximum true stress obtained for CFRPs containing SiC microfillers at an impact momentum of 15 kg m/s.....	56
Figure 4.15	True stress-strain curves obtained for CFRPs containing colloidal silica microfiller at an impact momentum of 15 kg m/s: (a) HRJ-15881 (b) SP-6877.....	57

Figure 4.16	Maximum true stress obtained for CFRPs containing colloidal silica microfillers at an impact momentum of 15 kg m/s.....	57
Figure 4.17	True stress-strain curve obtained for CFRPs without microfillers at an impact momentum of 28 kg m/s.....	58
Figure 4.18	True stress-strain curves obtained for CFRPs containing SiC microfiller at an impact momentum of 28 kg m/s: (a) HRJ-15881 (b) SP-6877.....	59
Figure 4.19	Maximum true stress obtained for CFRPs containing SiC microfillers at an impact momentum of 28 kg m/s.....	59
Figure 4.20	True stress-strain curves obtained for CFRPs containing colloidal silica microfiller at an impact momentum of 28 kg m/s: (a) HRJ-15881 (b) SP-6877.....	60
Figure 4.21	Maximum true stress obtained for CFRPs containing colloidal silica microfillers at an impact momentum of 28 kg m/s.....	61
Figure 4.22	Calculated diffraction pattern obtained for graphite using different FWHM values.....	63
Figure 4.23	Comparison of diffraction pattern for calculated graphite (carbon) at FWHM of 4 and Experimental carbon fiber (Exp. CF).....	64
Figure 4.24	Calculated X-ray pattern of $\alpha$ -SiC obtained from American mineralogy crystal structure database (AMCSD) compared with that of the SiC used in the present study (Exp. SiC).....	65
Figure 4.25	XRD diffractograms showing constituent materials for CFRP composite made with (a) HRJ-15881 and (b) SP-6877 phenolic resin.....	66
Figure 4.26	XRD diffractograms showing the effect of SiC microfiller addition on the CFRP composite made with (a) HRJ-15881 and (b) SP-6877 phenolic resin..	67
Figure 4.27	XRD diffractograms showing the effect of colloidal silica microfiller addition on the CFRP composite made with (a) HRJ-15881 and (b) SP-6877 phenolic resin.....	68
Figure 4.28	XRD diffractograms showing the effect of SiC microfiller addition on the resins: (a) HRJ-15881 and (b) SP-6877 phenolic resin.....	69
Figure 4.29	XRD diffractograms showing the effect of colloidal silica microfiller addition on the resins: (a) HRJ-15881 and (b) SP-6877 phenolic resin.....	70

Figure 4.30	Determination of the percentage crystallinity and amorphous from an XRD diffractogram of CFRP made with SP-6877 without microfillers.....	71
Figure 4.31	Optical micrograph showing damage in a composite test specimen containing no microfiller under three-point flexural loading.....	75
Figure 4.32	Optical micrograph showing damage in flexural test samples with SiC addition.....	75
Figure 4.33	SEM micrograph showing damage in flexural test samples containing 0.5 wt.% SiC.....	76
Figure 4.34	SEM micrographs showing detailed damage in flexural test samples containing 0.5 wt.% SiC.....	77
Figure 4.35	SEM micrograph showing damage in flexural test samples containing 2 wt.% SiC.....	78
Figure 4.36	SEM micrographs showing detailed damage in flexural test samples containing 2 wt.% SiC.....	78
Figure 4.37	Optical macrographs showing impact failure of CFRP without microfillers; impacted at 28 kg m/s.....	80
Figure 4.38	Optical macrograph showing impact failure of CFRP composite containing 0.5 wt.% SiC; impacted at 28 kg m/s.....	80
Figure 4.39	Optical macrograph showing impact failure of CFRP composite containing 2wt.% colloidal silica; impacted at 28 kg m/s.....	81
Figure 4.40	SEM fractographs obtained for CFRP without fillers after fracture under impact loading (28 kg m/s).....	82
Figure 4.41	SEM fractographs obtained for CFRP composite containing 0.5 wt.% SiC after fracture under impact loading (28 kg m/s).....	82
Figure 4.42	SEM fractographs obtained for CFRP composite containing 2 wt.% colloidal silica after fracture under impact loading (28 kg m/s).....	83
Figure A.1	Calibration raw data from oscilloscope at firing pressure of 50 kPa.....	100
Figure A.2	Computed conversion factor of voltage to strain amplitude at different impact pressures.....	101

## LIST OF ABBREVIATIONS AND SYMBOLS

### ABBREVIATIONS

ASTM	American society for testing and materials
CF	Carbon fiber
CFRP	Carbon fiber reinforced phenolic
CMC	Ceramic matrix composite
CNT	Carbon nanotubes
CNF	Carbon nanofibers
cP	Centipoise
cps	Counts per second
CVD	Chemical vapor deposition
C/C	Carbon-carbon composite or carbon fiber reinforced carbon
1D	One dimensional
2D	Two dimensional
3D	Three dimensional
DTG	Derivative thermogravimetry
DWCNTs	Double wall carbon nanotubes
FRP	Fiber reinforced polymer/fiber reinforced plastic
FST	Fire smoke and toxicity
FTIR	Fourier transform infrared spectroscopy
h	Hour(s)
IM	Impact momentum (kg m/s)
MMC	Metal matrix composite
MWCNTs	Multi-wall carbon nanotubes
min.	Minutes
PIP	Polymer infiltration and pyrolysis
PMC	Polymer matrix composite
rpm	Revolutions per minute
RT	Room temperature
SEM	Scanning electron microscope/microscopy
TEM	Transmission electron microscope/microscopy

SHPB	Split Hopkinson pressure bar
SiC	Silicon carbide
SWCNTs	Single-wall carbon nanotubes
TGA	Thermogravimetric analysis
wt.	Weight
XuM	X-ray Ultra microscopy
XRD	X-ray Diffraction

## SYMBOLS

$A_B$	Cross-sectional areas of the incident and transmitted bars ( $\text{mm}^2$ )
$A_S$	Area of the dynamic impact test specimens ( $\text{mm}^2$ )
$C_B$	Velocity of elastic waves in the incident and transmitted bars
$E_B$	Elastic modulus of the incident and transmitted bar (GPa)
$\sigma_f$	Flexural stress (MPa)
$E_f$	Flexural modulus (GPa)
$b$	Flexural sample width (mm)
$d$	Flexural sample thickness (mm)
$L$	Length of support span (mm)
$m$	Slope of the tangent to the initial straight-line portion of the load-deflection curve (N/mm)
$P$	Flexural load (N)
$R$	Rate of crosshead motion (mm/min)
$\frac{s}{d}$	Span to depth ratio
$\sigma_n$	Nominal stress (MPa)
$\varepsilon_n$	Nominal strain
$\dot{\varepsilon}_n$	Nominal strain rate ( $\text{s}^{-1}$ )
$\sigma_t$	True stress (MPa)
$\varepsilon_t$	True strain
$\dot{\varepsilon}_t$	True strain rate ( $\text{s}^{-1}$ )
$\varepsilon_T$	Transmitted strain pulses
$\varepsilon_R$	Reflected strain pulses

$\varepsilon$	Dynamic impact strain amplitude
$L_s$	Initial length of the dynamic impact test specimen (mm)
$N$	Number of carbon fiber fabric layers for flexural test
$M$	Number of carbon fiber fabric layers for dynamic impact test
$t$	Time (s)
%	Percentage
$V_{st}$	Velocity of the striker bar (m/s)
$Z$	Rate of straining of the outer fiber (mm/min)

# CHAPTER 1

## INTRODUCTION

### 1.1 Overview

Carbon fiber reinforced polymer matrix composite materials are attractive for many engineering applications due to their low density and high specific strength. They are composed of two basic constituents: reinforcement and matrix. The reinforcement provides the strength, whereas the matrix holds and supports the reinforcement while also preventing them from environmental degradation. Polymeric materials used in fabricating fiber-reinforced composites include epoxy, phenolic, polyester, and polyurethane [1]. Carbon, Kevlar, and glass fibers are the popular fibers commonly used in polymer reinforcement [1], [2]. The focus of the current research is on carbon fiber reinforced phenolic matrix composites in which the reinforcement is woven carbon fiber fabrics that are embedded in a phenolic matrix.

Phenolic resins are formed by condensation reaction between phenol and formaldehyde. They have remained a candidate matrix material for the fabrication of fiber-reinforced plastics for structural applications for over 90 years [3], [4]. There are two categories of phenolic resins, namely: resoles and novolaks. Resoles are the preferred phenolic resin for the manufacture of fiber-reinforced polymer matrix composites, while novolaks are preferred for phenolic molding materials [4]. Carbon fiber reinforced phenolics composites have found widespread application as structural materials in aeronautical and space industries. This is due to their excellent combination of properties such as high specific strength and stiffness, low density, low thermal expansion, high thermal stability, excellent flame retardant properties, production of nontoxic combustion products, and relatively low cost [3], [5], [6].

Phenolic resins have suitable viscosities for the impregnation of fiber preforms to produce high strength composites. They also possess a carbon yield high enough to produce carbon-carbon (C/C) composite when the carbon fiber reinforced phenolic is pyrolyzed [5], [7]. This method of producing carbon-carbon composite using carbon fiber and phenolic resin as the raw material is called polymer infiltration and pyrolysis (PIP) process. The PIP method is a three-stage process that starts with the manufacture of carbon fiber reinforced phenolic using phenolic resins as the carbon precursor. The second stage involves pyrolysis of the carbon fiber reinforced phenolic to convert the phenolic resin to amorphous carbon. Evaporation of the volatile content of the phenolic

resin leads to a porous C/C composite, which is densified in the final stage by repeated cycles of impregnation with precursor resins and subsequent pyrolysis. The mechanical properties of carbon/carbon composites produced by pyrolysis of carbon fiber reinforced phenolics can be enhanced by enhancing the mechanical properties of the carbon fiber reinforced phenolics before pyrolysis.

The mechanical performance of fiber-reinforced plastics can be enhanced by dispersing fillers in the polymer matrix [8]. However, the main drawback with the addition of fillers is their agglomeration, which occurs as they adhere to one another due to the van der Waals forces between the filler particles [8]–[10]. However, in literature, the incorporation of fillers in the matrix of composite materials has resulted in considerable improvement in the ablation resistance of carbon fiber reinforced phenolic matrix composites [11]–[19]. Improvements in wear properties of carbon fiber reinforced phenolics composites as a result of filler addition have been reported [20], [21]. Other researchers [10], [22], [23] also reported improvement in flexural properties of phenolic due to filler addition. In most cases, the filler content was less than 3 wt.%. At higher filler contents, these properties started to deteriorate.

Examples of materials that have been used as fillers in polymer and polymer-based composites include; carbon nanotubes (CNTs), silica, graphite, fly ash, titanium dioxide, nanoclay, and alumina [24]–[26]. In this study, silicon carbide (SiC) and colloidal silica were used as filler materials. SiC has excellent properties such as high-temperature oxidation resistance, thermal shock resistance, superior wear properties, and considerable electron mobility [27]. As a result, they are used in high-temperature applications such as rocket injector grooves and nanodevice applications such as semiconductor wafer. Colloidal silica has excellent wear resistance and is used in the manufacture of silicon wafers and ceramic coatings [28].

## **1.2 Motivation**

The use of phenolic materials for ballistic protective body armors dates back to the 1960s. One of the first matrix material systems qualified for protective body armors was phenolic resin blended with polyvinyl butyral (PVB) resin [3]. DeBell & Richardson Inc. originally developed this polyblend resin system for nylon helmet liners in the early 1960s, the polyblend resin system was made by mixing the two components in 1:1 ratio by weight. When phenolic is used as the matrix material in fiber-reinforced composites, the resulting composites have found applications as floor

panels of aircraft, cabin furnishings, and engine compartments [29]. However, aircrafts structures experience bending loads, accidental damage in the form of integrated parts, and suckling of runaway debris into the engine, with velocities of 100 – 150 m/s and impact energies of over 100 J [30]–[32], posing a serious challenge to aircraft's structural integrity. When carbon fiber reinforced phenolic is used in manufacturing carbon/carbon composites for leading edges and nose cones of space shuttles, considerable resistance to impact failure is very crucial considering the space shuttle Columbia disaster on February 1, 2003. This was caused by impact failure of the leading edge of the space vehicle by falling insulating foam during take-off [33]. It is therefore, crucial to enhance the dynamic impact resistance of carbon fiber reinforced phenolic composites that will be used in producing carbon/carbon composites.

The incorporation of fillers to improve the ablation resistance [11]–[19] and wear properties [20], [21] of carbon fiber reinforced phenolics composites have been explored. Other authors have also attempted to improve the flexural properties of phenolic resin with fillers addition [10], [22], [23]. However, there is limited or no information on how the flexural and dynamic impact properties of carbon fiber reinforced phenolic composites can be improved with fillers addition. Obviously, there is a great need to develop carbon fiber reinforced phenolic composite with superior service lives and long-term durability. So, an understanding of their performance is essential. This study aims to provide additional knowledge in this field through the investigation of the flexural and dynamic impact properties of carbon fiber reinforced phenolic composites in which microfillers of colloidal silica and silicon carbide have been added.

### **1.3 Research Objectives**

The goal of the present study was to develop carbon fiber reinforced phenolic composites with improved resistance to failure under dynamic impact and flexural loading conditions. This is very important whether the carbon fiber reinforced phenolic is intended for structural application or for use as the base material in the manufacture of carbon/carbon composites. This was achieved through the following specific objectives:

1. Optimize process parameters for manufacturing carbon fiber reinforced phenolic matrix composites.

2. Determine the effects of filler (colloidal silica and SiC) addition on the flexural and dynamic impact properties of carbon fiber reinforced phenolic matrix composites.
3. Determine the influence of filler addition on the failure mode of the manufactured carbon fiber reinforced phenolic matrix composites under flexural and impact loading.

#### **1.4 Expected Research Contributions**

Material property data generated from the study of the effects of filler addition on dynamic impact properties of carbon fiber reinforced phenolic composites are a major contribution to knowledge, since most available data in the literature are mainly on flexural data.

#### **1.5 Thesis Arrangement**

The current chapter, Chapter 1, provides an overview, the motivations, and the objectives of this research. A summary of a literature survey on the previous works by other researchers in the areas related to this study is provided in Chapter 2. Chapter 3 contains detailed information on the materials and methods used in this study. The obtained experimental results are presented and discussed in Chapter 4, while Chapter 5 includes the summary and conclusions drawn from this study. Recommendations for future research are also included in Chapter 5.

## CHAPTER 2

### LITERATURE REVIEW

This chapter contains a literature review on composite materials, their constituents, and classifications, different techniques for manufacturing fiber-reinforced plastics (FRP), damage modes in FRP. Materials used as fillers, fillers dispersion, and their characterization techniques in FRP composites are also discussed. The effects of fillers addition on phenolic and carbon fiber reinforced phenolic matrix composites and the structural applications of carbon fiber reinforced phenolic are also covered in this chapter.

#### 2.1 Composite Materials

A composite material is a combination of two major constituents that results in better properties than those of the individual constituent used alone. The two major constituents of composites are the matrix and the reinforcement. The reinforcement provides strength and stiffness while the role of the matrix is to bind the reinforcement together and protect them from environmental induced degradation. The reinforcement in composite materials is usually fiber, whiskers, or particles [34], [35]. In fiber reinforced composite, the matrix aids in load transfer to the fibers [34], [36], [37]. Owing to the chemical interactions of the reinforcement and matrix, an additional phase exists between them called interface [36]. The reinforcement-matrix interface plays an important role in controlling failure mechanisms and the overall stress-strain behavior of the composite material [35], [36]. The overall properties of the composite material depend on the properties of the reinforcement and matrix, as well as the interface between them [36].

The advantages of fiber reinforced plastic (FRP) composite materials are their high specific strength and stiffness, which allow for a weight reduction in the finished parts [1], [6], [35], [37]. For example, commercial airline manufacturers have shown increasing interest in FRPs, as it is possible to reduce the weight of aircrafts, thereby increasing payload and fuel efficiency [34], [35]. Reduction of 0.453 kg mass in a commercial aircraft can save up to 360 gals (1360 l) of fuel per year, and fuel expenses alone account for 25% of the total operating costs of a commercial airline [34]. Hence, the use of FRPs in commercial airlines offers significant cost savings, coupled with overall weight reduction and shorter travel times.

## 2.2 Reinforcements

The basis of the superior performance of FRP composites lies in the high specific strength (strength to density ratio) and high specific stiffness (modulus to density ratio), these two properties are controlled by the reinforcements [36]. As mentioned earlier, the reinforcements in composite materials are usually fiber, whiskers, or particles [34], [35].

### 2.2.1 Particles

Particles have dimensions that are approximately equal in all directions and they may be spherical, platelets, or any other regular or irregular geometry [35]. Particles tend to be much weaker and less stiff than fibers, but they are usually much less expensive [38]. Particulate reinforced composites usually contain less reinforcement due to processing difficulties and brittleness [35]. Chandranohan *et al.* [39] used natural particles as reinforcements to manufacture composite. In their work, hybrid of powdered coconut shell, walnut shell, and rice husk was used as particle reinforcements with bio epoxy resin as the matrix. The authors reported that the particle hybrid reinforced polymer composite had better tensile, flexural, and shear strength than fiberglass reinforced polymer composite.

### 2.2.2 Whiskers

Whiskers diameters have a similar diameter to fibers but their lengths are short relative to fibers [1]. The length to diameter ratio ( $l/d$ ), known as the aspect ratio is short for whiskers relative to fibers. A major drawback of whiskers is that they are too expensive to manufacture and cannot be oriented easily [34], [37]. For example, the average cost to purchase silicon carbide whiskers cost \$95/lb, while that of silicon carbide particles cost \$3/lb [38].

Ryan *et al.* [40] reinforced high-density polyethylene (HDPE) with two different types of whiskers separately; synthetic hydroxyapatite (HA) whiskers and a commercially available HA spherical powder. The authors reported that the composites reinforced with the synthetic HA whiskers had higher elastic modulus, ultimate tensile strength, and work to failure relative to the composites reinforced with the commercially available spherical HA powder.

### 2.2.3 Fibers

Fibers have mostly circular cross-section and a length that is much greater than its diameter. Fibers are classified either as continuous or discontinuous based on aspect ratio and orientation [35]. Continuous fibers have high aspect ratios and preferred orientation, while discontinuous fibers

have small aspect ratios and are randomly oriented in composites reinforced with whiskers. Examples of continuous fibers include unidirectional fibers and woven fiber fabric, while examples of discontinuous reinforcements are chopped fibers and random mat [35], [36]. Fibers are categorized either as artificial (synthetic) or man-made (natural).

#### **2.2.3.1 Natural fibers**

Examples of natural fibers are jute, flax, hemp, sisal, coconut fiber (coir), and banana fiber (abaca). All these fibers are grown as agricultural plants in various parts of the world and are commonly used for making ropes, carpet backing, and bags. The components of natural fibers are cellulose micro-fibrils dispersed in an amorphous matrix of lignin and hemicellulose [41]. Depending on the type of the natural fiber, the cellulose content can be in the range of 60 – 80 wt.%, and the lignin content in the range of 5–20 wt.% [41]. Also, the moisture content in natural fibers can be up to 20 wt.%.

Even though natural fibers are easily accessible, however, they have several limitations. Natural fibers have low tensile strength, low melting points, and readily absorb moisture [41]. Furthermore, at temperatures higher than 200 °C, natural fibers start to degrade, first by the degradation of hemicellulose and then by the degradation of lignin. The degradation leads to odor, discoloration, the release of volatiles, and deterioration of mechanical properties of composites reinforced with natural fibers.

#### **2.2.3.2 Synthetic fibers**

Synthetic fibers are man-made fibers and are used as reinforcements in composite materials for high-performance structural applications. Synthetic fibers have high strength and stiffness, low density, and can be tailored to meet service requirements in terms of mechanical properties due to vast possibilities of fiber orientations and ability to withstand high temperatures when compared to natural fibers [36]. Synthetic fibers are also unaffected by microorganisms and environmental factors like moisture, sunlight, and stains.

There is a large variety of synthetic fibers available as reinforcement for composite materials, as shown in Table 2.1. Each type of synthetic fiber offers its advantages and disadvantages, however, the most desirable characteristics are high strength and high stiffness [35], [41]. Carbon fibers are the most common reinforcements in high-performance composite structures as they offer the best

combination of properties such as superior tensile and compressive strength, high moduli, excellent fatigue, and chemical/corrosion resistance [35]. The carbon fiber reinforcement can either be polyacrylonitrile-based (PAN-based), pitch-based, or rayon-based [1],[42]. PAN-based carbon fibers have higher tensile strength, modulus, failure strain, low density, and low coefficient of thermal expansion in comparison to rayon and pitch-based carbon fibers [1], [35], [43]. Hence, PAN-based carbon fibers are the most common carbon fibers in the manufacture of fiber reinforced plastics.

Table 2.1. Common synthetic fibers: advantages and disadvantages. [36]

Fiber	Advantages	Disadvantages
E-glass, S-glass	High strength	Low stiffness
	Low cost	Short fatigue life
		High-temperature sensitivity
Aramid (Kevlar)	High tensile strength	Low compressive strength
	Low density	High moisture absorption
Boron	High stiffness	High cost
	High compressive strength	
Carbon	High strength	Moderately low cost
	High stiffness	
Ceramic (silicon carbide, alumina)	High stiffness	Low strength
	High use temperature	High cost

### 2.3 Classification of Composite Materials

Composites can be classified into broad categories according to the matrix used (Fig. 2.1). The matrix could either be metal, ceramic, or polymer [36]. The properties of the matrix determine the maximum usage temperature, resistance to moisture and fluids, thermal and chemical stability [5], [34], [35].

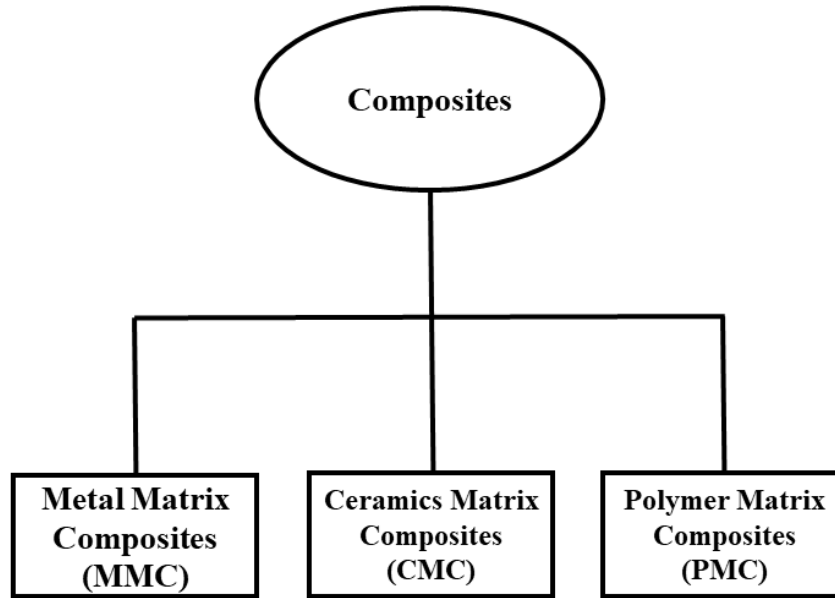


Figure 2.1. Classification of composite materials.

### 2.3.1 Metal matrix composites (MMCs)

They consist of metals or alloys (aluminum, magnesium, titanium, and copper) reinforced with boron, carbon, or ceramic fibers/whiskers. Ceramic particles are also often used to reinforce light alloys to increase their stiffness. Metals are mainly reinforced to alter their properties to suit the meet design requirements for structural applications [34]. For example, elastic stiffness and strength of metal can be increased, while the high coefficients of thermal expansion and electrical conductivities of metals can be reduced by the addition of fibers such as silicon carbide [34]. Their maximum use temperature is limited by the softening or melting temperature of the metal matrix [36].

### 2.3.2 Ceramics matrix composites (CMCs)

CMC consist of fibers embedded in ceramic matrices (silicon carbide, aluminum oxide, glass-ceramic, and silicon nitride). Originally, ceramics by themselves have low fracture toughness, under tensile or impact loading and they fail catastrophically [35], [36]. One of the reasons for reinforcing ceramics is to increase their fracture toughness [34]. CMC is best suited for applications where excellent mechanical properties and extreme service temperatures are desired. For example, NASA [44], developed a CMC that could be used as a hot component in gas turbine engines, heat exchangers, thermal protection systems, and turbo-pump components for space

vehicles. The CMC was made of non-oxide SiC fiber embedded in a SiC matrix, that can withstand adverse structural and environmental conditions for long times at temperatures up to 1500 °C.

### **2.3.3 Polymer matrix composites (PMCs)**

Polymer matrices are classified as either thermosets or thermoplastics [34], [35]. Thermosets are low-molecular-weight, low- viscosity monomers that are converted during curing into a three-dimensional (3D) cross-linked structure which is infusible and insoluble [5], [6], [35]. Cross-linking (Fig. 2.2(a)) results from chemical reactions that are driven by heat generated either by the chemical reactions themselves (i.e. exothermic heat of reaction) or by externally supplied heat. As curing progresses, the reactions accelerate, and the available volume within the molecular arrangement decreases, resulting in less mobility of the molecules and an increase in viscosity. After the resin gels and forms a rubbery solid, they cannot be re-melted. Thermosets are generally brittle and have low toughness. Reinforcement with fibers significantly improves their toughness and expand their load-bearing applications in engineering. Thermoset composite matrices include polyesters, vinyl esters, epoxies, bismaleimides, cyanate esters, polyimides, and phenolics, while examples of thermoplastics are Polyetheretherketone (PEEK), polyphenylene sulfide (PPS) and polypropylene (PP) and Polyetherimide (PEI) [1], [6], [35], [37].

In contrast to thermosets, thermoplastics (Fig. 2.2(b)) are high molecular weight polymers that do not chemically cross-link with heat. After forming a rubbery solid, they can be reheated for forming or joining operations. Due to their inherently high viscosity in comparison to thermosets, high temperatures and pressures are normally required for processing, or as recommended by the manufacturer [35]. Thermoplastic materials have low stiffness, which hinders their structural applications in areas where high rigidity is a requirement. Reinforcing thermoplastic materials will impart the required stiffness for load-bearing applications in engineering structure.

An ideal structural material would have high strength, high stiffness, high toughness, excellent creep resistance, and low weight. Fiber-reinforced polymer (FRP) composites meet these criteria in addition to low density, which makes their specific strength and stiffness to be higher than those of most structural materials. For example, the high specific strength and specific modulus offered by FRP composites are higher than those of comparable aerospace metallic alloys, e.g., aluminum (7075-T6) and Titanium (Ti-6Al-4V) [35]. This translates to greater weight savings resulting in

improved performance, longer range, and fuel savings when used as structural materials in aircraft manufacture.

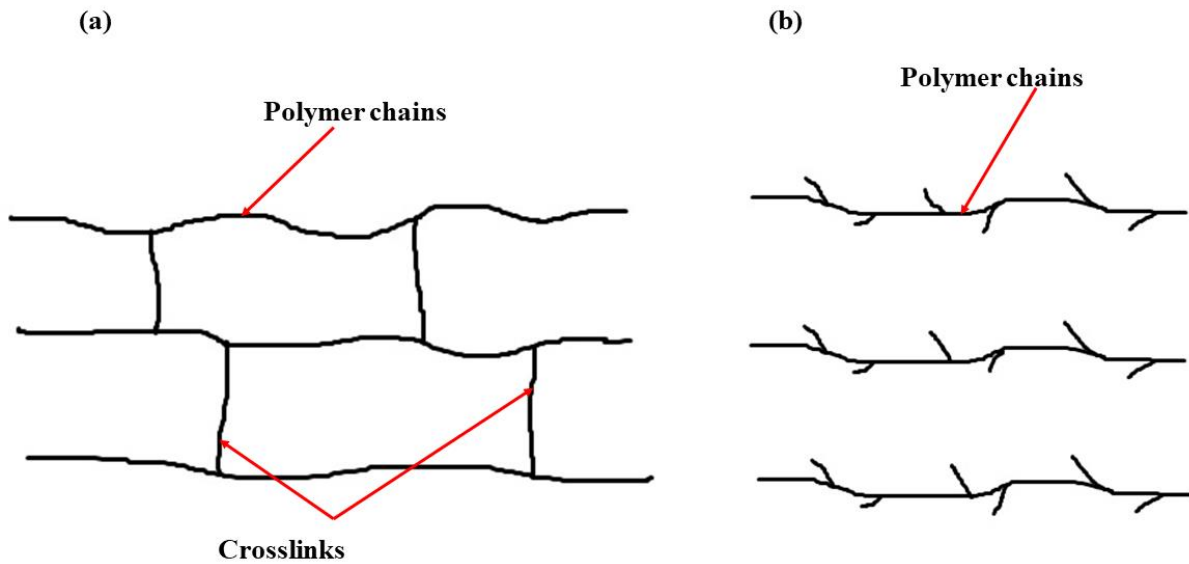


Figure 2.2. Polymer classification and structures: (a) Thermosets and (b) Thermoplastics.

## 2.4 Phenolic Resin and Phenolic Matrix Composites

### 2.4.1 Phenolic resin

Phenolic resin is synthesized from the reaction of phenol and formaldehyde, and are categorized into two: Resole and Novolac [45]. Phenolic resole are synthesized by the reaction of an excess of formaldehyde with phenol in the presence of a basic catalyst. The excess formaldehyde helps produce a sufficient number of active methylol groups during polymerization and helps cure the resin without the need for curing agents. For phenolic novolac resins, they are synthesized by the reaction of an excess (molar) of phenol with formaldehyde in the presence of an acidic catalyst. This reaction produces an insufficient methylol for curing to occur, and require an external curing agent. Hexamethylenetetramine is the common curing agent used for curing the phenolic novolac resin [45]. Resoles are the preferred phenolic resin composition for the manufacture of fiber-reinforced polymer composites, while novolak is the preferred resin for phenolic molding materials [4].

### **2.4.2 Phenolic matrix composites**

Phenolic resins have found widespread applications in structural applications owing to their excellent mechanical properties (when reinforced with fibers), good thermal resistance, excellent flame retardant properties, production of nontoxic combustion products, and relatively low cost [3]. Phenolic resins have demonstrated superior Fire, Smoke, and Toxicity (FST) properties relative to other polymers, as they produce low smoke and less toxic by-products upon combustion [4], [45], [46]. The global phenolic matrix composites market is dominated by the use in aircraft (interiors) and mass transit (buses, railways) industries [4], [45]. For example, when phenolics resins are reinforced with carbon fibers, they are used as aircrafts decks and cabin furnishings [29]. The use of the carbon fiber reinforced phenolic composites in these applications is because of the combination of the strength and stiffness that carbon fibers offer coupled with the production of nontoxic combustion products from the phenolics in case of fire outbreak. The success of phenolics in these areas is a reflection of the perspective to use fire-safe materials in confined-space for human occupancy. The FST properties of phenolic resins are the primary factors that drive the selection of these products in many applications. There is no other matrix material available, which provides the same FST performance at a comparable price [45].

### **2.5 Manufacturing Process for Fiber-Reinforced Plastic**

Manufacturing of fiber-reinforced plastic (FRP) starts with the arrangement of a large number of single fibers, fiber bundles, or fabrics into fiber preform to form a lamina (ply/layer) [1], [5], [35], [37]. In continuous fibers reinforced polymers, the fibers may be arranged either in a unidirectional orientation, in a bidirectional orientation, or a multidirectional orientation (i.e., fibers in more than two directions) [41]. Although the fibers provide the main source of strengthening for polymer matrix composites, the type of the polymeric matrix and their properties generally control the manufacturing and processing methods [35].

Broadly, one can divide the manufacturing processes into three different categories depending on the type of fibers and type of polymer [37]. The first category deals with FRP composites that contains thermoplastic materials which are in the form of pellets with discontinuous short or chopped fibers [37]. In such cases, once the thermoplastic polymer is melted, the fibers and the resin, mix and flow together as a suspension, either into a mold or through a die. Processes such as extrusion, injection molding, and compression molding fall under this category [37]. The

second category involves discontinuous or continuous fibers pre-impregnated with thermoplastic resin [37]. In such cases, heat and pressure are applied to form and consolidate the composite part. Thermoplastic sheet forming, thermoplastic pultrusion, and fiber tow placement processes fall under this category [37].

The third category involves thermosets of low viscosity resins and continuous fibers in the form of aligned, woven, or stitched fibers. In almost all thermoset resins, the manufacturing approach uses resin infiltration into a porous network of fibers [35], [37], [41]. The application of heat is vital, as this cross-links the resin, rapidly changes the viscosity and consolidates the composite. Resin transfer molding, thermoset pultrusion, thermoset filament winding, and autoclave processing are examples of such manufacturing processes [37].

### **2.5.1 Filament winding**

In the filament winding process, fibers are drawn through an in-line resin bath and wound over a rotating mandrel. [1], [35]. A large number of fiber (rovings) are pulled from a series of creels into a liquid resin bath containing the liquid resin. Fiber tension is controlled using the fiber guides located between each creel and the resin bath. Just before entering the resin bath, the rovings are usually gathered into a band by passing them through a textile thread board or a stainless steel comb. At the end of the resin tank, the resin-impregnated rovings are pulled through a wiping device that removes the excess resin from the rovings and controls the resin coating thickness around each roving. Once the rovings have been thoroughly impregnated and wiped, they are gathered together in a flat band and positioned on the mandrel. The angle of the roving band for the mandrel axis is called the wind angle and the winding could be hoop, helical, or polar [1], [37]. After winding several layers to generate the desired thickness, the filament wound part is generally cured on the mandrel and the mandrel is then extracted from the cured part. Filament winding is generally used for making pipes and tanks to handle chemicals, automotive drive shafts, helicopter blades, oxygen tanks, pipelines, spherical pressure vessels, conical rocket motor cases, and large underground gasoline storage tank [34], [41].

### **2.5.2 Pultrusion**

Pultrusion is a process for producing continuous lengths of reinforced plastic shapes with a constant cross-sectional area [1]. The reinforcing fiber is typically pulled through a heated resin bath and then formed into specific shapes as it passes through one or more forming die. The

forming die shapes the material and removes the excess resin before entry into the pultrusion die. The material then takes its net shape and cures in the pultrusion die. After the structure cools down, it is clamped and the flying saw moves along the clamped section to cut into the desired length. Pultrusion yields smooth finished parts, and it is mostly used for consistent solid and hollow structures like beams and pipes [35], [37].

### **2.5.3 Resin transfer molding**

In the resin transfer molding (RTM) process, the resin is injected under low pressure into a closed mold that contains the fiber preform [1], [35], [41]. Several layers of fibers (forming the fiber preform) are placed in the bottom half of a two-part mold, the mold is closed, and liquid resin is injected into the mold via a centrally located sprue. The resin injection point is usually at the lowest point of the mold cavity and the injection pressure is in the range of 69-690 kPa (10–100 psi) [41]. As the resin flows and spreads throughout the mold, it fills the space between the fiber in the dry fiber preform, displaces the entrapped air through the air vents in the mold, and coats the fibers. Depending on the type of the resin used, curing is performed either at room temperature or elevated temperature. After the cured part is pulled out of the mold, the part at the outer edges is trimmed to conform to the required dimensions.

### **2.5.4 Autoclave processing**

Autoclave processing is one of the oldest composites processing technologies and it is used to make complex shapes and flat panels for structures where high quality is desired [35], [37]. In this process, the required number of fibers are hand lay-up, one layer at a time or by an automated means on a mold surface, and resin is infiltrated into the mold cavity if the fibers are not already pre-impregnated with the resin before lay-up in the mold. The whole assembly is placed in an autoclave, where heat and pressure are applied in an inert gas atmosphere. The autoclave is a large pressure vessel with an integral heating element, or better still, an oven that can be pressurized [41]. The main function of the autoclave is to provide the heat and pressure required to consolidate and cure the composite structures. The high pressure and temperature in the autoclave allow the fiber preform to become a single coherent structure by forcing out air pockets, volatiles, and excess resin. The temperature and pressure requirements are determined by the kind of resin used [41]. For example, for high-temperature thermoset resins such as polyamides, the temperatures required could be in the range of 300-400 °C and pressure requirements may exceed 1 MPa [41].

## 2.6 Damage in FRP Structures

The manner in which FRP composites deform and fracture depends upon the mechanical and the chemical properties of its constituents (fiber, matrix, and fiber-matrix interface) and the loading conditions [30], [47]. A strong fiber-matrix interface is required for a good mechanical response of FRP. If the bond strength is too high, the resulting composite fails catastrophically with little or no delamination or debonding that can slow down or arrest crack propagation. If interfacial strength is too low, the composites will delaminate and fail in pure shear [6].

To investigate the failure mechanisms and modes in FRP composites, optical and scanning electron microscopes are usually used [48]. FRP composite experience damages such as intra-laminar matrix cracking, longitudinal matrix splitting, delamination, fiber fracture, fiber-matrix debonding, and fiber pull out [48], [49]. It is pertinent to note that out of these failure modes, the failure mode that involves the fracture of the matrix or interphase region requires low energy to fracture whereas failures involving fiber fracture require higher energy to fracture [48].

Most aircraft structures are of stiffened thin-walled types, e.g. wings, fuselage, and doors, which are often manufactured using FRP composite [50]–[52]. In these aerospace structures, the dynamic interactions between the structure and their surrounding mediums are significant and these interactions lead to a vast number of failure modes that need to be considered in the design process [30]. Before FRP composites are used, an important consideration is their behavior under different loading conditions such as impact and flexural. FRP composites used in aircraft structures such as deck and bulkhead are often subjected to all kinds of out-of-plane bending loads in service [30]. Impact damage is also greatly considered for the design and maintainability of aircraft composite structures, as they have a significant effect on the strength, durability, integrity, and stability of structural materials [53]. Impact damage are categorized into low velocity (low-velocity/low mass) and high velocity (low-velocity/high mass, high-velocity/low mass or high-velocity/high mass) [47], [51].

Low-velocity impact damage in aircraft structures is due to both operational and maintenance activities [53]. In the operational environment, the low-velocity impact damage is due to hailstone strikes and foreign object damage such as runway debris. For the maintenance activities, the low-velocity impact damage is due to aircraft part transportation, handling, and storage and incidental

tool drops [53]. In the low-velocity impact loading, the time of contact between the projectile and the target is relatively long, so, the structure responds by enabling kinetic energy from the impact to be absorbed by the structure, posing damage even at locations away from the point of impact [47]. In the high-velocity impact, a projectile traveling high velocity may induce localized damage, which can be intense and have serious consequences on the safety of aircraft and passengers [47]. Examples of high-velocity impact include bird strikes, which have become a regular occurrence in the aviation industry. High-velocity impact loading is more detrimental to the integrity of composite structure than a low-velocity impact loading, as higher velocity impact loading tends to produce greater damage and larger reductions in residual strength of the composite structure [47].

## 2.7 Fillers

The idea of improving the cold-curing resins by mixing them with filler particles to enhance their properties date back to 1951 [54]. Fillers are also incorporated into the resin matrices of fiber-reinforced polymer matrix composites to improve the performance of composite materials, which might not be offered by the reinforcement and the matrix alone [55]. For example, a resin that contains fillers shrink less than resins without fillers, thereby offering improved dimensional stability of manufactured molded parts [55]. Composite materials containing fillers can be identified according to the size of the filler namely; macro, micro, hybrid (containing both macro and micro fillers), and nanofilled composites [25], [56].

The macrofilled composites contain filler particles of a size range of 0.1- 150  $\mu\text{m}$  and examples of such macrofillers are quartz, borosilicate glass, and lithium aluminum glass [56]. Micro-filled composites contain fine (micro) filler particles of size range 0.007 – 0.14  $\mu\text{m}$  and  $\text{SiO}_2$  are examples [56]. A hybrid filler is the one that contains a blend of micro and macro filler particles. A nanocomposite is a multiphase solid material in which one of its constituents has one, two, or three dimensions of less than 100 nm [25]. The composites containing nanofillers can be classified into one, two, or three dimensions, based on the nanofillers dimension [25], [57]. One-dimensional nanofilled composites are composites in which the fillers has one of its dimensions less than 100 nm [25], [58]. The fillers are usually in the form of plates or sheets of one to few nanometers thick to hundreds and thousands of nanometers long. Examples of such fillers are nanosized graphene platelets [58]. Two-dimensional nanofilled composites have two of its filler dimensions less than 100 nm and are mostly in the shape of tubes, fibers, or filaments [25], [58]. Examples of such

fillers include carbon nanotubes (CNTs), carbon nanofibers (CNF), 2D graphene, boron nitride tubes, and clay nanotubes [58]. Three-dimensional nanofilled composites contain iso-dimensional fillers such that they are relatively equiaxed particles having all three dimensions in the nanometer scale [25], [58]. They are usually in spherical and cubical shapes. Examples include nanosilica, nanoalumina, carbon black, and silicon carbide [58].

Fillers can also be classified based on the base material as carbon-based, metal-based, and ceramic-based fillers [59]. The carbon-based fillers are usually nano in size, while the metal and ceramic could be micro or nano in size [60], [61].

### 2.7.1 Carbon-based fillers

Fillers made completely of carbon are known as carbon-based fillers [62], [63] and they can be classified into fullerenes, graphene, carbon nanotubes (CNTs), and carbon nanofibers (CNF) [63].

- a. Fullerenes: Fullerene (C<sub>60</sub>) is a carbon molecule that is spherical and made up of carbon atoms held together by sp<sup>2</sup> hybridization [63]. The number subscript represents the number of carbon atoms held together by the hybridization. C<sub>60</sub> is the most studied member of the fullerenes because it is less expensive and relatively inert under mild conditions [64]. About 28 to 1500 carbon atoms form the spherical structure with diameters up to 8.2 nm for a single layer and 4 to 36 nm for multi-layered fullerenes [63].
- b. Graphene: Graphene is an allotrope of carbon. Graphene is a hexagonal network of honeycomb lattice made up of carbon atoms in a two-dimensional planar surface. Generally, the thickness of the graphene sheet is around 1 nm [63].
- c. Carbon nanotubes: Carbon nanotubes (CNT) were discovered by Oberlin *et al.* [65] in 1976, without application, and then rediscovered by Iijima [66], [67] in 1991. Carbon nanotubes (CNTs) are ultrathin carbon fibers with a nanometer-size diameter and micrometer size length [68]. The structure of CNT consists of the rolled graphene sheet, which is a planar-hexagonal arrangement of carbon atoms forming a closed cylindrical structure [68], [69]. Graphene has C-C sp<sup>2</sup> bonds, which are stronger than the C-C sp<sup>3</sup> bonds in diamonds because the C-C sp<sup>2</sup> bond length is shorter than the C-C sp<sup>3</sup> bond [70]. However, the molecular force between the graphene layers is Van der Waals force, which allows them to slide with relative ease and, as a result, can be rolled to form a cone or cylindrical shape [57], [71]. CNTs have excellent properties such as a high Young modulus

of up to 1 TPa, a heat conductivity of  $3000 \text{ W m}^{-1} \text{ K}^{-1}$ , and an electrical conductivity value of  $107 \text{ S m}^{-1}$  [25], [57], [66], [68]. As a result of these unique properties, they are used to manufacture composite materials with superior mechanical, thermal, and electrical properties [68]. In general, there are two types of CNTs, depending on the number of rolled graphene sheets [25], [68] :

- i. Single-wall carbon nanotubes (SWCNTs): SWCNTs consist of a single graphene layer rolled into a seamless cylinder and they have a diameter between 1 and 2 nm [66], [68].
- ii. Multi-wall carbon nanotubes (MWCNTs): Consist of two or more concentric cylindrical shells of graphene coaxially arranged around a central hollow core and usually have a diameter of between 2 and 150 nm [57]. It is pertinent to note that double-walled carbon nanotubes (DWCNTs) fall under MWCNTs.

The SWCNTs are much stronger than the MWCNTs because SWCNTs have one cylindrical layer of graphene. In contrast, MWCNTs are formed by many co-axial cylindrical layers of graphene which deteriorates the strength due to the possibility of slip between the layers [69].

- d. Carbon nanofibers (CNFs): are made when graphene nanosheets are wound into a cone shape [63]. They are mainly differentiated from nanotubes by the orientation of the graphene planes. Whereas the graphitic layers are parallel to the axis in nanotubes, nanofibers can show a wide range of orientations of the graphitic layers with respect to the fiber axis [69]. They can be visualized as stacked graphitic discs or (truncated) cones and can be in the form of hollow tubes with an outer diameter as small as  $\sim 5 \text{ nm}$  [69].

### **2.7.2 Metallic fillers**

Metallic fillers are synthesized from metals to different metric sizes (micro or nano), either by destructive or constructive methods [63]. Metallic fillers are made up of metals that have weaker bonds between the atoms, allowing free movement of electrons. Hence they are excellent conductors of heat and electricity [72]. They can further be classified into non-oxide pure metal and metal oxide-based [63].

- a. Non-oxide pure metal based: Almost all the metals can be synthesized into their fillers [73], [74]. The commonly used metals for synthesis are aluminum (Al), cadmium (Cd), cobalt (Co), copper (Cu), gold (Au), iron (Fe), lead (Pb), silver (Ag), and zinc (Zn) [63]. The fillers have distinctive properties, such as small sizes up to 100 nm and a high surface area to volume ratio [63].
- b. Metal oxides based: They are synthesized to modify the properties of their respective metal-based fillers [63]. Metal oxide fillers are synthesized mainly due to their increased reactivity and efficiency [63], [75]. For example, nanoparticles of iron (Fe) instantly oxidize to iron oxide ( $\text{Fe}_2\text{O}_3$ ) in the presence of oxygen at room temperature, which increases its reactivity compared to iron nanoparticles [63]. In applications, Iron oxide nanofillers are used for adsorption or recovery of metal ions from natural water streams or industrial wastes [76]. Also, owing to their magnetic properties, they are used as magnetic guidance of particle systems for site-specific drug delivery [77]. The commonly synthesized metallic oxide fillers are aluminum oxide ( $\text{Al}_2\text{O}_3$ ), cerium oxide ( $\text{CeO}_2$ ), iron oxide ( $\text{Fe}_2\text{O}_3$ ), magnetite ( $\text{Fe}_3\text{O}_4$ ), silicon dioxide ( $\text{SiO}_2$ ), titanium oxide ( $\text{TiO}_2$ ), and zinc oxide ( $\text{ZnO}$ ) [63].

### **2.7.3 Ceramic fillers**

Ceramics fillers are based on ceramic materials that have properties lying between metals and non-metals and can be found in amorphous, polycrystalline, dense, porous, or hollow forms [59], [72]. They usually have low electrical and thermal conductivity, high elastic modulus, high stiffness, and are resistant to corrosive environments [72], [78]. The properties are dictated by the type of bonding between their constituent atoms, which is a combination of ionic and covalent bonds [72]. Examples of ceramic fillers are silicon carbide (SiC), alumina ( $\text{Al}_2\text{O}_3$ ), and silicon nitride ( $\text{Si}_3\text{N}_4$ ) [78].

## **2.8 Method of Fillers Dispersion**

A schematic representation of different forms of fillers distribution in a polymer resin is shown in Fig. 2.3. They are usually incorporated in the polymer matrix at a particular weight addition, depending on the discretion of the individual. If the fillers are poorly dispersed, they adhere to one another as a result of their Van der Waals forces, leading to the fillers agglomeration in the resin

[8]. The agglomeration of the fillers negatively influences the end properties of the resulting composites. The end goal of filler distribution in polymer resin is to achieve an excellent homogenous and distribution of the fillers through appropriate techniques to promote good filler distribution.

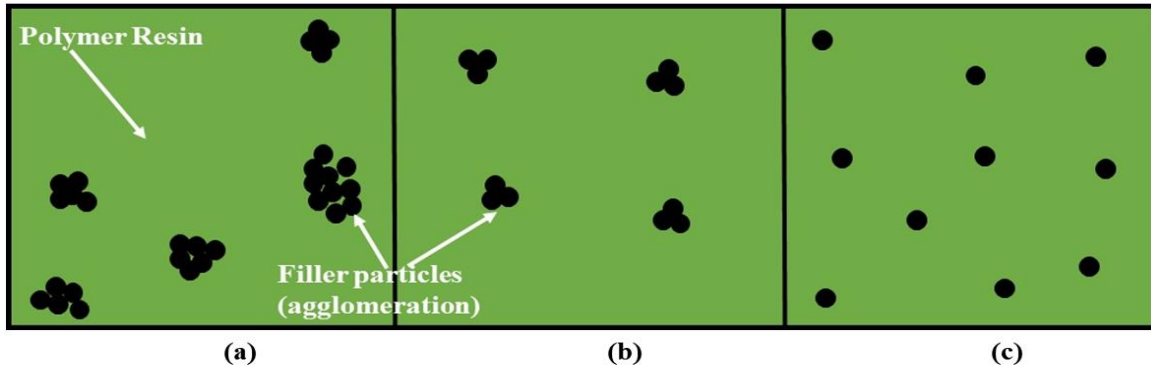


Figure 2.3. Different forms of distribution of filler particles in polymer resins: (a) inhomogeneous and non-uniform distribution (b) fairly homogeneous and fairly uniform distribution, and (c) uniform and homogeneous distribution.

A perfect dispersion of different micro or nanofillers in different types of polymer matrices could be very challenging and different tools are used to achieve this. Factors such as; physical (solid or liquid) and chemical (thermoplastic or thermoset) states of the polymer matrix, dimensions and content of micro or nanofillers to be added, availability of techniques and fabrication processes, are taken into account when selecting a proper technique for fillers dispersion [79]. Some methods employed in dispersing fillers in the polymer matrix are ultrasonication, magnetic stirring, calendaring, and ball milling [8], [79]–[84]. Using a combination of these dispersion techniques can further promote homogeneous dispersion of the fillers as opposed to using a single dispersion technique. Atif *et al.* [8] recommended combining the magnetic stirring technique with ultrasonication. In another work by Agbura *et al.* [85], the authors used dispersion techniques such as sonication, three roll mill (calendaring), and magnetic stirring in different combinations to promote nanoclay particle dispersion in epoxy resin.

## 2.9 Evaluation of Filler Dispersion

The dispersion state of fillers in the polymer matrix can be evaluated to provide an inference between the microstructure and the measured composite properties [86]. The most commonly used

experimental techniques for dispersion evaluation are scanning electron microscopy (SEM), transmission electron microscopy (TEM), and X-ray diffraction [87], [88]. The main application of the TEM methodology is for morphological examination and quantitation of exfoliated or intercalated samples [89]. In comparison with SEM, TEM provides additional information at finer scales about possible nanostructure, quantification of filler particles, and or the crystalline structure of the matrix [90]. For example, Luo *et al.* [89] developed a TEM methodology to quantify clay dispersion in a polymer layered silicate nanocomposites (PLSN). The authors developed a dispersion parameter  $D_{0.1}$ , where the subscript 0.1 represents the free path spacing between single nano clay sheets from the captured TEM images. The TEM technique has also been successfully used for dispersion evaluation of different filler types such as CNFs in polypropylene, Nanomontmorillonite (NaMMT) and multi-walled carbon nanotubes (MWCNTs) in chitosan and organo modified bentonite in poly-lactic acid (PLA) [87].

SEM technique is good for visualizing nanofillers at higher filler content (>0.5 wt.% addition) [91]. Below this threshold, it is difficult to visualize these nanofillers as SEM only gives information about the cross-sections of the bulk material [90]. Even if the fillers can be visualized on the SEM micrograph, below this threshold they are not likely to be a true representation of the filler dispersion since the SEM technique picks up particles that are fully or partially exposed on the surface, with the particles buried deeper beneath the surface remaining invisible on the micrographs [91]. However, TEM images can provide a good contrast between the matrix and the fillers and they are the preferred method for filler quantification by image analysis as compared to the SEM images, which have poor contrast [91].

The XRD method uses a characteristics diffractogram peak to determine the presence of the filler in the polymer matrix [23]. The composite material structure is considered to be intercalated with fillers if the XRD characteristic peak peculiar to either the fillers or composite constituents appears, decreases in intensity, or shifts to a low angle after reaction [23]. Another XRD technique is the phase-contrast X-ray imaging (high spatial resolution X-ray ultra-microscopy (XuM)) which was developed by Wu *et al.* [91] to provide 2D and 3D information on filler distribution in polymer composites. In their work, the authors compared the SEM and the XuM images for calcium carbonates ( $\text{CaCO}_3$ ) filler particles dispersed in nylon 6 matrix at 0.5, 1, 3, and 5 wt.% addition. The XuM images were used for filler dispersion quantification, using statistical analysis coupled

with image analysis software, Image-Pro Plus. They reported that the XuM images provide well clear, spatially resolved filler dispersions and even, the size and distribution of the fillers for all the weight additions. However, for the SEM images, at 0.5 wt.% loading, the filler was difficult to visualize, but the presence of the filler particles became apparent on the SEM micrographs as the filler loading increased.

Other techniques, such as Raman spectroscopy, can provide useful information about the material properties of carbon-based materials [68]. For example, the Raman spectra can provide information about the exceptional one dimensional (1D) properties of carbon materials, such as their photon and electronic structure, as well as information about sample imperfections [92]. Rheological measurements such as FTIR, differential scanning calorimetry (DSC), thermogravimetric analysis (TGA), and thermomechanical analysis (TMA), can also provide information about the presence of the fillers in the polymer matrix [68]. When these techniques are combined with XRD, TEM, SEM, they can provide detailed information about the state and mechanism of dispersion of the fillers in the polymer matrix of the composites [68].

## **2.10 Effect of Filler Addition on Properties of Phenolic Resin and Carbon Fiber Reinforced Phenolic**

Previous researchers have added fillers at different weight additions to improve intended desired properties. In a work by Yum *et al.* [93], they added carbon nanotubes (CNTs) to phenolic resin at 0.05, 0.1, and 0.3 wt.% filler loading to investigate the improvement in ablation resistance. The authors reported that the ablation resistance improved as a result of up to 0.1% CNTs addition before it started decreasing. In another work carried out by Ma *et al.* [11], they investigated the addition of graphitic carbon nitride ( $g\text{-C}_3\text{N}_4$ ) at 0.05, 0.1, and 0.2 wt.% on the ablation resistance of carbon fiber reinforced phenolic composites. The authors obtained optimum ablation resistance at 0.2 wt.% ( $g\text{-C}_3\text{N}_4$ ). Kaushik *et al.* [10] also studied the morphology and mechanical properties of phenolic reinforced with various amounts of montmorillonite clay (0.2, 0.4, 0.6, 0.8, 1.2, and 4 wt.%). They reported that the addition of 0.8 wt.% of montmorillonite clay gave the optimum flexural properties.

In another work done by Srikanth *et al.* [18], the authors studied the addition of zirconia (3.5, 6.5, and 9.5 wt.%) and carbon nanotubes (CNTs) at 0.5 wt.% on the mechanical properties of carbon

fiber reinforced phenolic composites. Optimum flexural strength was obtained with 0.5 wt.% CNTs, while the addition of zirconia did not improve the flexural strength. Pelin *et al.* [22] also investigated the addition of nano-SiC at 0.5, 1, and 2 wt.% on the flexural properties of phenolic resin. The authors reported that optimum flexural properties of phenolic were obtained with 1 wt.% nano-SiC addition. Sekhar *et al.* [23] studied the mechanical and thermal properties of phenolic resin modified with particles of natural graphite and graphite bisulfate. Graphite bisulfate was added at 0.1, 0.5, and 1 wt.% filler addition, while 1 wt.% natural graphite particles were added to the phenolic resin. When compared to the non-modified phenolic resin, the optimum flexural strength was obtained with the addition of 1 wt.% graphite bisulfate. On the other hand, the flexural strength of the phenolic decreased with the addition of natural graphite addition. Naderi *et al.* [19], also studied the addition of nano zirconium dioxide ( $n\text{ZrO}_2$ ) at 3, 5, and 7 wt.% on the ablation resistance of carbon fiber reinforced phenolic composites. The authors reported that optimum ablation resistance was obtained at 7 wt.% nanofiller addition.

### **2.11 Applications of Carbon Fiber Reinforced Phenolic Matrix Composites**

Carbon fiber reinforced phenolic composites are one route to the production of high-temperature resistant C/C composites [35]. Originally, there are two manufacturing routes for the manufacture of C/C composites; polymer infiltration and pyrolysis (PIP) and chemical vapor deposition (CVD) [1]. The PIP method is a three-stage process that starts with the manufacture of carbon fiber reinforced phenolic using phenolic resins as the matrix. The second stage involves the pyrolysis of the carbon fiber reinforced phenolic to convert the phenolic resin to amorphous carbon. Evaporation of the volatile content of the phenolic resin leads to a porous C/C composite, which is densified in the final stage by repeated cycles of impregnation with precursor resins and subsequent pyrolysis. Phenolic resin is the widely used matrix for C/C composite manufacture, because, they have a high carbon yield that is about 50-70% with consequent low weight loss during pyrolysis. The shrinkage of the phenolic during pyrolysis does not damage the carbon fiber preform, while the low viscosity of the phenolic resin aid re-impregnation during the densification process [1], [94].

The CVD process uses volatile carbon-hydrogen compounds such as methane, propane, benzene, and other low molecular carbon compounds as precursors [1], [5], [6]. The carbon fiber is heated in the precursor gaseous environment to deposit the matrix and thermal degradation is achieved on

the hot surface of the carbon reinforcement, resulting in a pyrolytic carbon deposit. By-product consisting mainly of hydrogen is released in the process. The drawback of CVD is the low rate of deposition resulting from the use of low gas pressure, which favors a long mean free path for the reactant and the decomposed gases. A long mean free path enhances deposition into the center of the sample bringing about the uneven thickness of the sample and inconsistent materials properties [6].

Amorphous carbon is brittle and flaw sensitive like ceramics [34]. Reinforcing carbon matrix with carbon fiber allows the composite to fail gradually and also gives advantages such as the ability to withstand high temperatures, low creep at high temperatures, low density, good tensile and compressive strengths, high fatigue resistance, high thermal conductivity, and a high coefficient of friction [1], [5], [6], [36]. Owing to these excellent properties, notable examples of C/C composite applications in extreme conditions include heat shields in re-entry vehicles, leading edges and nose cones of intercontinental ballistic missiles, aircraft heat exchangers, high friction members in aircraft and space shuttle orbiter [95].

## **2.12 Summary**

The improvements in different properties of carbon fiber reinforced phenolic matrix composites through filler additions have been reviewed. From previous works, it could be observed that optimum properties were mostly obtained at low fillers addition before these properties started to decrease. Also, carbon fiber reinforced phenolic matrix composites are prone to failure from flexural and dynamic impact loadings when used in their service environment. However, there is limited information in the literature assessing the flexural and dynamic impact properties of carbon fiber reinforced phenolic composites, especially with the possibility of improving these properties via suitable fillers addition. This knowledge gap gave the motivation for this study to provide additional knowledge, through the investigation of flexural and dynamic impact properties of carbon fiber reinforced phenolic composites in which colloidal silica and silicon carbide particles have been added as microfillers.

## CHAPTER 3

### MATERIALS AND METHODOLOGY

In this chapter, the materials and methods used for manufacturing the carbon fiber reinforced phenolic matrix (CFRP) composites are discussed. The procedures for dispersing the microfillers in the phenolic resin, impregnation of the carbon preform with the resin, and the subsequent curing process to obtain the CFRP are highlighted. Furthermore, the procedures for characterization of the composites using optical and scanning electron microscopy, thermogravimetric analysis (TGA), Fourier transform infrared spectroscopy (FTIR) analysis, X-ray diffraction (XRD), flexural test (3-point), dynamic impact test, and statistical analysis are provided.

#### 3.1 Materials

A 3K, 2x2 twill weave carbon fiber fabric manufactured by Fibre Glast Developments Corporation (Brookville, Ohio, USA) was used as reinforcement for the fabrication of the carbon fiber reinforced phenolic matrix (CFRP) composite. The thickness of each carbon fiber fabric layer was first determined to be 0.3048 mm. This is very important to decide the number of layers of carbon fiber fabric required to fill up the mold cavity. Two variations of phenolic resin (resole) supplied by SI Group (Schenectady, New York, USA) was used in this study. They are HRJ-15881 and SP-6877. The chemical analysis of the two phenolic resins, as provided by the manufacturer, is provided in Table 3.1. Colloidal silica (406), manufactured by West System Inc. (Michigan, USA) and silicon carbide (SiC) produced by Washington Mills (Massachusetts, USA), are the microfillers used in this study. The colloidal silica consists of quartz particles with an average particle size of 0.2 - 0.3  $\mu\text{m}$  and a density of 0.05  $\text{g}/\text{cm}^3$ . The SiC has a density of 3.19  $\text{g}/\text{cm}^3$  and a particle size of 1.2 - 53  $\mu\text{m}$ . According to the manufacturer (Washington Mills), the SiC microfiller was produced by mixing silica ( $\text{SiO}_2$ ) with carbon (C) in an electric resistance furnace at temperatures around 2500  $^\circ\text{C}$ .

Table 3.1. Chemical analysis of the phenolic resins used in this study.

Characteristics	HRJ-15881	SP-6877
Phenol (%)	13.61	13.61
Solids (%)	76.09	76.09
Viscosity Brookfield (cP)	906	53.1
pH Value	8.1	8.1
Gel Time (min.)	12.5	12.5
Formaldehyde (HCHO, (%))	0.5	1.3

### 3.2 Manufacturing of Carbon Fiber Reinforced Phenolic

The flow chart summarizing the manufacturing process for the carbon fiber reinforced phenolic matrix (CFRP) composites is presented in Fig. 3.1. Where the addition of fillers is needed, the filler was first added to the resin, followed by ultrasonication and magnetic stirring. The next step involves hand-laying of the cut carbon fibers fabrics in the mold cavity. This was followed by infiltration of the resin into the fiber preform inside the mold cavity. Curing was subsequently done in a Parr 4848 pressure reactor (autoclave) to obtain the CFRP composites.

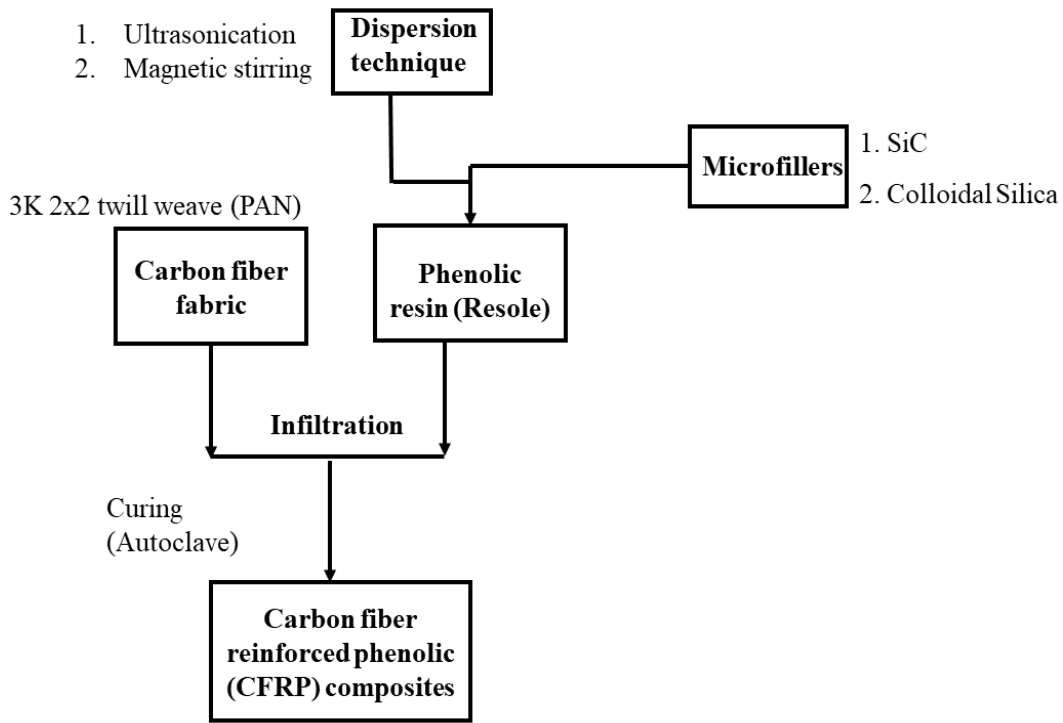


Figure 3.1. Manufacturing process flow chart for carbon fiber reinforced phenolic.

### 3.2.1 Dispersion of colloidal silica in phenolic resin

The 406 colloidal silica was mixed with polyethylene glycol (Carbowax™ PEG-400) supplied by Fisher Chemical, Canada to form a shear thickening fluid (STF). Shear thickening is an increase in viscosity when the shear rate during mechanical deformation increases to a critical value [96]. The most studied STF is based on the suspension of silica in polyethylene glycol [97]. The PEG used is made of Carbowax with the chemical formula (C<sub>2</sub>H<sub>4</sub>O<sub>n</sub>H<sub>2</sub>O) and a density of 1.13 g/ml, it has low volatility and good thermal stability [98]. The STF was produced as described by Haro *et al.* [98]; The Carbowax™ PEG-400 and the colloidal silica were mixed in a ratio of 2:1 and stirred using a magnetic stirrer at 1200 RPM for 3 h at room temperature. After preparation, the STF was then diluted with ethyl alcohol using the ratio 3:2 and held for 2 h. This mixture was then added to the phenolic resin in appropriate proportions to obtain 0.5, 1.0, 1.5, and 2.0 wt.% of the colloidal silica in the phenolic resin. As an additional step to promote colloidal silica dispersion in the phenolic resin, the mixture was subjected to mechanical magnetic stirring at 1200 rpm for 1 h. This was followed by ultrasonication bath using Branson 1510 ultrasonicator for 1 h.

### 3.2.2 Dispersion of SiC in phenolic resin

The photographs presented in Fig. 3.2 depict the changes that occur in each step during the microfillers dispersion and CFRP manufacturing. Fine SiC particles were first weighed in appropriate proportions to obtain 0.5, 1, 1.5, and 2 wt.% in the composites. The SiC particles were then mixed with 5ml ethanol (absolute) to produce composites containing 0.5 wt.% SiC. The volume of ethanol mixed with SiC particles was increased to 6, 7, and 8 ml for composites containing 1, 1.5, and 2 wt.% SiC particles, respectively to ensure good dispersion of the SiC particles in the ethanol. The open part of the beaker was covered with aluminum foil to prevent the mixture from splashing out (Fig. 3.2b). The essence of the ethanol absolute is to serve as a dispersant medium for the SiC in the phenolic resin. During curing (cross-linking) of the polymer chains at a temperature greater than 100 °C, it is expected that the ethanol will evaporate, leaving behind well-dispersed SiC particles in the phenolic resin. The SiC particles mixed with ethanol was then subjected to ultrasonication using Branson 1510 ultrasonicator for 30 min. (Fig. 3.2c). The ultrasonicated ethanol containing SiC particles was then mixed with the phenolic resin (Fig. 3.2d). Afterward, this mixture was subjected to further ultrasonication for 1 h (Fig. 3.2 (e, f)). The mixture was further subjected to magnetic stirring at 1200 rpm for 1 h after ultrasonication (Fig. 3.2g), to obtain a homogenous mixture (Fig. 3.2h). The ultrasonication and the magnetic stirring

method serve to complement one another and promote homogenous dispersion of the microfillers in the resin. The order at which they are done does not affect the microfillers dispersion.

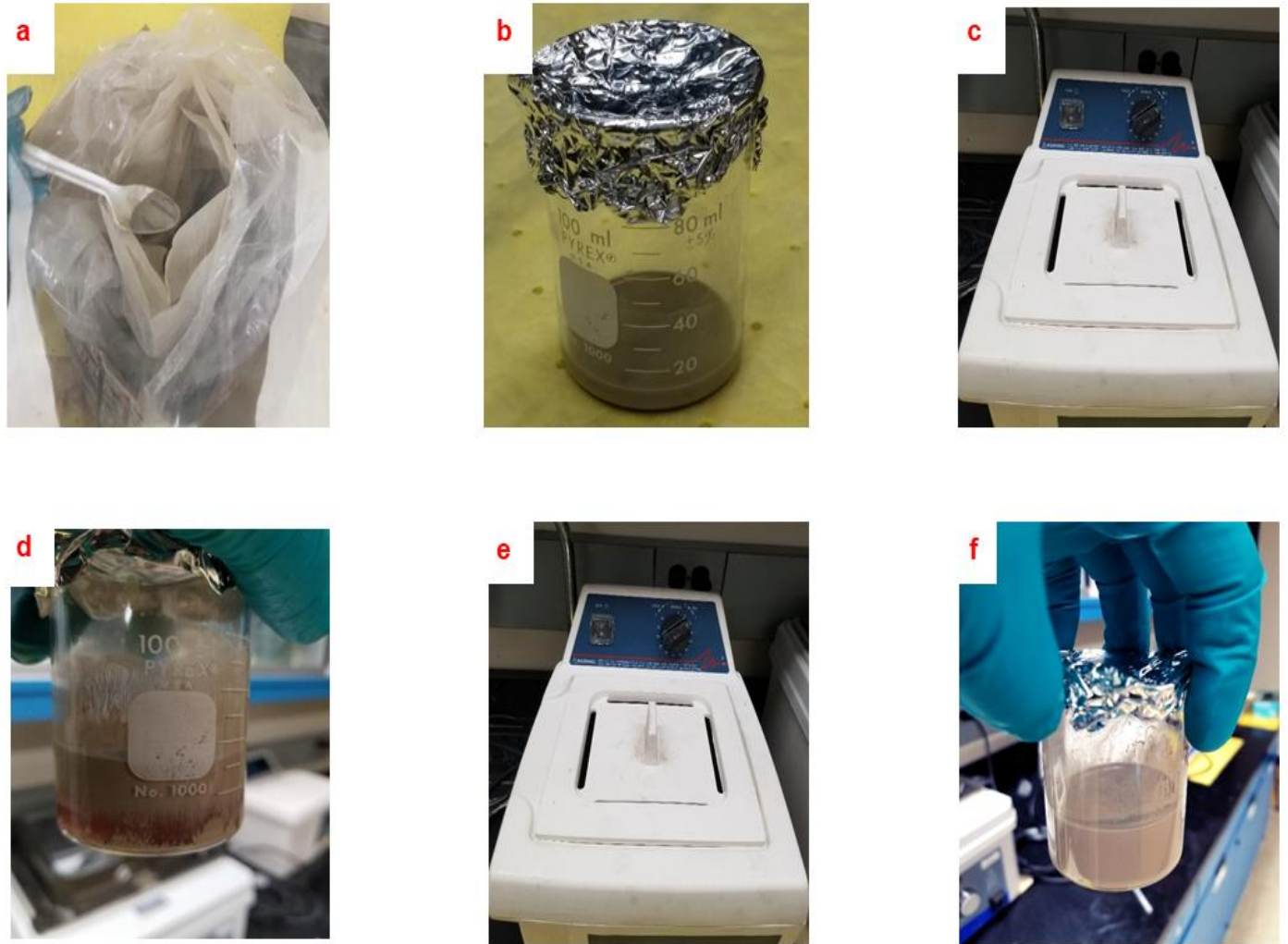


Figure 3.2. Photograph showing stages in microfiller dispersion and CFRP manufacturing: (a) SiC microfillers (MF) (b) SiC MF + ethanol absolute (c) ultrasonication (d) phenolic resin added (e) ultrasonication, and (f) ultrasonicated mixture.



Figure 3.2 continued. Photographs showing stages in microfillers dispersion and CFRP manufacturing: (g) magnetic stirring (h) homogenous mixture (i) mold sprayed with release agent (j) carbon fiber lay-up (k) phenolic resin infiltration, and (l) autoclave curing.

### 3.2.3 Fabrication of carbon fiber reinforced phenolic

A mold with a rectangular internal cavity having dimensions of 170.00 mm x 60.00 mm x 3.47 mm and 170 mm x 60.00 mm x 10 mm, was used to manufacture the flexural and dynamic impact test specimens of the CFRP, respectively. The molds were fabricated at the University of Saskatchewan engineering workshop. The composite fabrication procedure consists of cutting the carbon fiber fabric into a dimension of 160 mm x 60 mm. The number of carbon fiber fabric layers required for flexural ( $N$ ) and dynamic impact ( $M$ ) specimens was determined using Equations (3.1) and (3.2) respectively:

$$N = \frac{\text{thickness of mold internal cavity}}{\text{thickness one layer of the 2D carbon fiber fabric}} = \frac{3.47\text{mm}}{0.3048\text{mm}} = 11 \text{ layers} \quad (3.1)$$

$$M = \frac{\text{thickness of mold internal cavity}}{\text{thickness one layer of the 2D carbon fiber fabric}} = \frac{10\text{mm}}{0.3048\text{mm}} = 33 \text{ layers} \quad (3.2)$$

Slide® Epoxease mold release lubricant #40614N manufactured by Infotrac company was sprayed on the internal cavity of the mold and was left to dry for 25 min. (Fig. 3.2i). The mold release agent facilitates the easy removal of the CFRP from the mold after curing. Eleven and thirty-three layers of the carbon fiber fabric were stacked together inside the mold to fill up the internal mold cavity for the flexural and dynamic impact test samples, respectively. A representative of the carbon fiber lay up inside the mold cavity for the flexural test sample is shown in Fig. 3.2j. The priorly mixed phenolic resins with or without microfillers were then infiltrated into the mold cavity. The mixture slowly impregnated the carbon fiber preform inside the mold cavity with the aid of the gravitational force until the filler-impregnated resin had filled all the voids inside the carbon fiber preforms (Fig. 3.2k). The mold containing resin-impregnated carbon fiber preform was placed inside a Parr 4848 pressure reactor (Moline, Illinois, USA) for curing of the resin (Fig. 3.2l).

The cure cycle is schematically presented in Fig. 3.3. Using the ramp and soak programming of the autoclave, curing was done by heating the resin at 2 °C/min from room temperature to 120 °C. It was held at 120 °C for 1 h followed by slow cooling inside the reactor to room temperature. The reactor pressure is 50 bar, and the specimens were cured under an argon gas atmosphere. Curing was done under pressure to ensure the elimination of gaseous by-product of polymerization reactions during curing and thereby reduce the porosity of the CFRP. The ramp and soak program used in this study is provided in the Appendix B section of this thesis.

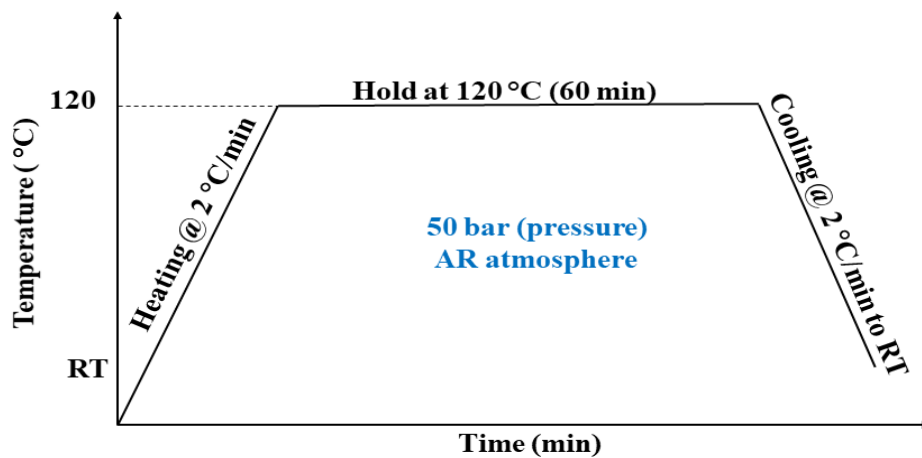


Figure 3.3. Curing cycle for the carbon fiber reinforced phenolic.

### 3.3 Materials Characterization

#### 3.3.1 Thermogravimetric analysis

To evaluate the thermal stability of the phenolic resins used in this study, and determine the appropriate curing temperature, thermogravimetric analyses (TGA) of the resins were carried out using a TA instrument model Q5000 (New Castle, Delaware, USA) (Fig. 3.4). The equipment is located at the Department of Chemistry, University of Saskatchewan. Each scan was performed using an open platinum pan from room temperature to 1000 °C and a heating rate of 10 °C/min in a nitrogen gas atmosphere. The flow rate of the balance gas and sample gas are 10.0 ml/min and 25.0 ml/min, respectively. About 30 mg of each sample (HRJ-15881 and SP-6877) phenolic resin was used for the analysis. The mass-loss rate in wt.% was obtained, and the derivative TG (DTG) data (% loss/ °C) was calculated from the mass loss data.

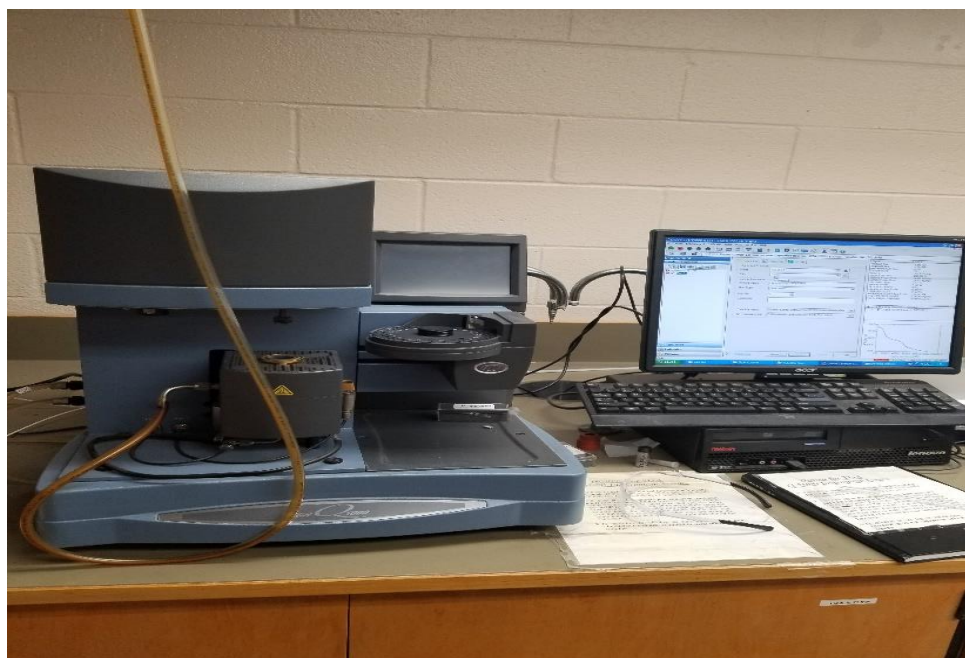


Figure 3.4. TA instrument Q5000 used in this study.

#### 3.3.2 Fourier transform infrared spectroscopy analysis

Fourier Transform Infrared Spectroscopy (FTIR) analysis uses an infrared absorption spectrum to identify the chemical bonds in a polymer resin. The spectra produced a profile of the phenolic resin, which is a distinctive molecular fingerprint that can be used to screen the phenolic resin for its functional group, and provide the corresponding covalent bonding information. A Renishaw

Raman inVia Reflex Microscope (Renishaw Inc, West Dundee, IL) coupled to a Smiths IlluminatIR II™ spectrometer equipped with a diamond attenuated total reflection (ATR) with a capacity of 36X objective was used to obtain the FTIR spectra. A photograph of this equipment is presented in Fig. 3.5, and it is located at the Saskatchewan Structural Sciences Center, University of Saskatchewan. The FTIR data were acquired at a resolution of 4 cm<sup>-1</sup> and 512 scans per sample and a wavelength range of 4000 – 600 cm<sup>-1</sup>.



Figure 3.5. Renishaw Raman InVia Raman microscope used in this study.

### 3.3.3 X-ray diffraction (XRD)

XRD analysis was done using Rigaku Ultima IV X-Ray Diffractometer (Rigaku Americas Corporation, Texas, USA), equipped with a Cu source (1.54056Å), a CBO optical, and a Scintillation Counter detector. The XRD equipment is located at the Saskatchewan Structural Sciences Center, University of Saskatchewan. The diffractometer was operated at a voltage of 40 kV and a current of 44 mA. The measurements were carried out on the multipurpose attachment with a parafocusing mode. A K<sub>β</sub> filter (Ni foils) was placed at the receiving end. The diffraction patterns were measured from 5° to 60°, using a scan rate of 0.5 °/min and a step size of 0.02. PANalytical X'Pert Highscore software was used for background correction and smoothing of the raw XRD files. Origin 2019 software was then used to plot and analyze the obtained XRD data. Before performing the XRD test, the composite samples were dipped in nitrogen gas and crushed

in an acetone cleaned ceramic crucible to fine aggregates. Photographs of a ground composite sample and the Rigaku Ultima IV X-ray Diffractometer used in this study are presented in Figs. 3.6 and 3.7, respectively.



Figure 3.6. Photograph of ground composite sample used for XRD in this study.



Figure 3.7. Rigaku Ultima IV X-ray Diffractometer used in this study.

### 3.3.4 Flexural tests (3-point bending test)

The flexural test sample used in this study is shown in Fig. 3.8. An Instron™ universal testing machine (Model 5500R) (Norwood, MA, USA) equipped with a 5 kN-capacity load cell was used to conduct the three-point bending test according to ASTM D790-17 standard [99]. The equipment is located at the Department of Chemical and Biological Engineering, University of Saskatchewan.



Figure 3.8. Photograph of flexural test samples.

The dimension of the rectangular tests specimens are 127.0 mm (length) x 12.7 mm (width) x 3.5 mm (thickness) with a span (s)-to-depth (d) ratio ( $\frac{s}{d}$ ) of 16:1 (Fig. 3.9) as recommended in the ASTM standard.

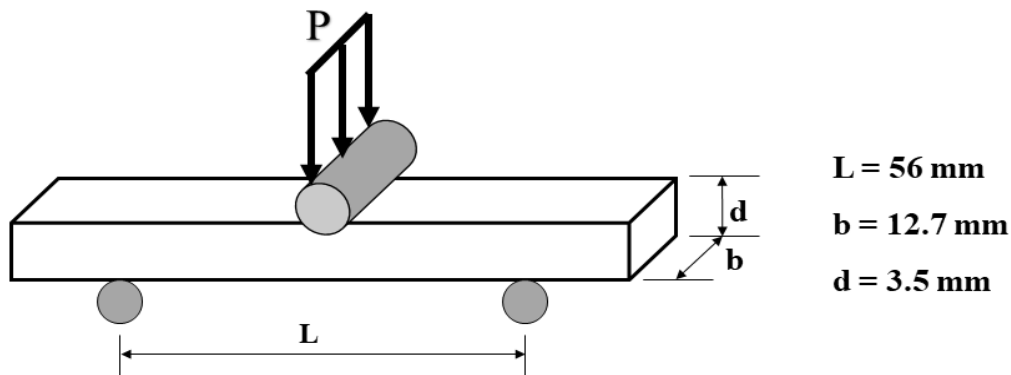


Figure 3.9. Schematic representation of the geometry of the flexural test specimen and its dimensions.

The rate of crosshead motion ( $R$ ), flexural strength ( $\sigma_f$ ), and tangent modulus of elasticity ( $E_f$ ) were calculated using equations (3.3) – (3.5) respectively as outlined in the ASTM standard.

$$R = \frac{ZL^2}{6d} \quad (3.3)$$

where  $Z$ , a constant, is the rate of straining of the outer fiber (0.01 mm/min), while  $L$  and  $d$  are the support span (56 mm) and the thickness of the sample (3.5 mm), respectively.

$$\sigma_f = \frac{3PL}{2bd^2} \quad (3.4)$$

where,  $\sigma_f$ ,  $P$ ,  $L$ ,  $b$ , and  $d$ , are flexural stress (MPa), load at a given point, support span (mm), width (mm), and thickness (mm) of tested samples, respectively (Fig. 3.10).

$$E_f = \frac{L^3 m}{4bd^3} \quad (3.5)$$

where,  $E_f$ ,  $L$ ,  $b$ ,  $d$ , and  $m$ , are flexural modulus (MPa), support span (mm), width (mm), thickness (mm), and slope of the tangent to the initial straight-line portion of the load-deflection curve (N/mm), respectively. A crosshead speed of 1.35 mm/min was used in the flexural test, as obtained from equation (3.3). Photograph of the Instron™ universal testing machine showing a flexural test specimen in 3-point bending loading are shown in Figs. 3.10.

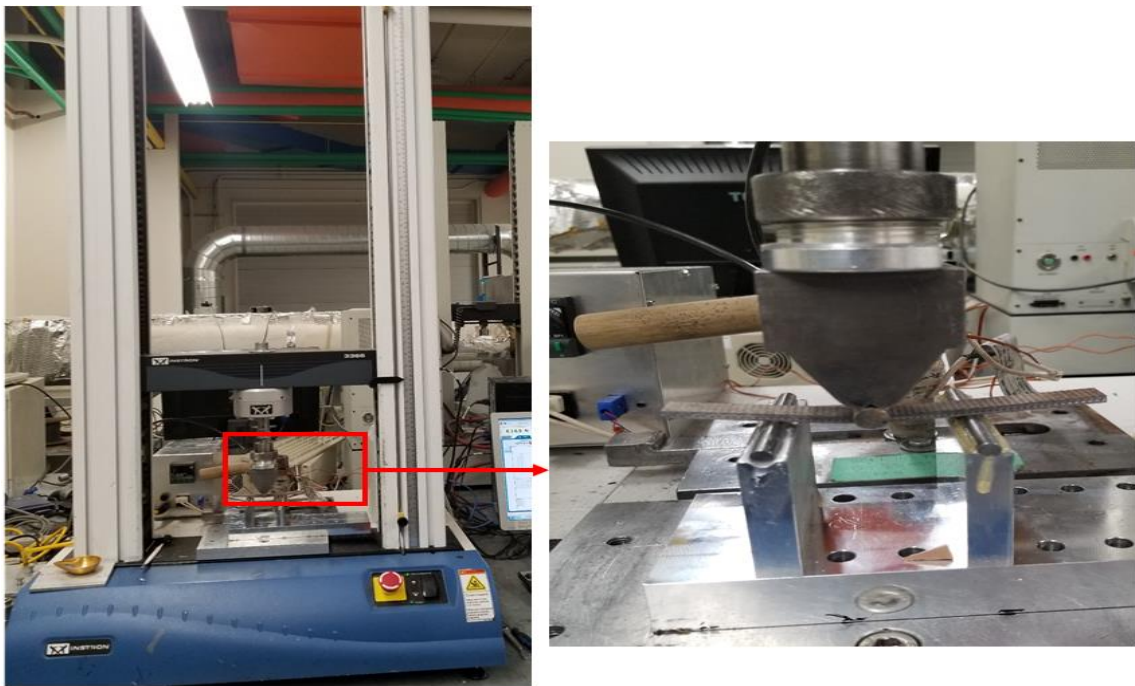


Figure 3.10. Instron™ universal testing machine (Model 5500R) showing three-point bend testing of the composites.

### 3.3.5 Dynamic impact test

The dynamic impact test was conducted to evaluate the impact (high strain-rate) response of the manufactured CFRP samples. The test was performed using a Split Hopkinson pressure bar (SHPB) system. A schematic representation of the SHPB is shown in Fig. 3.11, and it is located at the Department of Mechanical Engineering, University of Saskatchewan. The SHPB consists of three pressure bars; striker, incident, and transmitted bars. The incident and transmitter bars are 38 mm in diameter and are made of 7075-T651 aluminum alloy. The tested sample is cuboidal in shape with a dimension of 12 mm x 12 mm x 10 mm. A photograph of the dynamic impact test samples is shown in Fig. 3.12. The specimen was sandwiched between the incident and the transmitted bars. Before impact, both surfaces of the specimen in contact with both the incident and transmitted bars were lubricated to reduce friction between the specimen and the bars. With the use of a light gas gun, the striker bar was fired towards the incident bar at a pressure of 50 and 80 kPa. The firing pressures of 50 and 80 kPa generated impact momenta of 15 kg m/s and 28 kg m/s, respectively. On impacting the incident bar, an incident stress pulse was generated, which propagated along the incident bar towards the interface of the incident bar and the sandwiched test specimen. At this interface, a fraction of the incident pulse was reflected back to the incident bar, while the rest propagated to the transmission bar through the sandwiched specimen. Kolsky [100] stated that a constant strain rate is helpful to eliminate the effect of radial inertia on tested samples during the SHPB test. To achieve this, a pulse shaper having the same area as the incident and the transmitted bars but with a height of 12mm was attached to the end of the incident bar. Therefore, when the striker bar was fired at the corresponding impact momentum, that striker bar comes in contact with the pulse shaper attached to the end of the incident bar, to help achieve a constant strain rate. The elastic strain waves (incident, reflected, and transmitted) propagating through the incident and transmitter bars were captured by the mounted strain gauges on these bars. The elastic strain waves were amplified and conditioned by the connected strain conditioner/amplifier and subsequently recorded using a mixed-signal digital oscilloscope connected to the strain amplifier. Based on the strain pulses captured by the strain gauges, the nominal stress ( $\sigma_n$ ), nominal strain ( $\epsilon_n$ ), and nominal strain rates ( $\dot{\epsilon}_n$ ) were calculated using equations (3.6) – (3.8), respectively [100].

$$\sigma_n = \frac{A_B}{A_S} E_B \epsilon_T \quad (3.6)$$

$$\epsilon_n = -2 \frac{C_B}{L_S} \int_0^t \epsilon_R dt \quad (3.7)$$

$$\dot{\epsilon}_n = -2 \frac{C_B}{L_S} \epsilon_R \quad (3.8)$$

where  $A_B$  and  $A_S$  are the cross-sectional areas of the bars and specimens, respectively.  $\epsilon_T$  and  $\epsilon_R$  are transmitted and reflected strain pulses, respectively.  $C_B$  is the velocity of elastic waves in the bars, while  $E_B$  is the elastic modulus of the bar materials.  $L_S$  and  $t$  are the initial lengths of the specimen and deformation time, respectively. As the positive direction in the SHPB test is in the same direction as the wave in the incident bar (i.e., incident pulse, which is compressive), the negative sign in equation (3.8) is due to the opposite direction of the reflected wave (i.e., strain in the reflected pulse). The flow curves are plotted based on true stress ( $\sigma_t$ ), true strain ( $\epsilon_t$ ), and true strain rate ( $\dot{\epsilon}_t$ ), equations (3.9) – (3.11) were used to determine the true stress ( $\sigma_t$ ), true strain ( $\epsilon_t$ ), and true strain rate ( $\dot{\epsilon}_t$ ) values respectively [101].

$$\sigma_t = \sigma_n(1 - \epsilon_n) \quad (3.9)$$

$$\epsilon_t = -\ln(1 - \epsilon_n) \quad (3.10)$$

$$\dot{\epsilon}_t = \frac{\dot{\epsilon}_n}{(1 - \epsilon_n)} \quad (3.11)$$

The corresponding true stress and true strain generated from equations (3.9) and (3.10) were used to determine the true stress-strain curve of the manufactured samples. The firing pressures of 50 and 80 kPa generated an average true strain rate of  $880 \text{ s}^{-1}$  and  $2150 \text{ s}^{-1}$  in the tested samples, respectively.

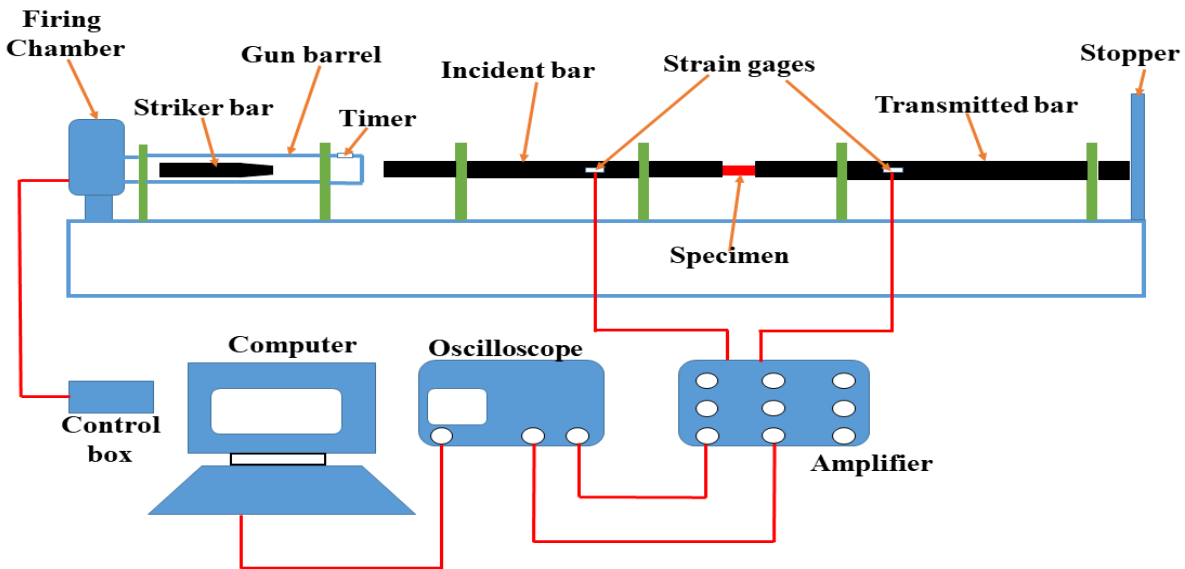


Figure 3.11. Schematic representation of the Split Hopkinson pressure bar used in this study.

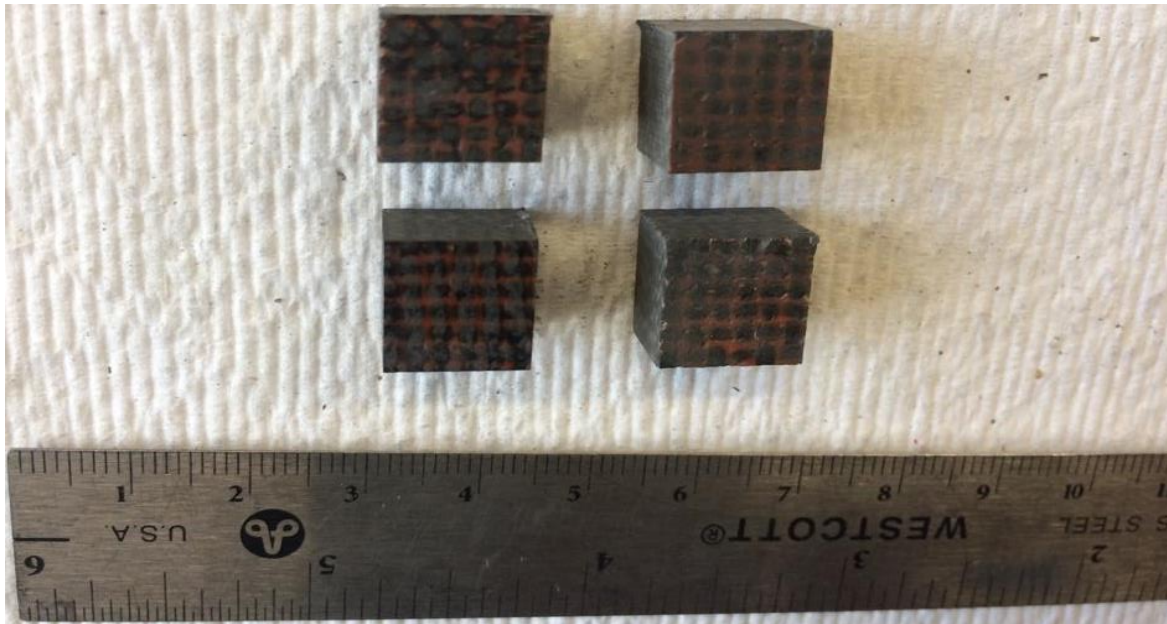


Figure 3.12. Photograph of dynamic impact test samples.

### 3.3.6 Microstructure examination

The CFRP samples for microscopic investigations were sectioned and pre-ground using 320, 500, 800, and 1200 SiC grit emery papers. This was followed by fine grinding using 2000 and 4000 SiC grit emery papers. Final polishing of the samples was done using 5  $\mu\text{m}$  MD-Dac cloth with 5  $\mu\text{m}$  MD-Dac suspension and 1  $\mu\text{m}$  MD-Nap cloth with 1  $\mu\text{m}$  MD-Nap suspension. The optical microscopy was done using a Nikon Eclipse MA 1500 microscope and Nikon optihot stereomicroscope (Melville, New York, USA) coupled with PAX-it software. The Eclipse microscope and optihot stereomicroscope were used for the fractography of the flexural and dynamic impact samples respectively. JEOL-JSM-6010LV (Peabody, MA, USA) scanning electron microscope (SEM) was used for scanning electron microscopic investigation of polished and fractured specimens. The photographs of the Nikon eclipse, Nikon optihot, and scanning electron microscopes used in this study are presented in Figs. 3.13, 3.14, and 3.15, respectively, and they are located at the Department of Mechanical Engineering, University of Saskatchewan.



Figure 3.13. Nikon Eclipse MA 1500 microscope used in this study.

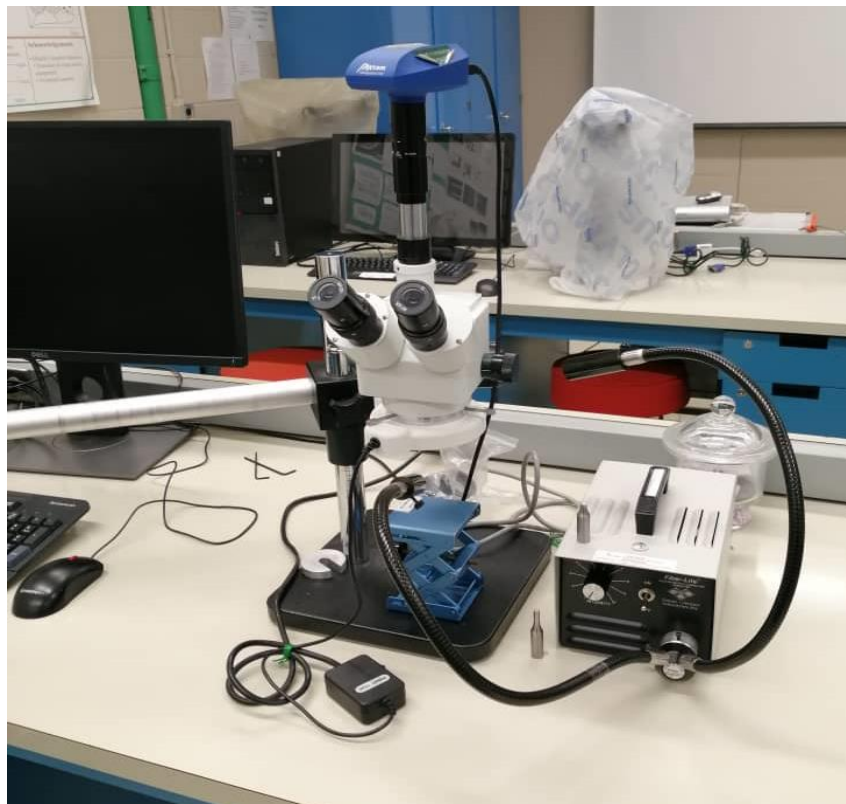


Figure 3.14. Nikon optiphot stereomicroscope used in this study.



Figure 3.15. JEOL-JSM-6010LV scanning electron microscope (SEM) used in this study.

The SEM specimens were gold-coated using an Edward S150B sputter coater (BOC Edwards, UK) while the SEM images were acquired using an accelerating voltage of 20 kV. The sputter coater is shown in Fig. 3.16, and it is located at the Department of Biology, University of Saskatchewan.

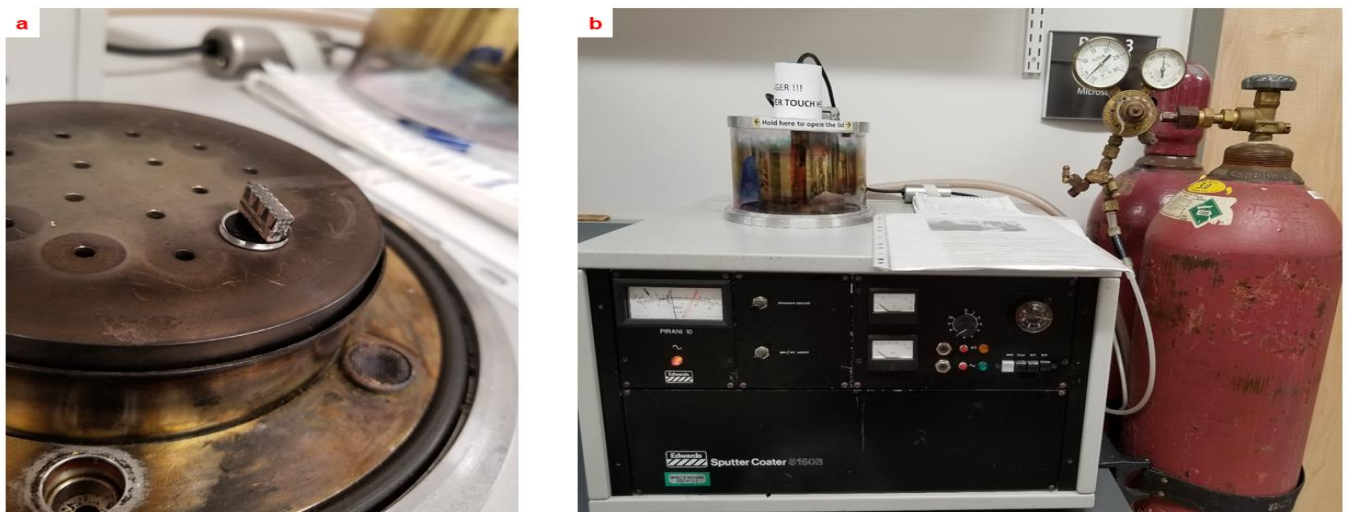


Figure 3.16. Edward S150B sputter coater used in this study.

### **3.3.7 Statistical analysis**

Statistical analysis was done using SPSS Statistics 26 software, available at the virtual laboratory portal of the University of Saskatchewan. One-way analysis of variance (ANOVA) with a level of significance of 5% (i.e., 95% level of confidence) was carried out to determine the effect of microfiller addition on flexural properties (flexural strength and flexural modulus) and dynamic impact strength of the manufactured carbon fiber reinforced phenolic composites produced in this study.

## CHAPTER 4

### RESULTS AND DISCUSSION

The results obtained from the experimental investigations outlined in Chapter 3 are presented and discussed in this chapter. It contains five subsections, the first of which focuses on the rheological measurements on the phenolic resin. The second subsection deals with the microstructural examination of the as-manufactured carbon fiber reinforced phenolic without fillers. The third subsection contains the mechanical response of the manufactured carbon fiber reinforced phenolic, with and without microfillers under 3-point flexural and dynamic impact loading. The fourth section deals with the results of the XRD analysis and percentage crystallinity of the carbon fiber reinforced phenolic matrix composites, with and without microfillers. The results of the damage evolution in the composites under flexural and dynamic impact loading, as observed under optical and scanning electron microscopes, are presented in the fifth subsection.

#### 4.1 Fourier-Transform Infrared Spectroscopy (FTIR)

The FTIR spectra obtained for HRJ-15881 and SP-6877 phenolic resins are presented in Figs. 4.1(a) and 4.1(b), respectively. The corresponding assignment of the peaks is provided in Table 4.1. The assignment of characteristic absorbance peaks of the spectrums was done based on literature sources [10], [102], [103]. These peaks helped in identifying the functional groups present in the two phenolic resins used in this study.

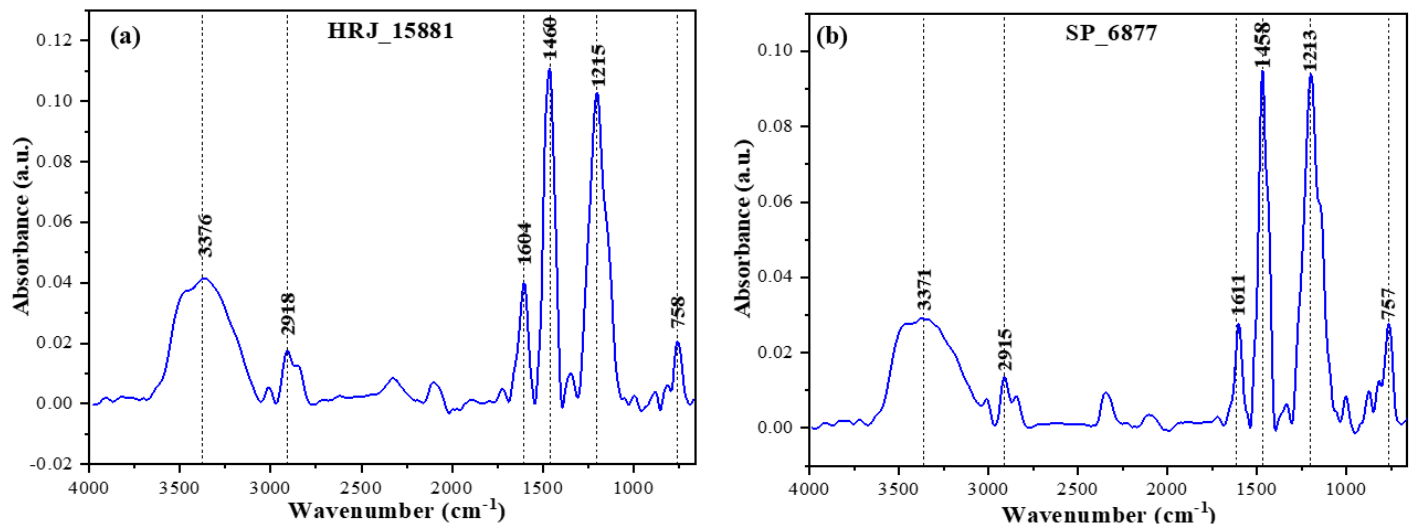


Figure 4.1: FTIR spectra obtained for the cured phenolic resins

Table 4.1. FTIR spectra functional group assignment.

<b>SP-6877</b> <b>Wavenumbers</b> <b>(cm<sup>-1</sup>)</b>	<b>HRJ-15881</b> <b>Wavenumbers</b> <b>(cm<sup>-1</sup>)</b>	<b>Literature</b> <b>Wavenumbers</b> <b>(cm<sup>-1</sup>)</b>	<b>Functional group identification</b> [10], [102], [103]
3371	3376	3400	Phenolic –OH stretch
2915	2918	2925	C-H stretch
1611	1604	1608	Aromatic C=C stretch
1458	1460	1460	-CH <sub>2</sub> - deformation vibration
1213	1215	1235	Asymmetric stretch of phenolic C-C-OH
757	758	760	C-H out of plane ortho-substituted

A blank (empty scan) was run before the FTIR scanning of the phenolic resins and the background of the Infrared (IR) spectrums have been corrected. The SP-6877 and HRJ-15881 resins both have broad peaks at 3371 and 3376 cm<sup>-1</sup>, respectively. The absorbance intensity is higher in HRJ-15881 than SP-6877, while the appearance of both peaks is attributed to phenolic-OH stretch. The appearance of mildly sharp peaks at wavenumbers 2918 and 2915 cm<sup>-1</sup>, for HRJ-15881 and SP-6877, respectively, is attributed to C-H stretch [10], [102], [103]. However, the absorbance peak band is higher for HRJ-15881 than SP-6877. The aromatic C=C stretch accounts for the sharp peaks at 1604 and 1611 cm<sup>-1</sup>, for HRJ-15881 and SP-6877, respectively [10], [102], [103]. The intensity is higher for HRJ-15881 resin than SP-6877 resin. The peaks at 1460 and 1458 cm<sup>-1</sup> for HR-15881 and SP-6877, respectively, are attributed to -CH<sub>2</sub>- deformation vibration with the absorbance intensity higher in HRJ-15881. The asymmetric stretch of phenolic C-C-OH is responsible for the sharp peaks at 1215 and 1213 cm<sup>-1</sup>, respectively, for HRJ-15881 and SP-6877 with the intensity higher in HRJ-15881. The sharp peaks at 758 and 757 cm<sup>-1</sup>, respectively for HRJ-15881 and SP-6877 are attributed to C-H out-of-plane ortho-substituted functional group [10], [102], [103], with the intensity higher in SP-6877 than HRJ-15881. From the FTIR spectra, it can be inferred that the structure of the cured phenolic matrix is primarily due to methylene bridged phenolic units [104]. Although the two investigated phenolic resins (HRJ-15881 and SP-6877) have the same phenol and solid content, they only differ in their viscosity before curing and

the formaldehyde (HCHO) content. The slight differences in the peak intensities may be due to the difference in the formaldehyde content of the resins.

#### 4.2 Thermal Analysis

The TGA and DTG provided information about the thermal stability and the trend of the decomposition process as the temperature of the applied resin increased from room temperature to 1000 °C. The TGA and DTG plots obtained for the two resins are presented in Figs. 4.2 and 4.3, respectively. Table 4.2 shows the mass loss (in %) at different temperature ranges for both varieties of phenolic resins used in this study.

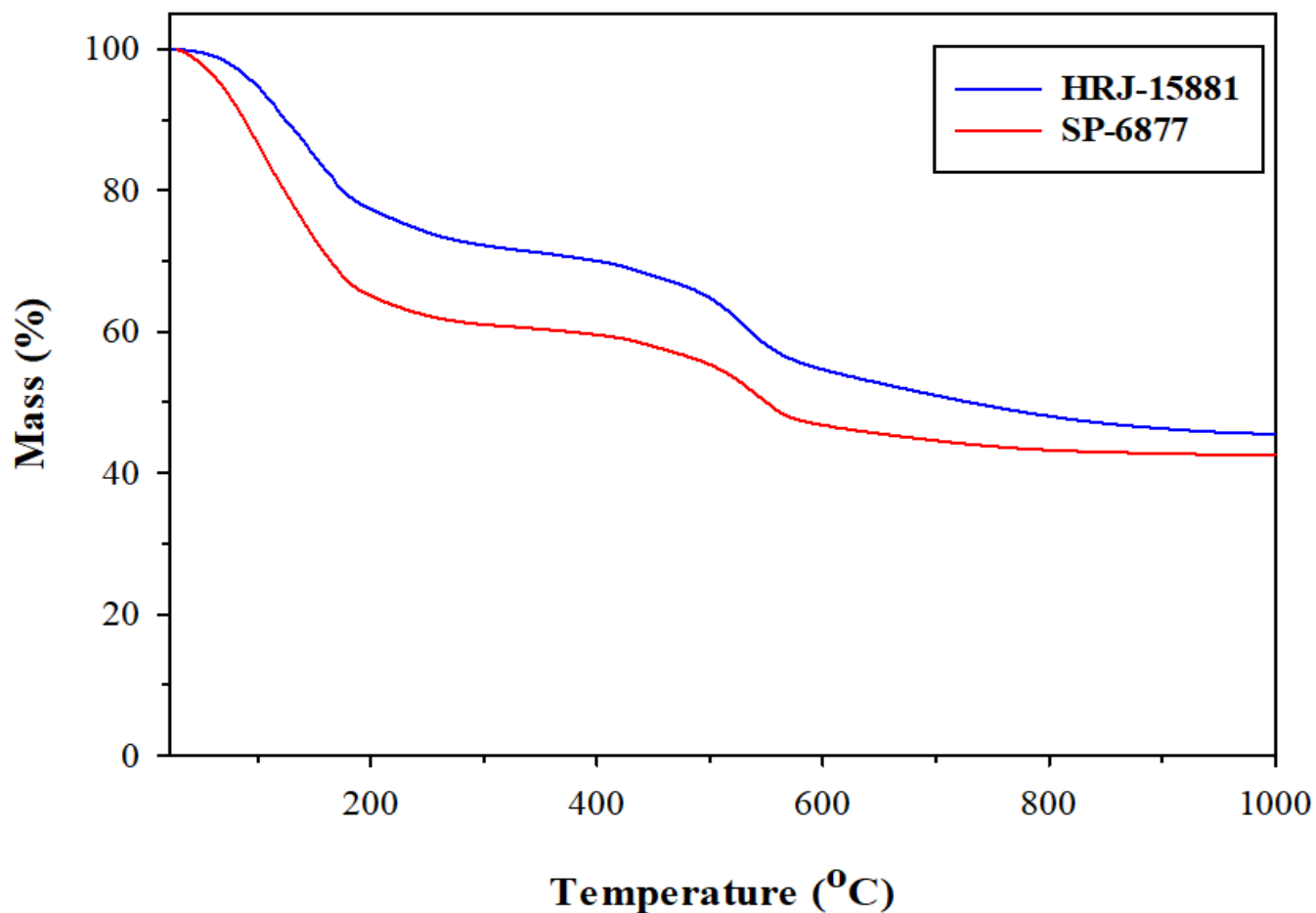


Figure 4.2. TG analysis of the as-received phenolic resins.

Table 4.2. Results of TGA showing mass loss (in %) of the phenolic resins with temperature increase.

Temperature	SP-6877	HRJ-15881
≤200 °C	32%	24%
200-600 °C	20%	21%
600-1000 °C	4.5%	8.5%

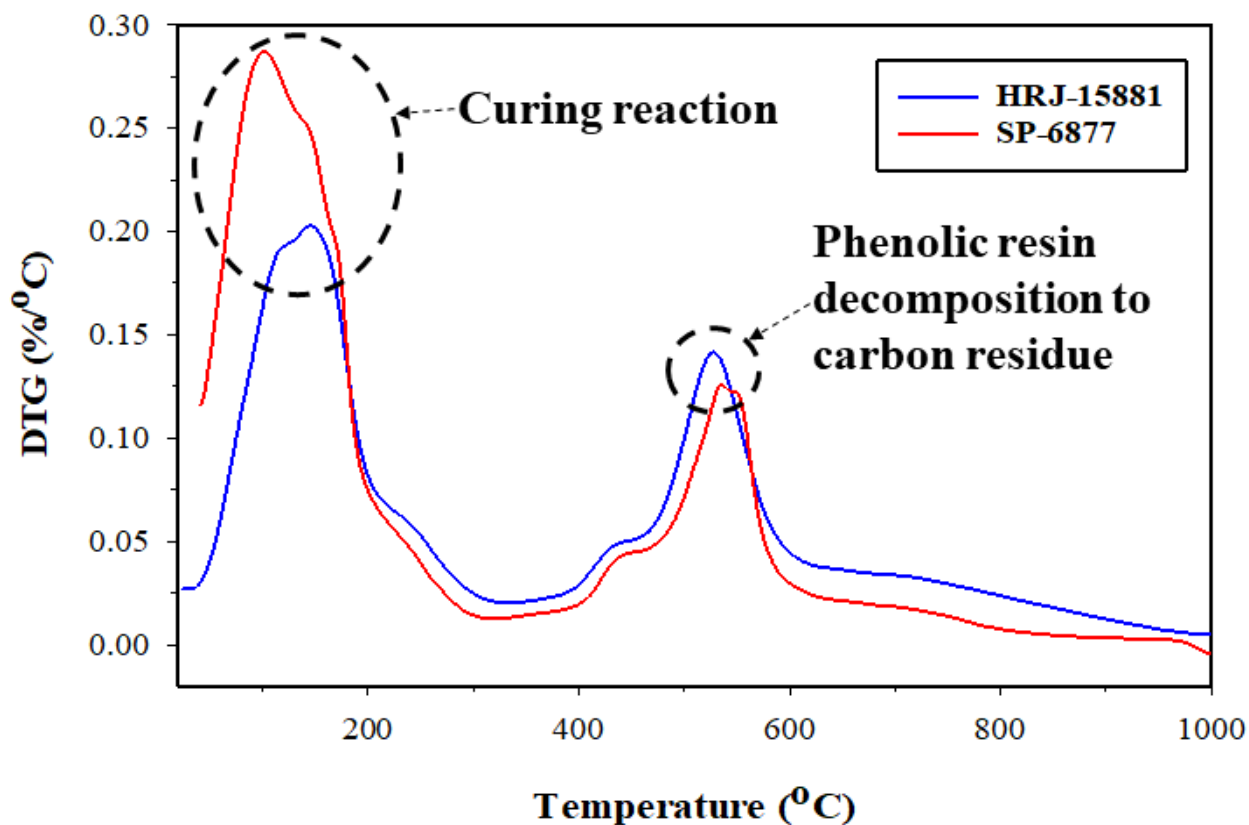


Figure 4.3. DTG plots obtained for the as-received phenolic resins.

From the TGA plot, both phenolic resins experienced more mass between room temperature and 200 °C than from about 400 to 600 °C. However, SP-6877 experienced a mass loss of 8% higher than HRJ-15881 in this temperature range. The high mass loss for both resins at temperatures less than 200 °C could be attributed to the evaporation of the solvent and other volatile materials in both resins. From the DTG plots, there are two prominent peaks for both resins; the first peak lies in the temperature range of 110-130 °C while the second lies in the range 460-550 °C. The first

peak is due to the curing reaction, while the second peak is due to the decomposition of the phenolic resin leaving behind a carbonaceous residue [104]–[106]. According to De Souza *et al.* [105], there are no significant molecular size changes up to 350 °C, only small molecular bridge transformations occur as a result of the release of volatile free molecules, notably water and phenol. As the curing reaction starts, the increase in these activated volatile free molecules gives rise to the monotonic increase in the DTG curve till it gets to the maximum temperature of 100–130 °C for both phenolic resoles. As seen in Table 3.1, both phenolic resins have equal phenol content of 13.61%. However, the HCOH (formaldehyde) content in SP-6877 is 2.6 times that of HRJ-15881 and the viscosity of HRJ-15881 is 17 times that of SP-6877. This indicates that there might be more water solvent in SP-6877 resole than in HRJ-15881. So, the higher mass loss experienced by SP-6877 at temperatures  $\leq 200$  °C as shown in Table 4.2 is due to its greater solvent content than the HRJ-15881.

The results of thermogravimetric analysis of cross-linked resins are presented in Fig. 4.4. The thermal behaviors of the two resins after they have been cross-linked are similar. The difference in mass loss as the temperature of the cured phenolic resin was increased from room temperature to 1000 °C is insignificant. This is unlike the significant difference in mass loss observed for the as-received liquid resin, i.e., TGA of as-received liquid resin in Fig. 4.2. This is not unexpected since the major difference in the two resins is in their viscosities. This difference would have been eliminated with the evaporation of the solvents in the resins during the prior curing process before the TG analysis. Beyond 350 °C, new volatile substances are released, indicating the beginning of a dehydration-condensation reaction [106]. During the dehydration-condensation reaction, molecular degradation starts, which gives rise to a reduced molecular mass of the phenolic resin. Volatiles such as H<sub>2</sub>O, CO, CO<sub>2</sub>, H<sub>2</sub>, CH<sub>4</sub>, C<sub>2</sub>H<sub>2</sub>, C<sub>2</sub>H<sub>6</sub>, phenol, and its methyl derivatives are released in the temperature range of 350–800 °C during the pyrolysis of phenolic resins [106]. The condensation of molecules from aromatic rings and volatilization of these compounds leads to weight loss and shrinkage of the phenolic resin, and at a temperature of about 700 °C, the phenolic resin is slowly converted to amorphous carbon [104], [105], [107].

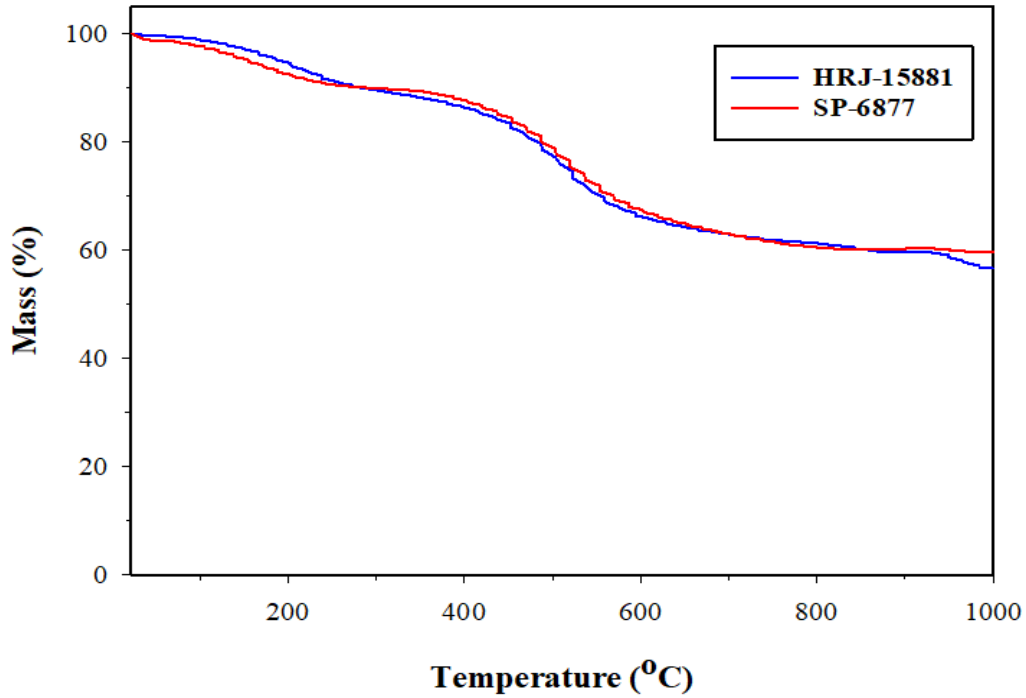


Fig. 4.4. TG analysis of cured phenolic resins.

### 4.3 Microstructural Examination of As Manufactured Carbon Fiber Reinforced Phenolic

Typical optical and scanning electron micrographs showing the microstructure of the as-fabricated carbon fiber reinforced phenolic (without microfiller addition) after curing are presented in Figs. 4.5 and 4.6, respectively. The SEM micrograph (Fig. 4.6) indicates good wetting and impregnation of the carbon fiber preforms by the phenolic resin. The good bonding between the fiber and the matrix can also be observed from the microstructures.

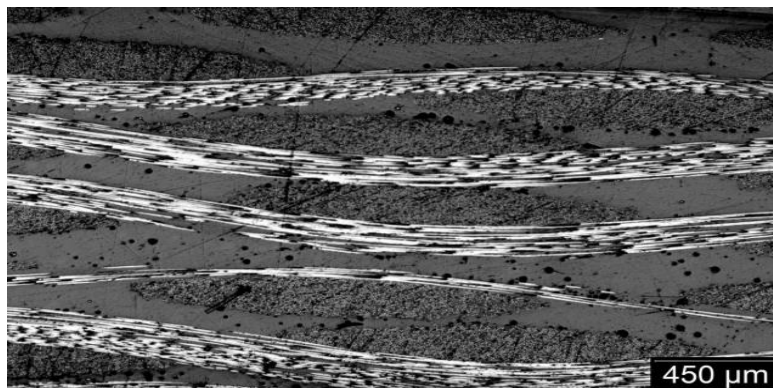


Figure 4.5. Optical micrographs of the manufactured carbon fiber reinforced phenolic matrix composite without fillers.

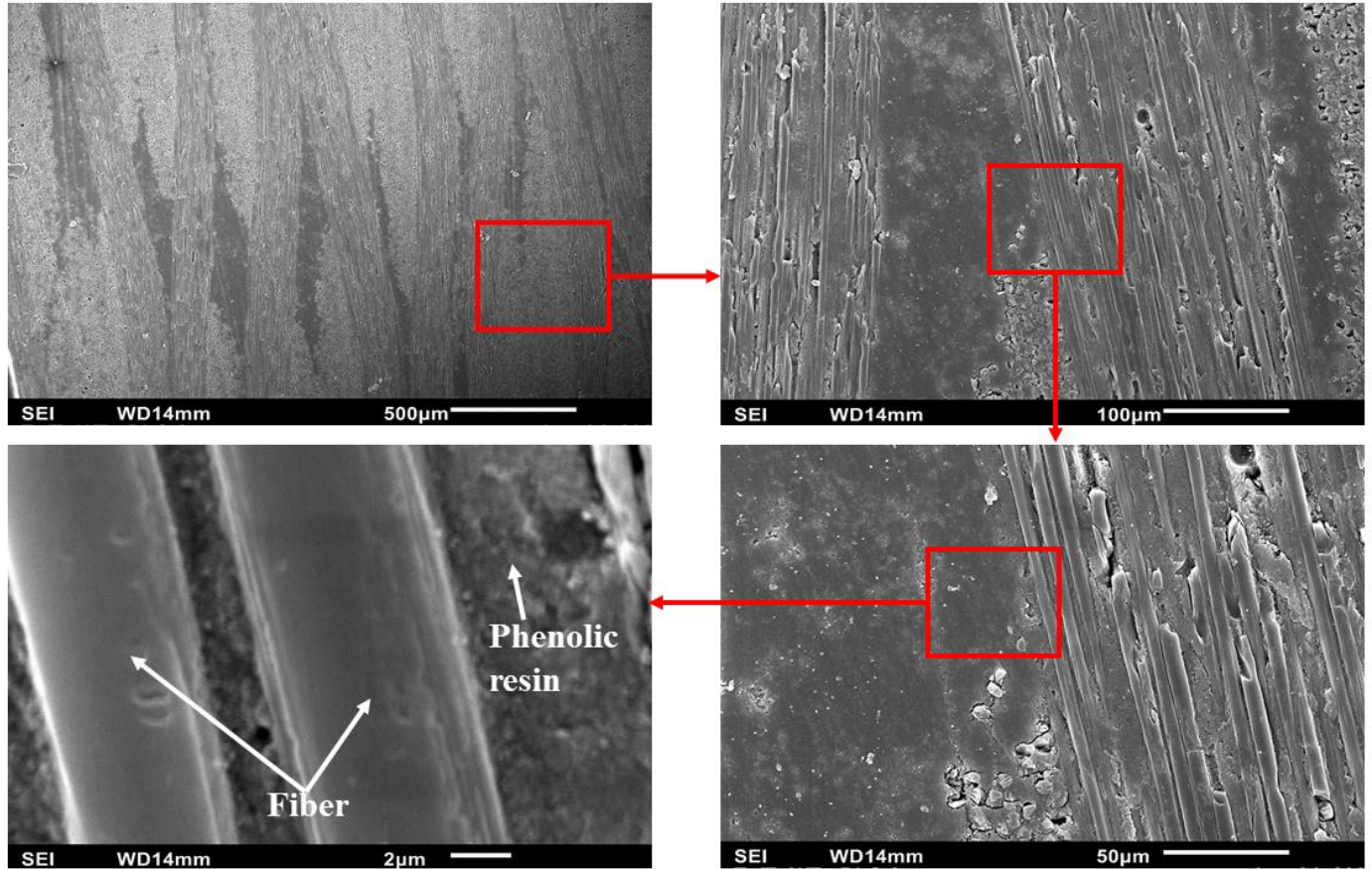
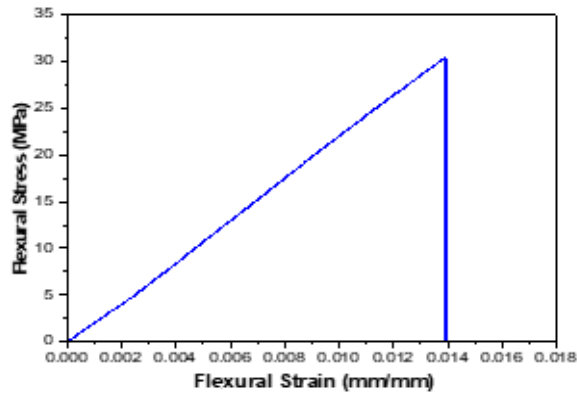


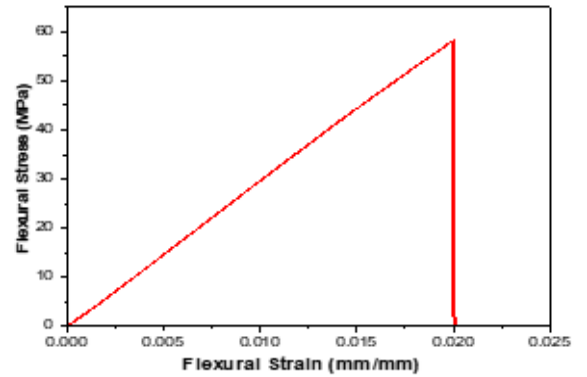
Figure 4.6. SEM micrographs of the manufactured carbon fiber reinforced phenolic matrix composite without fillers.

#### 4.4 Flexural Properties

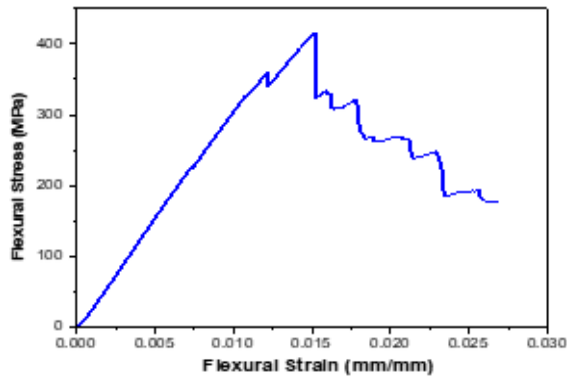
Typical flexural stress-strain curves obtained for tested samples of cured unreinforced phenolic resin and composites with and without microfillers are shown in Fig. 4.7. The carbon fiber is denoted with the acronym CF in the figure. The trends of the flexural stress-strain curve for the carbon fiber reinforced phenolic with microfillers (SiC or colloidal silica) are similar. However, the flexural-strain curve for the carbon fiber reinforced phenolic with a SiC microfiller was used as the representative of the carbon fiber reinforced phenolic with microfillers in the figure. From Fig. 4.7, it can be observed that the flexural stress-strain curves for the cured unreinforced phenolic resin are linear until the maximum stress is attained, after which a sudden drop in stress occurs, indicating brittle failure. This behavior is expected of a phenolic that is characteristically stiff and brittle [2], [5].



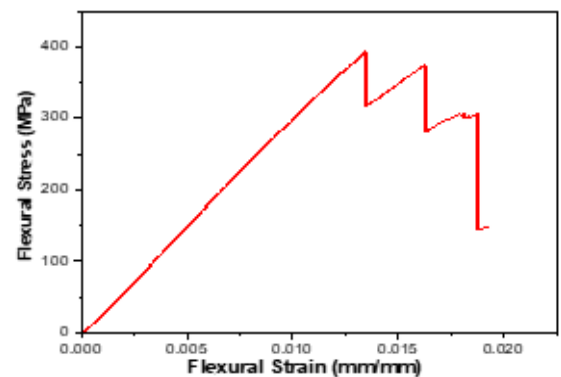
(a) SP-6877



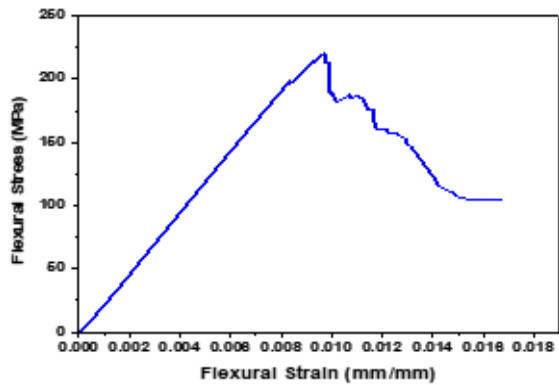
(b) HRJ-15881



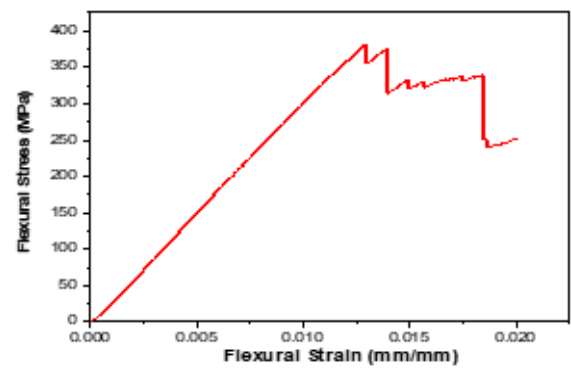
(c) SP-6877 + CF



(d) HRJ-15881 + CF



(e) SP-6877 + CF + SiC



(f) HRJ-15881 + CF + SiC

Figure 4.7. Flexural stress-strain curves for unreinforced cross-linked phenolic (a,b), carbon fiber reinforced phenolic without microfiller (c,d) and carbon fiber reinforced phenolic containing microfiller (e,f).

The flexural stress-strain curves for the carbon fiber reinforced phenolic (with or without microfiller addition) are characterized by discontinuities caused by matrix cracking or fiber rupture followed by crack bridging or deflection. The first major drop in stress in the stress-strain curves

of fiber-reinforced thermoset has been attributed to the failure of the first fiber bundle [2]. As a result of crack bridging and deflection, and the sustained ability of the matrix to transfer load between yet-to-rupture fibers, the composite material is still able to carry more load, leading to an increase in stress with strain. The intermittent increase in stress followed by a decrease before final failure stemmed from matrix cracking or fiber failure, followed by crack-deflection or crack bridging in the composite at high flexural loads.

The flexural properties of each cross-linked phenolic, with and without carbon fiber reinforcement, are compared in Fig. 4.8. Carbon fiber is denoted by the acronym CF in this figure. The addition of carbon fiber as reinforcement to the phenolic resins increased their flexural strength and modulus. The flexural strength of the carbon fiber reinforced HRJ-15881 resin is 508 % higher than that of the monolithic phenolic. Similarly, the flexural strength of the carbon fiber reinforced SP-6877 resin is approximately 909 % higher than that of monolithic SP-6877 phenolic. The flexural moduli of the CF reinforced HRJ-15881 and SP-6877 resins are respectively 930% and 1257 % higher than those of unreinforced phenolic. This improvement reflects the role of the carbon fiber as the main load-bearing component of the composite material. The phenolic matrix holds the fibers together and also protects them from environmental degradation. The load is transferred between the fiber and the matrix across the fiber-matrix interface [5]. Carbon fibers characteristically have high strength and modulus [1], [5], [36]. The high stiffness of the composites indicates good bonding between the fiber surface by the resin and a strong fiber-matrix interface.

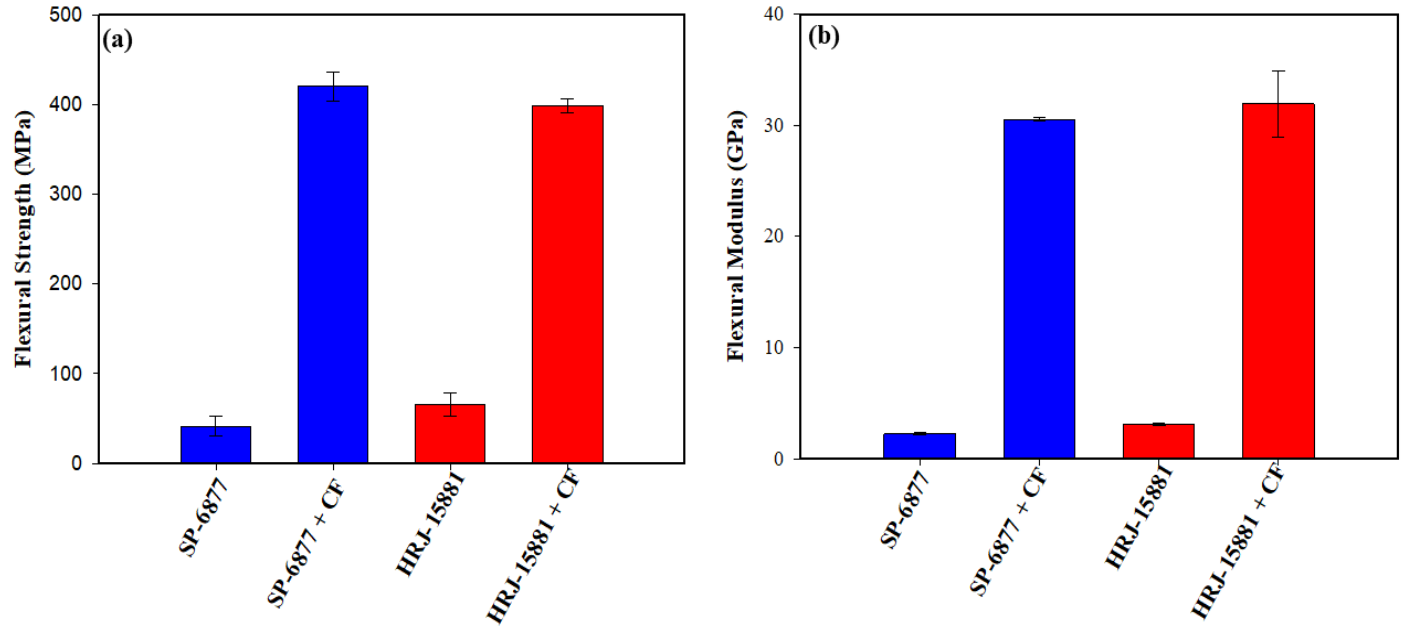


Figure 4.8. Effect of carbon fiber reinforcement on (a) flexural strength and (b) flexural modulus of cross-linked phenolic resin.

The effects of microfiller additions on the flexural properties of the carbon fiber reinforced phenolic (CFRP) are presented in Figs. 4.9 and 4.10. The composites containing no microfillers are designated by 0 wt.%, while others are designated according to the weight percent of added microfillers i.e., 0.5, 1, 1.5, and 2 wt.%. For CFRP containing no microfillers, better flexural strength was obtained for CFRP made with the SP-6877 resin as the matrix, compared to that made using HRJ-15881 resin as the matrix. However, the flexural modulus is about the same for CFRP manufactured with both phenolic resins.

For both phenolic resins, the flexural strength increased with microSiC particle addition up-to 1 wt.% before it started to decrease with further increase in filler content. The addition of microSiC particle at 0.5 wt.% gave a better flexural strength than at 1 wt.%. The main increase in flexural strength could be attributed to factors such as enhanced interfacial bonding between the fiber and the resin, as a result of the presence of SiC microfiller [108]. Furthermore, the good dispersion of the microfiller in the matrix can offer an additional load-bearing capacity to the matrix and contribute to the observed increase in flexural strength. The decrease in flexural strength at higher microfiller addition might be a result of the agglomeration of microfillers leading to a higher tendency for matrix cracking [8]–[10]. There is no improvement in the flexural modulus of CF

reinforced phenolic composites with the addition of SiC microparticles. The highest flexural moduli obtained with the addition of 0.5, 1, 1.5, and 2 wt.% SiC microparticles are less than that obtained without their addition.

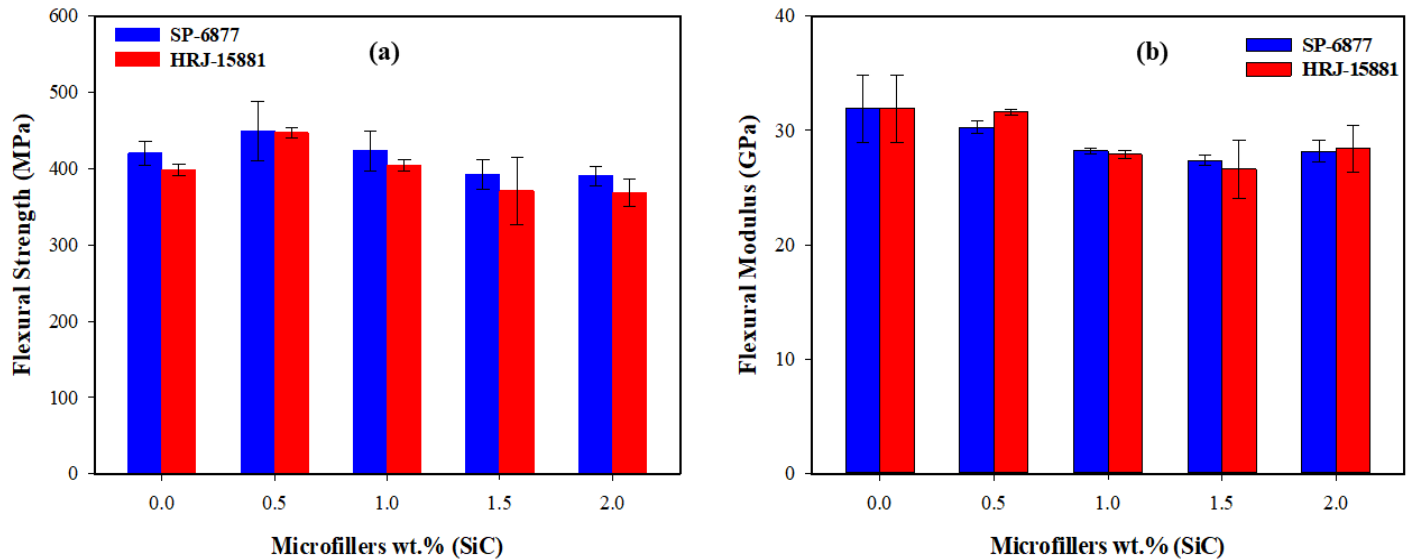


Figure 4.9. Flexural properties of CFRP composites with SiC microfiller addition: (a) flexural strength, and (b) flexural modulus.

The flexural strength and modulus of carbon fiber reinforced phenolic resins degraded with colloidal silica addition for both phenolic resins as shown in Fig. 4.10. Without colloidal silica addition, the flexural strength of CFRP composites made with SP-6877 resin is slightly higher than that made with HRJ-15881 resin. However, with colloidal silica addition, the flexural strength and flexural modulus of CFRP composites made from SP-6877 resin are lower than their HRJ-15881 resin counterparts at an addition of 0.5 -1.5 wt.%. It is not clear why the flexural strength and flexural modulus are higher for CFRP composites made from SP-6877 resin than those made from HRJ-15881 resin at a colloidal silica addition of 2.0 wt.%. The observed reduction in flexural strength and modulus of the composites containing colloidal silica fillers may be due to the effect of particle agglomeration. Fig. 4.11 shows SEM micrographs that present evidence of agglomeration of colloidal silica particles in composites made from SP-6877 resin.

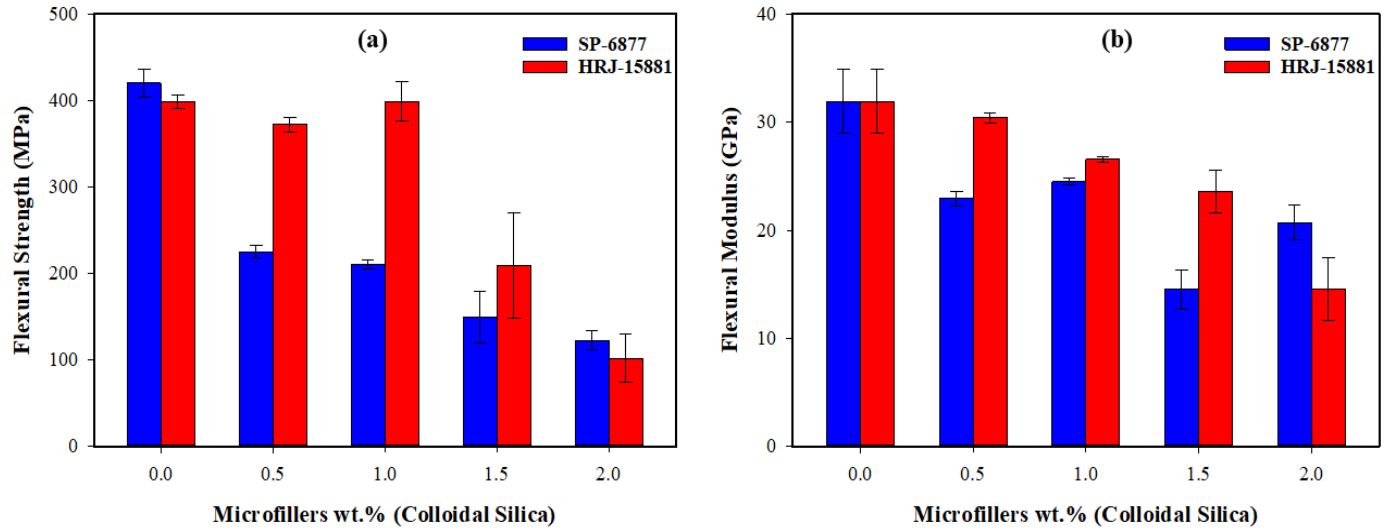


Figure 4.10. (a) flexural strength and (b) modulus of CFRP, with and without colloidal silica addition.

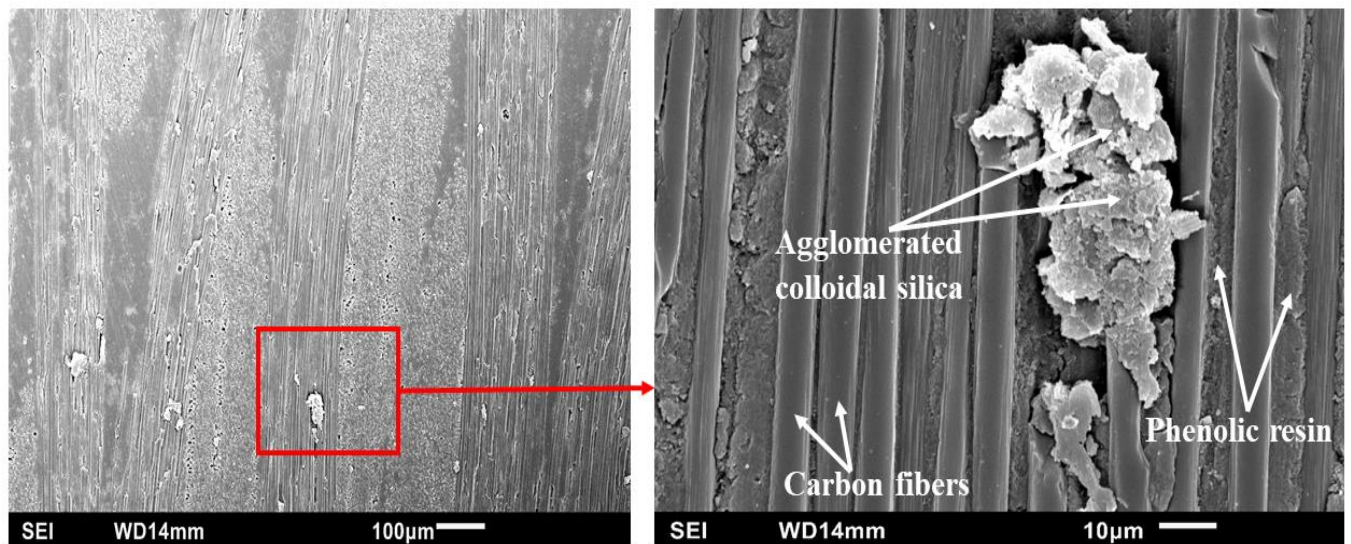


Figure 4.11. SEM micrograph showing colloidal silica agglomeration in a CFRP containing colloidal silica microfiller.

## 4.5 Dynamic Impact Properties

### 4.5.1 Dynamic impact response at impact momentum of 15 kg m/s

The results of the dynamic impact test conducted using the impact momentum of 15 kg m/s are shown in Figs. 4.12 – 4.21. The plot of true stress vs true strain for the carbon fiber reinforced phenolic matrix composite without microfillers under this loading condition is presented in Fig. 4.12. The plots of the true stress vs true strain and the maximum true stress for those of composites containing SiC microfiller are presented in Figs. 4.13 and 4.14, respectively. Charts showing the true stress vs true strain and the maximum true stress for those of composites containing colloidal silica microfiller are provided in Figs. 4.15 and 4.16, respectively.

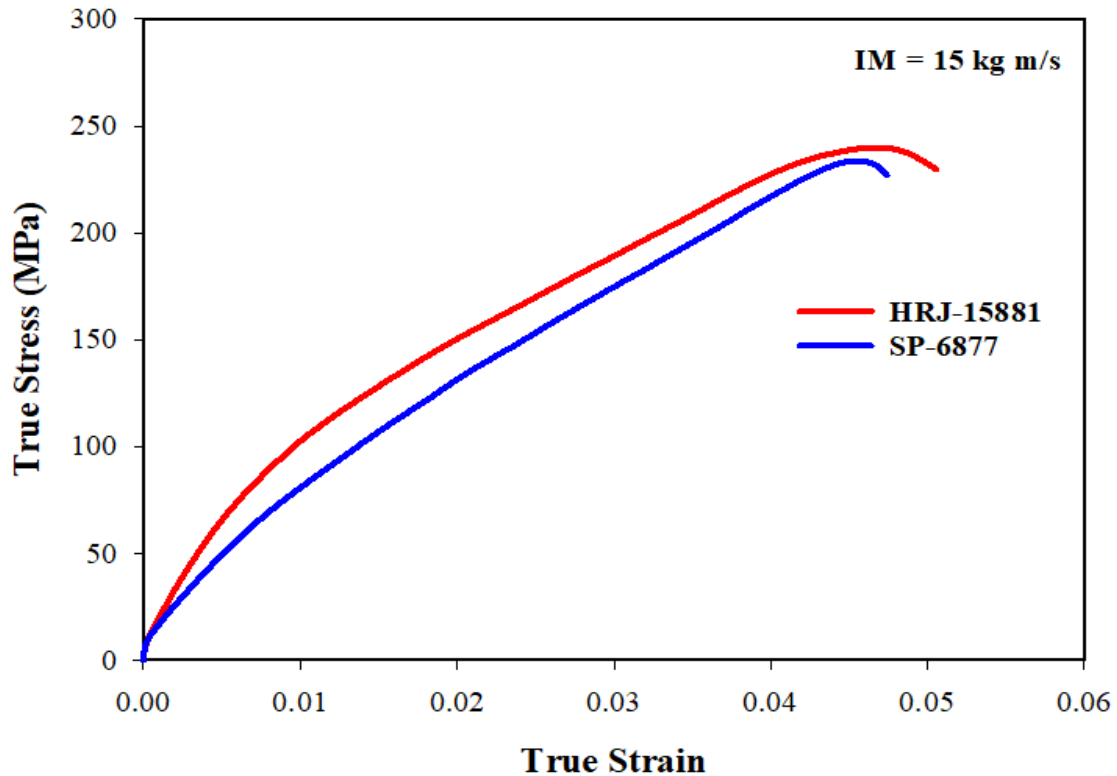


Figure 4.12. True stress-strain curve obtained for CFRPs without microfillers at an impact momentum of 15 kg m/s.

Without microfiller addition, the CFRP made with HRJ-15881 resin (with lower formaldehyde content) has better impact strength than that made with SP-6877 resin (Fig. 4.12). With the addition of SiC microfillers, the impact strength of the CFRP composites that were made with HRJ-15881 resin increased up to 1.5 wt.% microfiller addition and decreased with further increase in

microfiller content to 2.0 wt. % SiC (Fig. 4.13 and 4.14). However, there was a decrease in impact strength from 0.5 – 1 wt.% and an increase from 1 - 1.5 wt.% SiC addition. Despite this decrease and increase in impact strength at this varying microfiller content, the CFRP made with HRJ-15881 resin all had better impact strength with  $\leq 1.5$  wt.% SiC addition than its CFRP counterpart without SiC. For SP-6877 resin, the impact strength improved up to 0.5 wt.%, beyond which the impact strength started to decrease with further increase in SiC content.

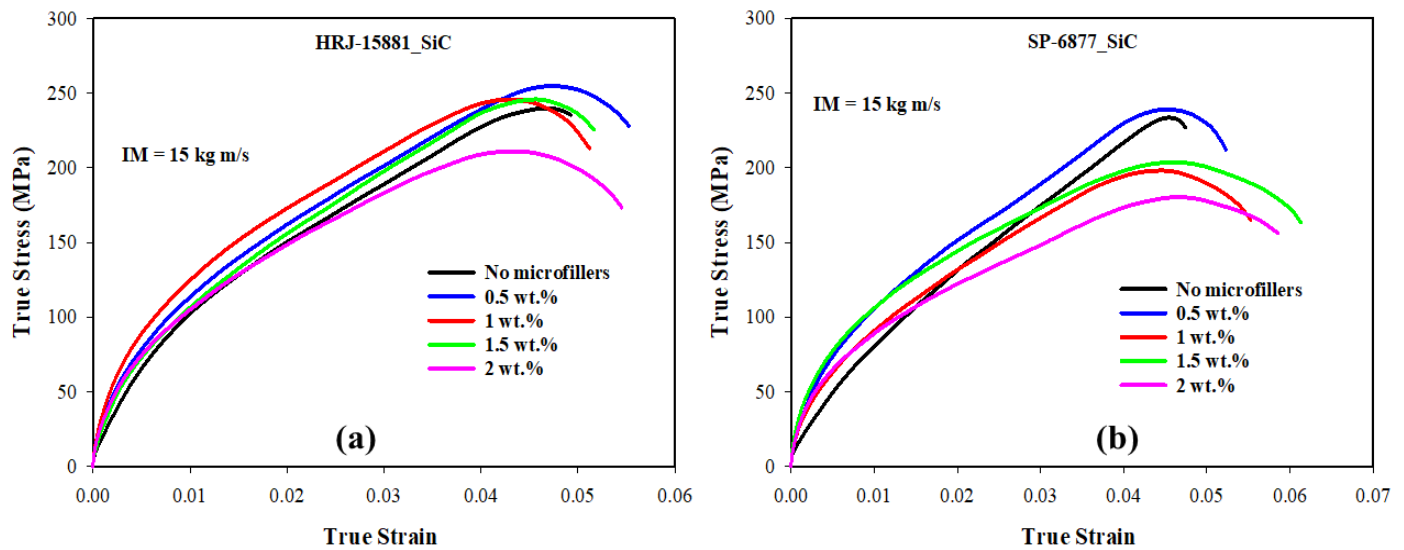


Figure 4.13. True stress-strain curves obtained for CFRPs containing SiC microfiller at an impact momentum of 15 kg m/s: (a) HRJ-15881 (b) SP-6877.

The maximum true stress of the CFRP containing SiC microfiller under 15 kg m/s impact loading is shown in Fig. 4.14. The figure reiterates the observed trend from the true stress-strain curve in Fig. 4.12 and it also shows that the CFRP made with HRJ-15881 resin had higher impact strength than those made with SP-6877 resin, with or without SiC microfiller addition.

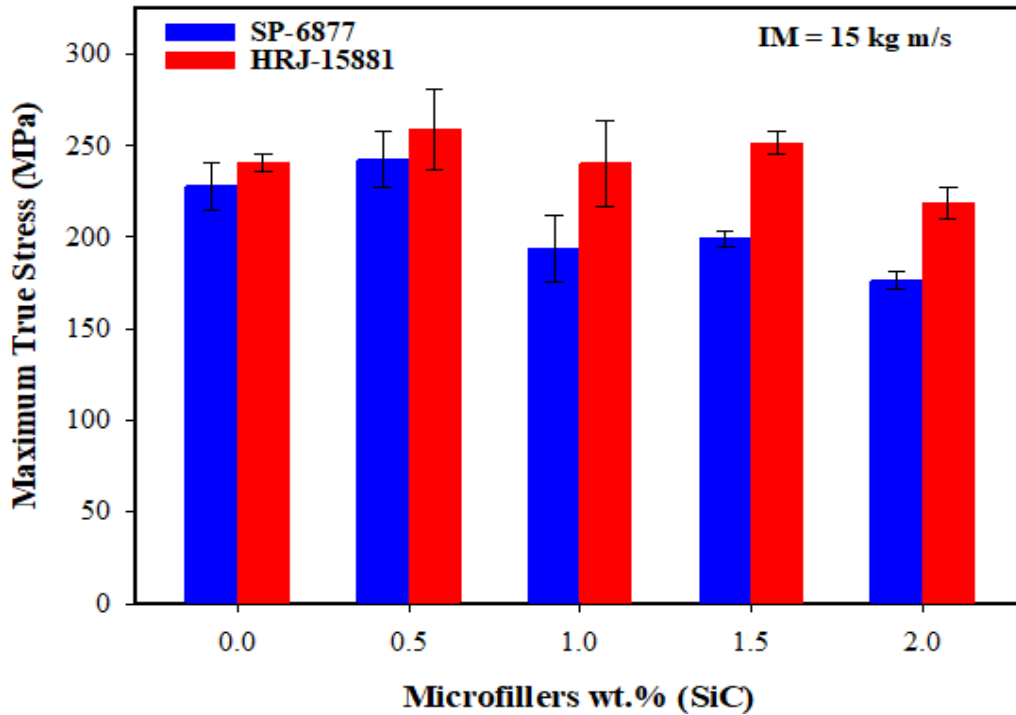


Figure 4.14. Maximum true stress obtained for CFRPs containing SiC microfillers at an impact momentum of 15 kg m/s.

For the CFRP containing colloidal silica microfiller, the impact strength did not improve with colloidal silica addition (Fig. 4.15) but deteriorated with colloidal silica addition. This deterioration in properties is due to the colloidal agglomeration and it is in agreement with the degradation in flexural properties with colloidal silica addition. However, with colloidal silica addition to the phenolic resins, the CFRP composites manufactured using HRJ-15881 resin had higher impact strength than those made using SP-6877 resin, at all microfiller addition as shown in Fig. 4.16. It was observed that the impact strength consistently deteriorated with increasing colloidal silica addition for the CFRP made with SP-6777 resin.

However, for the CFRP made with HRJ-15881 resin, the impact strength decreased up to 1 wt.% colloidal silica addition and suddenly increased from 1 – 1.5 wt.% colloidal silica addition. This reduction in impact strength up to 1 wt.% colloidal silica addition is attributed to the particle agglomeration, but it is not clear what might be responsible for the sudden increase in impact strength from 1 - 1.5 wt.% colloidal silica addition.

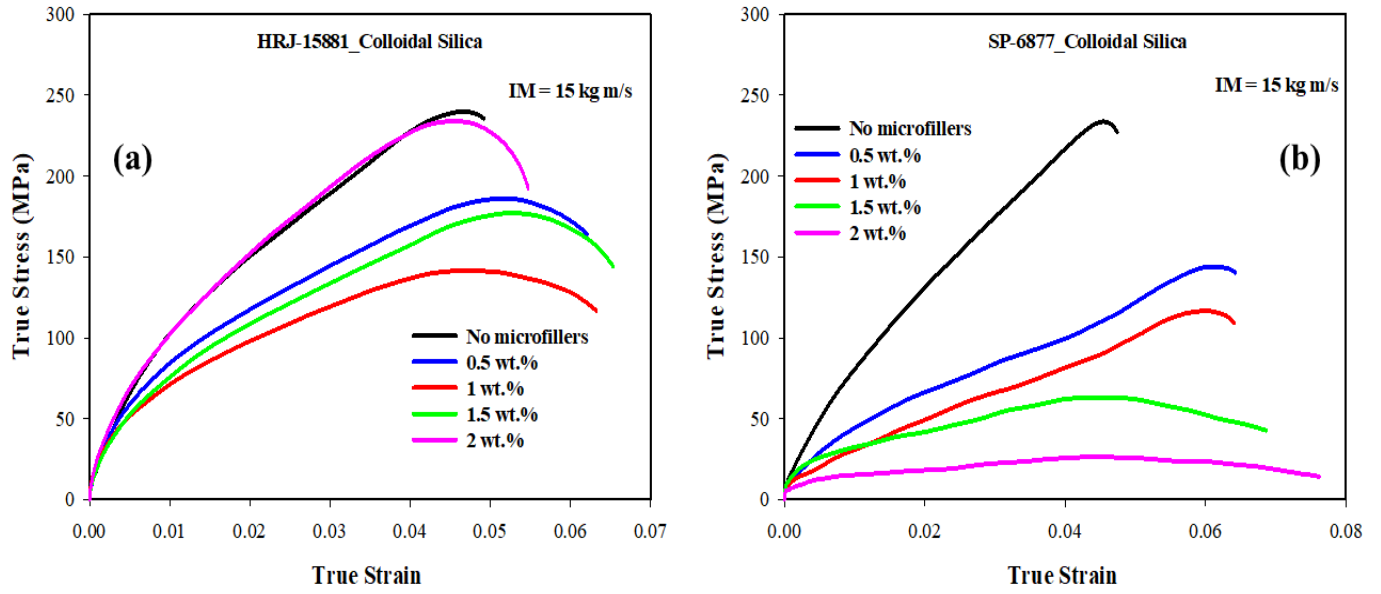


Figure 4.15. True stress-strain curves obtained for CFRPs containing colloidal silica microfiller at an impact momentum of 15 kg m/s: (a) HRJ-15881 (b) SP-6877.

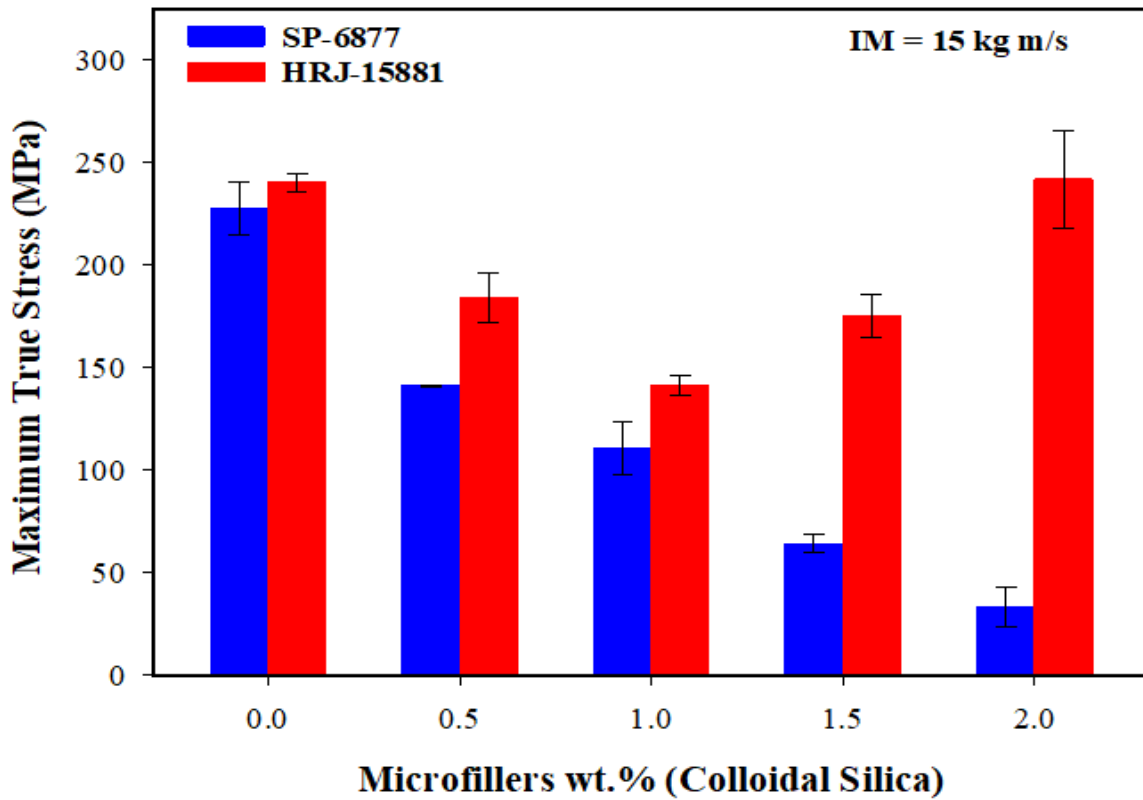


Figure 4.16. Maximum true stress obtained for CFRPs containing colloidal silica microfillers at an impact momentum of 15 kg m/s.

#### 4.5.2 Dynamic impact response at impact momentum of 28 kg m/s

The results of the dynamic impact test on the carbon fiber reinforced phenolic matrix composites are presented in Figs. 4.17 - 4.21. The true stress vs true strain curve for CFRP composites containing no microfillers is provided in Fig. 4.17. The true stress vs true strain curve and maximum true stress of the composites containing SiC microfillers are presented in Figs. 4.18 and 4.19, respectively. The charts of the true stress vs true strain and maximum true stress of the composites containing colloidal silica microfillers are presented in Figs. 4.20 and 4.21, respectively.

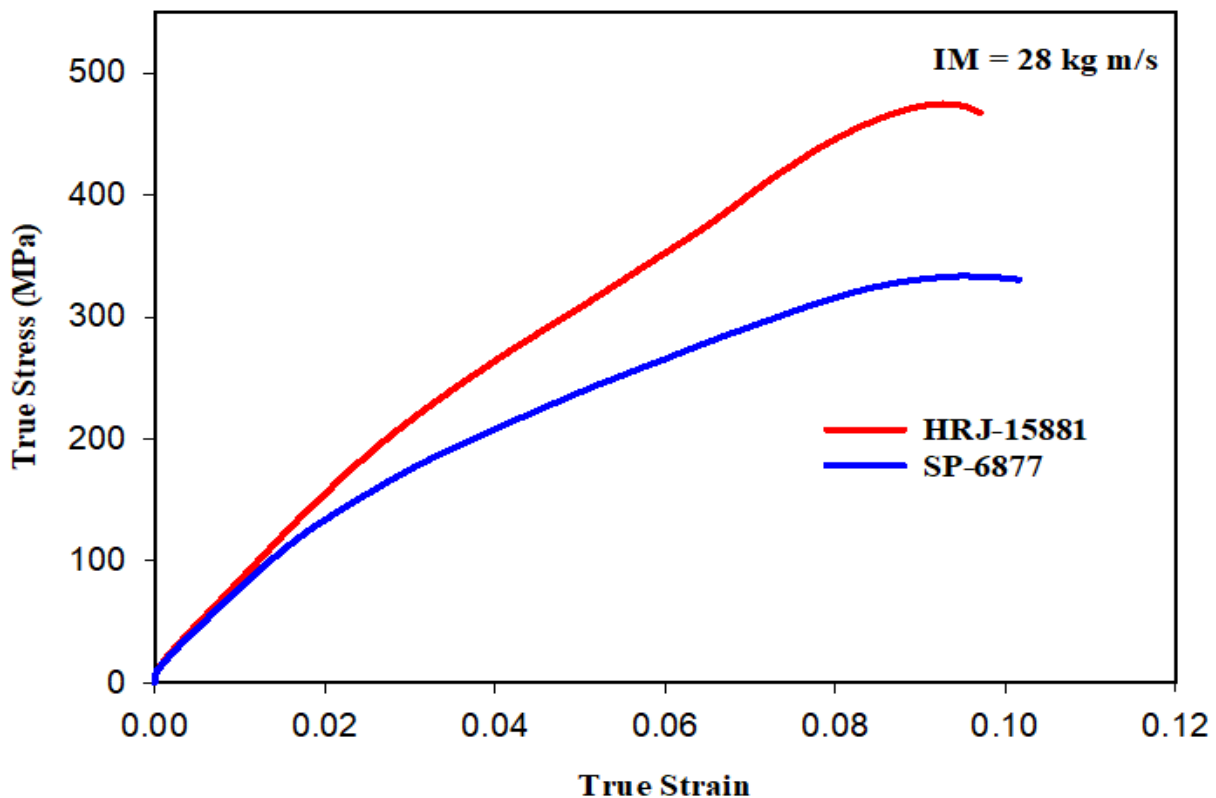


Figure 4.17. True stress-strain curve obtained for CFRPs without microfillers at an impact momentum of 28 kg m/s.

For the CFRP composites containing no microfillers, the HRJ-15881 resin has higher impact strength than the SP-6877 resin (Fig. 4.17), which is in agreement with the obtained results for composites impacted at a momentum of 15 kg m/s. Also, with SiC addition (Figs. 4.18 and 4.19), higher impact strength was obtained for the CFRP made with HRJ-15881 resin than those made

using SP-6877 resin. From the true stress-strain curve in Fig. 4.18, the impact strength increased with SiC addition up to 0.5 wt.%, beyond which it started to decrease for the CFRP made with SP-6877 resin. Despite this decrease in impact strength, the CFRP made with SP-6877 resin at all SiC additions have better impact strength than its CFRP counterpart without microfillers. However, the impact strength of CFRP made with HRJ-15881 resin increased with the addition of 0.5 wt.% SiC microfiller. It decreased when the SiC microfiller content was increased beyond 0.5 wt.% SiC.

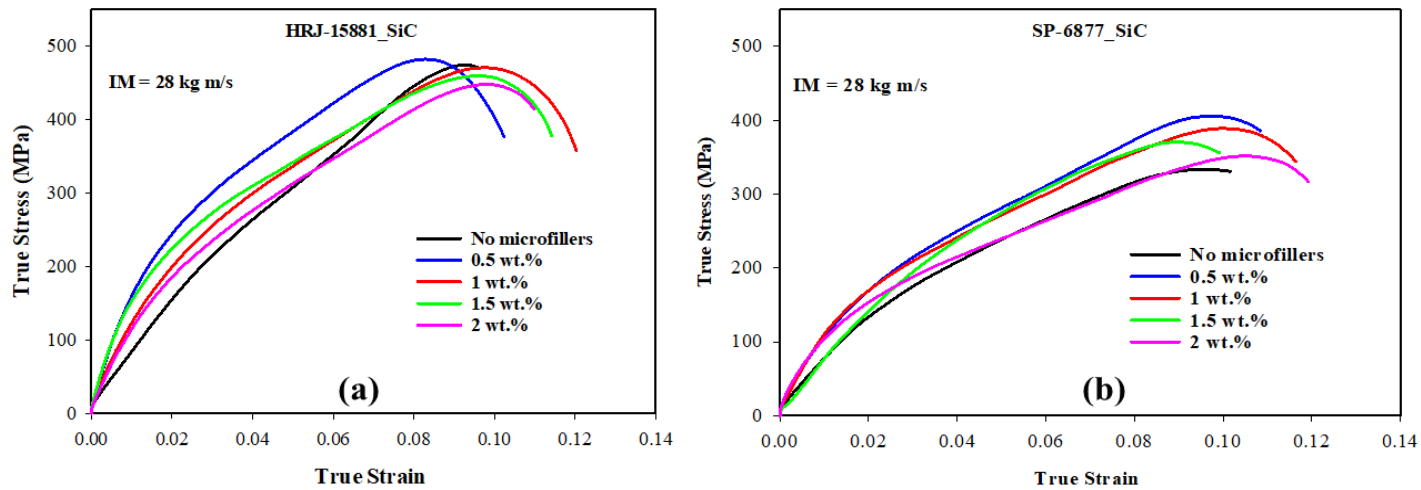


Figure 4.18. True stress-strain curves obtained for CFRPs containing SiC microfiller at an impact momentum of 28 kg m/s: (a) HRJ-15881 (b) SP-6877.

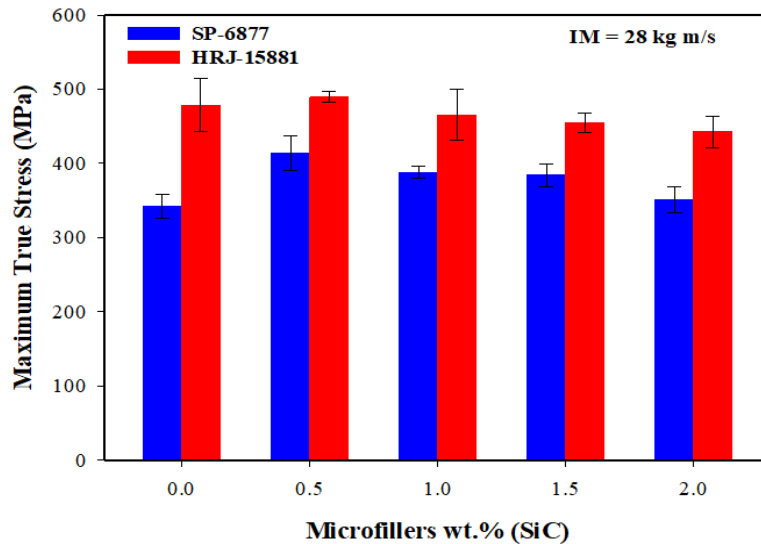


Figure 4.19. Maximum true stress obtained for CFRPs containing SiC microfillers at an impact momentum of 28 kg m/s.

The addition of colloidal silica did not result in any noticeable improvement in the impact strength of the CFRP produced using both phenolic resins as shown in Figs. 4.20 and 4.21. However, the CFRP made with HRJ-15881 resin had higher impact strength than that made with SP-6877 resin at all colloidal silica addition. It was observed that the impact strength consistently deteriorated with increasing colloidal silica addition for the CFRP made with SP-6777 resin, confirming the particle agglomeration. However, for the CFRP made with HRJ-15881 resin, the impact strength decreased up to 1 wt.% colloidal silica addition and suddenly increased from 1 – 1.5 wt.% colloidal silica addition. To a great extent, the trend of the impact strength results obtained at impact momentums of 15 and 28 kg m/s are similar to one another.

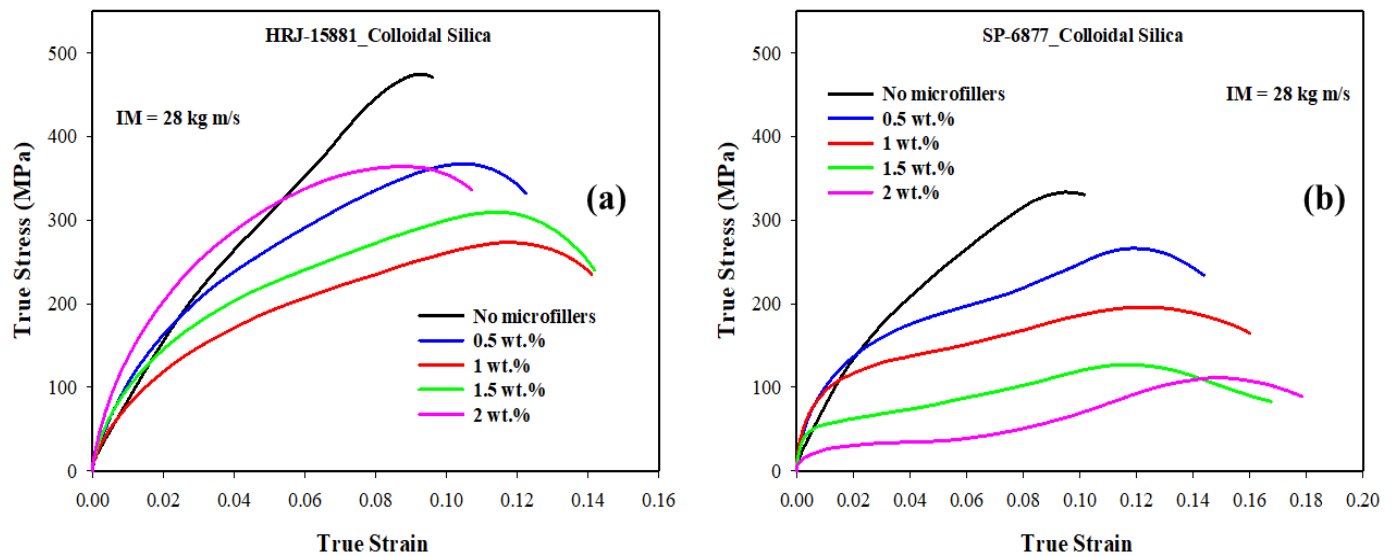


Figure 4.20. True stress-strain curves obtained for CFRPs containing colloidal silica microfiller at an impact momentum of 28 kg m/s: (a) HRJ-15881 (b) SP-6877.

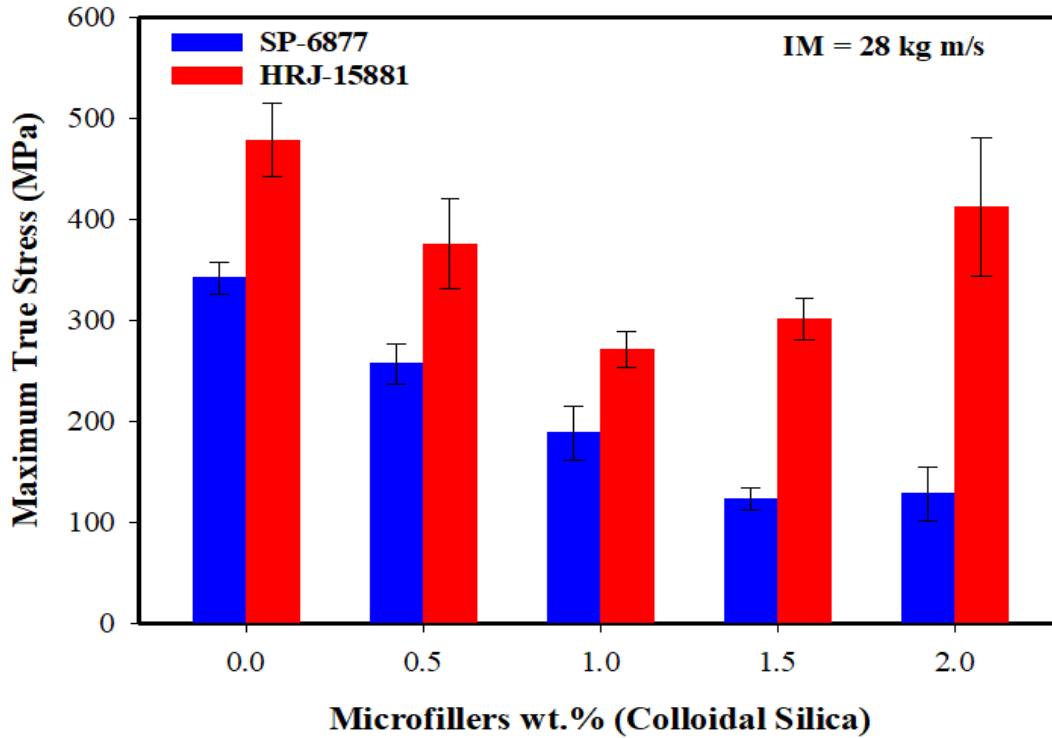


Figure 4.21. Maximum true stress obtained for CFRPs containing colloidal silica microfillers at an impact momentum of 28 kg m/s.

From the results obtained above, it is evident that the addition of SiC microfiller to the phenolic resins is beneficial to the impact response of the CFRP made from the resins. On the other hand addition of colloidal silica rather degrade the impact performance of the composite. This is the case for the two impact momenta (15 and 28 kg m/s) used in this study. To a great extent and for both microfillers, the dynamic impact properties results obtained are in agreement and similar to the results of the flexural properties with individual microfillers.

#### 4.6 Statistical Analysis

The results of the ANOVA test on the flexural properties of the composites are presented in Table 4.3 for the CFRP composites containing colloidal silica and SiC microfillers. Table 4.4 presents the ANOVA test results of the impact strength for the CFRP composite with colloidal silica and SiC microfillers at impact momentum of 15 and 28 kg m/s. When the P-value is less than 0.05 and the F ratio ( $F/F_{critical}$ ) larger than 1, the difference between the mean values is considered to be significant. From both ANOVA tables for the flexural properties, it could be observed that

differences in flexural properties of the composite samples with fillers are statistically significant except for the flexural strength of the CFRP composites made with SP-6877 resin containing SiC microfiller. However, the difference in impact strength are all statistically significant with either microfiller addition and for both resins.

Table 4.3. ANOVA test results for flexural properties of the carbon fiber reinforced phenolic (CFRP) containing microfillers.

Microfillers	Resin type	Flexural Strength			Flexural Modulus		
		P-value	F-ratio	Statistically significant	P-value	F-ratio	Statistically significant
Colloidal Silica	HRJ-15881	0.000	49.1	Yes	0.000	44.7	Yes
	SP-6877	0.000	25.7	Yes	0.000	35.6	Yes
SiC	HRJ-15881	0.014	6.70	Yes	0.028	5.2	Yes
	SP-6877	0.071	3.46	No	0.003	11.2	Yes

Table 4.4. ANOVA test results for impact strength of the CFRP containing microfillers.

Microfillers	Resin type	Impact Strength – 15 kg m/s			Impact Strength – 28 kg m/s		
		P-value	F-ratio	Statistically significant	P-value	F-ratio	Statistically significant
Colloidal Silica	HRJ-15881	0.000	26.244	Yes	0.027	2.115	Yes
	SP-6877	0.000	91.834	Yes	0.000	30.091	Yes
SiC	HRJ-15881	0.035	3.718	Yes	0.041	1.4321	Yes
	SP-6877	0.000	16.099	Yes	0.016	5.178	Yes

#### 4.7 X-ray Diffraction Analysis

The XRD diffractograms obtained for carbon fiber and microfillers were compared to the standard for the purpose of properly indexing the diffraction peaks. For the carbon fiber, the indexing of the experimental diffraction peaks was done using the Mercury software (version 4.3.0) and graphite crystallographic information (.cif) file [deposition number: 918549] obtained from the Cambridge crystallographic data center (CCDC) crystal structure database. The full width at half-maximum

(FWHM) values used in simulating the theoretical diffraction pattern of graphite were 1.0, 2.0, 3.0, 4.0 and 5.0. Fig. 4.22 shows the diffraction patterns generated. As can be seen, there is a characteristic intense peak (002) at approximately  $2\theta = 26.2$ , followed by minor peaks (101) at  $2\theta \sim 44.0^\circ$ , and (004) at  $2\theta \sim 54.0^\circ$ . Depending on the value of FWHM used, there is an additional peak of (100) at  $2\theta \sim 42.3^\circ$  and (102) at  $2\theta \sim 50.5^\circ$ .

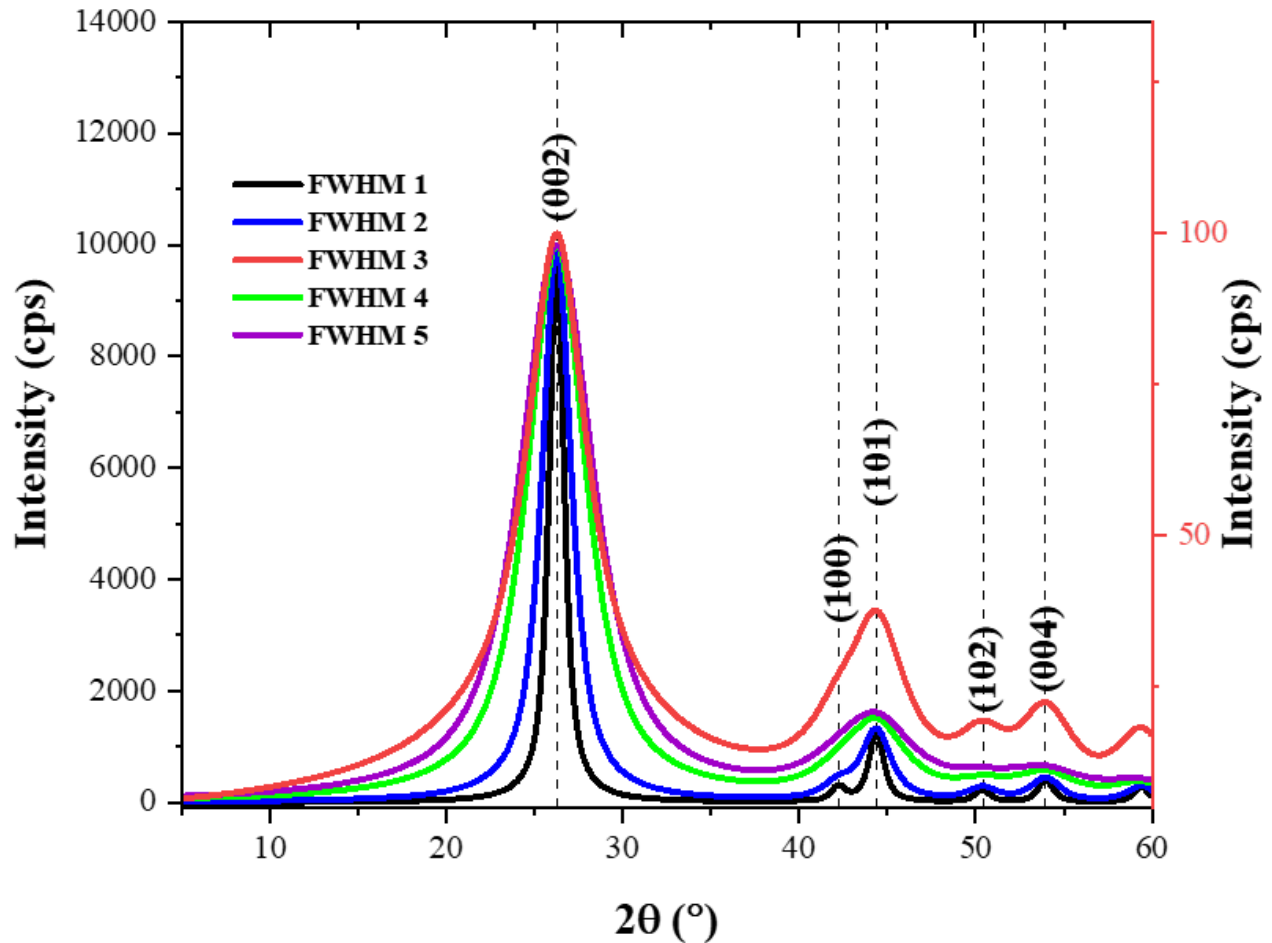


Figure 4.22. Calculated diffraction pattern obtained for graphite using different FWHM values.

It was observed that the calculated XRD diffractogram matched the XRD diffractogram of the experimental carbon fiber (Exp. CF) used in this study at FWHM of 4. The XRD diffractogram for the standard carbon fiber at FWHM of 4.0 and applied carbon fiber (in this study) was co-plotted to get the peak index of the applied carbon fiber, as shown in Fig. 4.23. The comparison revealed the index of the characteristics peak of the carbon fiber used in this study at a (002) peak at  $2\theta \sim 25.7^\circ$ , (101) peak at  $2\theta \sim 44.1^\circ$  that did not decompose into (100) peak and (004) peak at

2 $\theta$  ~ 54° that did not decompose into (102) peak. Furthermore, it was also observed that, for the experimental carbon fiber, a 0.5° difference was obtained for (002) peak, a 0.1° difference for (101) peak, when compared with the calculated XRD diffractogram. In addition, no difference was observed with the (004) peak, both for the experimental and the calculated XRD diffractogram.

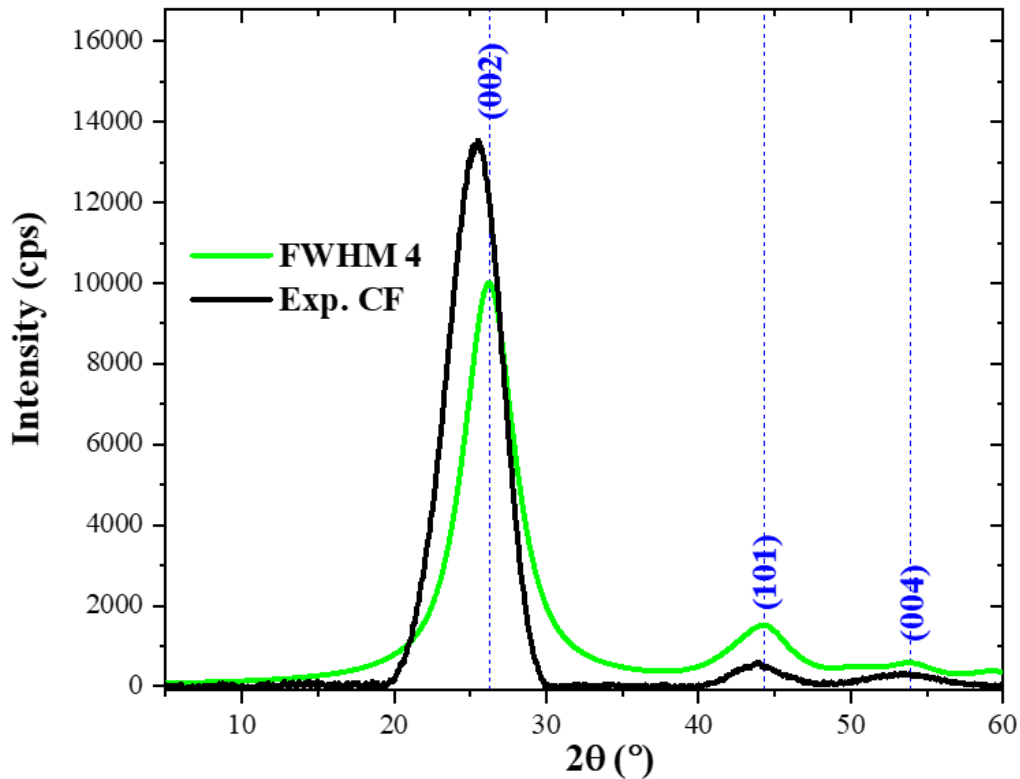


Figure 4.23. Comparison of diffraction pattern for calculated graphite (carbon) at FWHM of 4 and Experimental carbon fiber (Exp. CF).

SiC can crystallize in different polytypes and the most stable structures are the  $\alpha$ -SiC (6H hexagonal) and  $\beta$ -SiC (3C-cubic) [109], [110].  $\alpha$ -SiC are formed at temperatures greater than 1700 °C and has a hexagonal crystal structure while  $\beta$ -SiC are formed at temperatures below 1700 °C and has a cubic crystal structure. Moissanite is a naturally occurring silicon carbide with 6H polytype [111], so, the SiC used in this study was compared with Moissanite as standard. The Moissanite cif. used was obtained from the American mineralogy crystal structure database (AMCSD). Its XRD pattern was indexed with the aid of the Mercury software using a FWHM value of 0.6 because this FWHM value generated a diffraction pattern that looked closest to the

SiC used in this study as shown in Fig. 4.24. The AMSCD characteristic features the  $\alpha$ -SiC are diffraction peaks (101), (102), (103), (104), (105), (107) and (108) peaks at  $2\theta \sim 34.2^\circ$ ,  $35.7^\circ$ ,  $38.3^\circ$ ,  $41.4^\circ$ ,  $45.3^\circ$ ,  $54.7^\circ$ , and  $60.9^\circ$  respectively. A majority of these peaks appeared in the SiC used in this study, which indicates that it is  $\alpha$ -SiC.

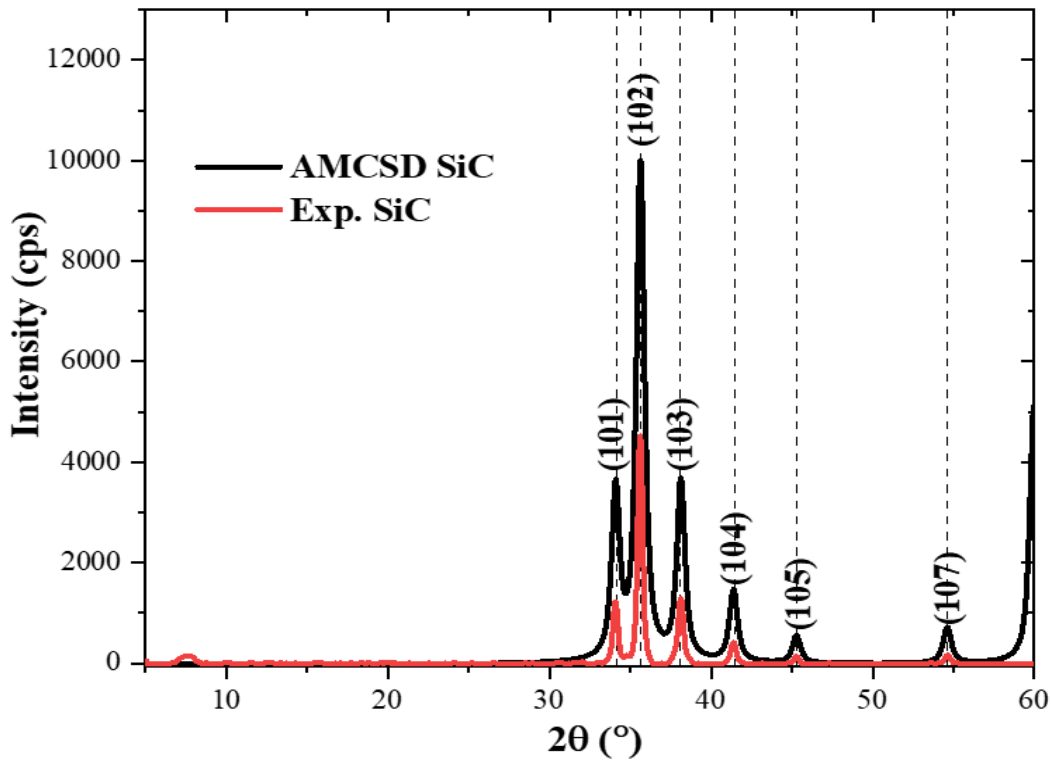


Figure 4.24. Calculated X-ray pattern of  $\alpha$ -SiC obtained from American mineralogy crystal structure database (AMCSD) compared with that of the SiC used in the present study (Exp. SiC).

The X-ray diffraction pattern obtained for CFRP composites made from the two resins are compared with those obtained for monolithic resins and carbon fiber in Fig. 4.25. The addition of carbon fiber to the two resins to form CFRP composites resulted in the existence of two prominent peaks at  $2\theta \sim 18.6^\circ$  and  $25.7^\circ$  for SP-6877 resin and  $18.8^\circ$  and  $25.7^\circ$  for HRJ-15881 resin. The presence of these peaks in the CFRP without fillers is a result of the constituent materials retaining their identities after manufacturing. It could also be observed that the phenolic resin (002) peak decreased for the SP-6877, probably owing to its low viscosity.

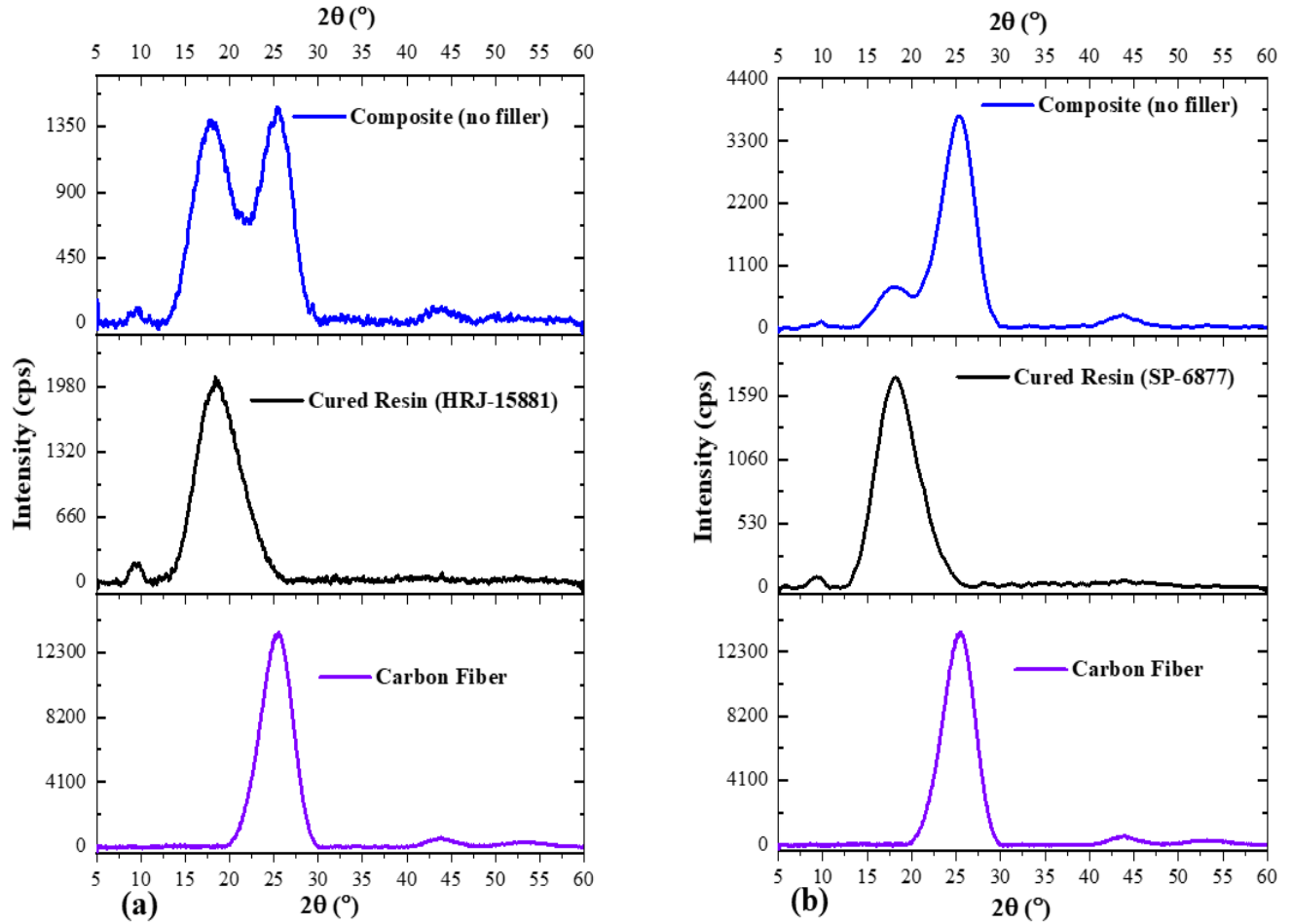


Figure 4.25. XRD diffractograms showing constituent materials for CFRP composite made with (a) HRJ-15881 and (b) SP-6877 phenolic resin.

The resulting changes in XRD diffractogram with SiC and colloidal silica addition to the CFRP composite are documented in Figs. 4.26 and 4.27, respectively, for both phenolic resins. With SiC addition to the CFRP, the phenolic resin (002) peak decreased for the CFRP composite made with each phenolic resin. In a work carried out by Sekhar *et al.* [23], where they studied the mechanical, thermal, and rheological studies of phenolic resin modified with intercalated graphite (graphite bisulfate). In the author's characterization technique, they compared the XRD diffractogram of natural graphite and their intercalated graphite. They reported that the characteristics diffraction peak of the intercalated graphite shifted to the left and reduced in intensity when compared with the characteristics peak of the natural graphite. Owing to the decrease and shifting to the left of the characteristics peak of the intercalated graphite, they concluded that their intercalated graphite

truly intercalates and contains bisulfate. In another work by Ki Park *et al.* [112] to study the electrochemical and structural evolution of structured microspheres  $V_2O_5$  during  $Li^+$  intercalation, the authors reported progressive changes in characteristics peak of the  $V_2O_5$  as phase transformation occurred during  $Li^+$  intercalation. For example, a (001) characteristics peak belonging to the  $V_2O_5$  shifted towards a lower diffraction angle. The authors stated that this shift is associated with the transformation of  $\alpha-V_2O_5$  to  $Li_x V_2O_5$  when  $Li^+$  was first intercalated. In relation to the present study, it could be inferred that as the (002) diffraction peak of the phenolic resin decreases, the SiC has penetrated the phenolic resin matrix. Furthermore, a (102) peak, which is a characteristics feature of the  $\alpha$ -SiC existed at  $35.7^\circ$  for the CFRP composite made with each phenolic resin containing SiC. The presence of the  $\alpha$ -SiC peak further confirms the presence of SiC that is intercalated in the phenolic resin matrix.

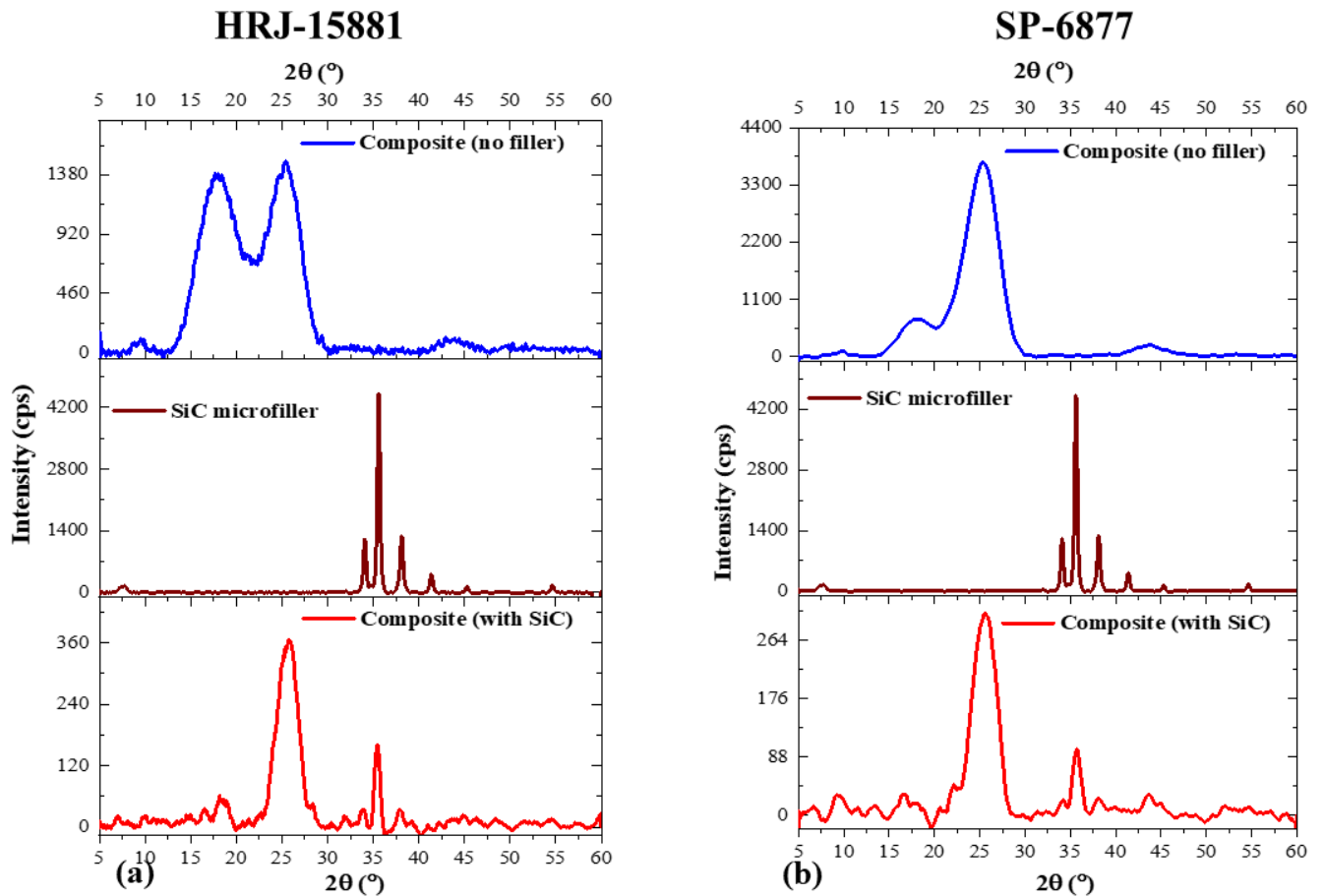


Figure 4.26. XRD diffractograms showing the effect of SiC microfiller addition on the CFRP composite made with (a) HRJ-15881 and (b) SP-6877 phenolic resin.

The addition of the colloidal silica to the CFRP composites decreased and eliminated the phenolic resin (002) peak for HRJ-15881 and SP-6877 respectively. The decrease of the phenolic resin (002) peak for HRJ-15881 shows that the colloidal silica is present in the matrix of the CFRP [23], [112]. However, the phenolic resin (002) peak elimination in the CFRP made with SP-6877 phenolic resin containing colloidal silica might be because of the colloidal silica inhomogeneous distribution, agglomeration, and non-presence in strategic sites. Perhaps, this explains its deterioration in both the flexural and dynamic impact properties, when compared to the CFRP made with HRJ-15881 containing colloidal silica as obtained in section 4.4 and 4.5.

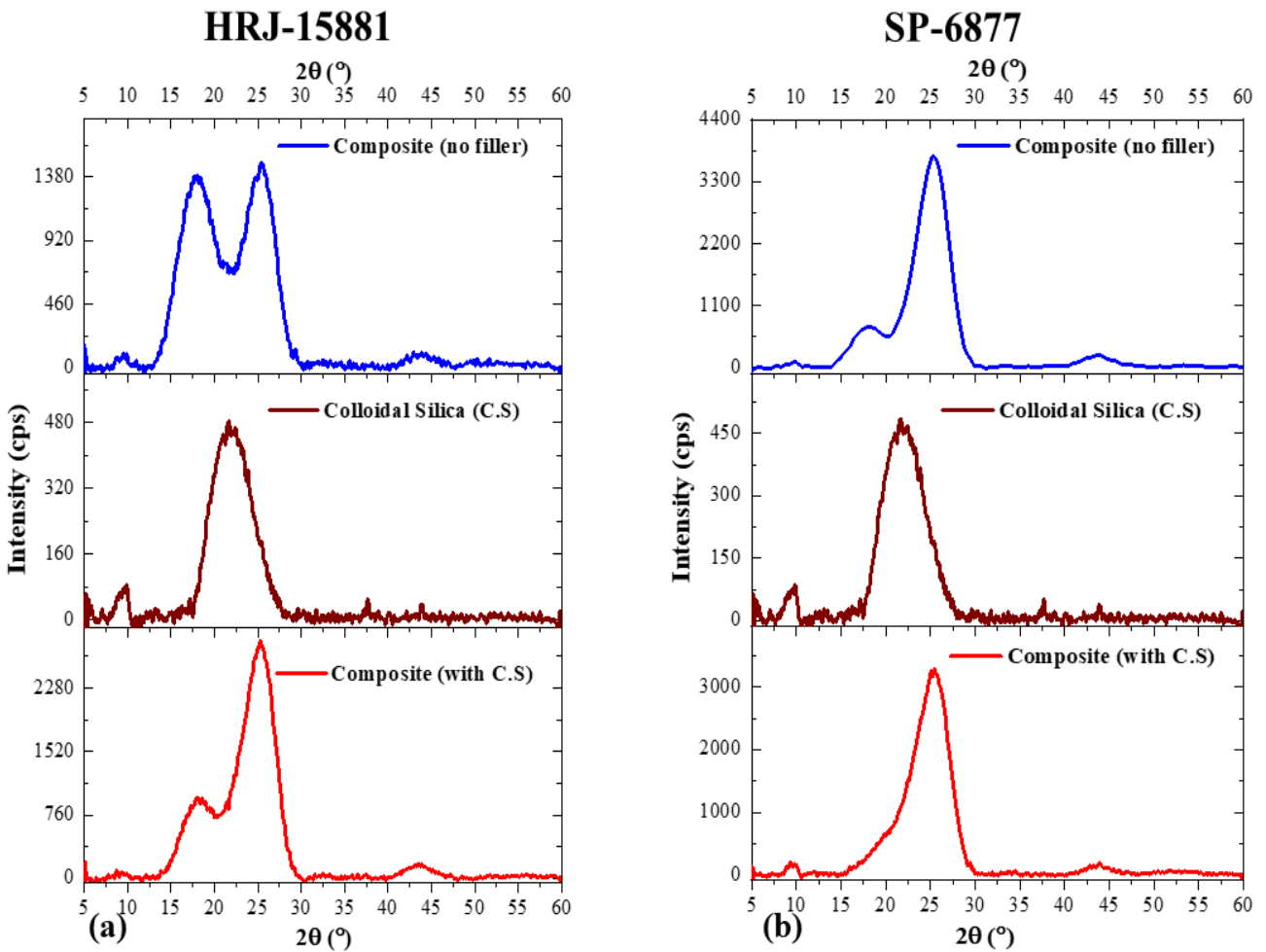


Figure 4.27. XRD diffractograms showing the effect of colloidal silica microfiller addition on the CFRP composite made with (a) HRJ-15881 and (b) SP-6877 phenolic resin.

The resulting changes in XRD diffractogram of phenolic resins as a result of the addition of SiC and colloidal silica microfillers are shown in Figs. 4.28 and 4.29 respectively. The addition of the SiC microfiller to both phenolic resins resulted in the existence of a (002) diffraction peak at  $2\theta \sim 18.4^\circ$  for phenolic resin, and a (101), (102) and (103) peaks at  $2\theta \sim 34.2^\circ$ ,  $35.7^\circ$ ,  $38.3^\circ$  respectively, which are the characteristics feature of the  $\alpha$ -SiC used in this study, as obtained from the AMCSD standard. The presence of these peaks confirms that the SiC microfillers are present and intercalated in the phenolic resin matrix [23], [112].

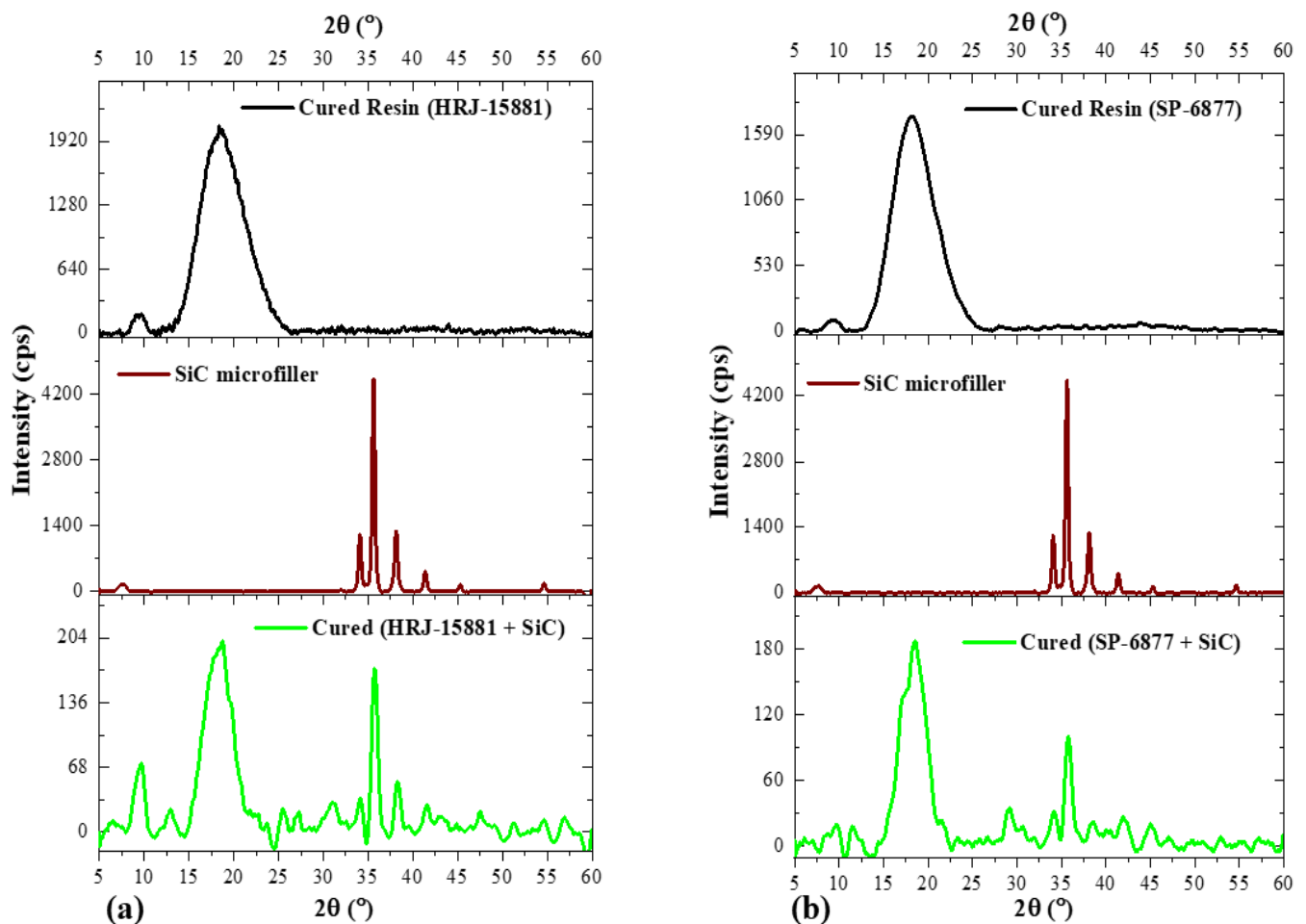


Figure 4.28. XRD diffractograms showing the effect of SiC microfiller addition on the resins: (a) HRJ-15881 and (b) SP-6877 phenolic resin.

A peak at  $2\theta \sim 18.2^\circ$  was obtained for both phenolic resins which contained colloidal silica microfillers. This peak shifted to the left, as compared to the individual cured resin peak which existed at  $2\theta \sim 18.6^\circ$  for SP-6877 resin and  $18.8^\circ$  for HRJ-15881 resin. Furthermore, this peak of

the phenolic resins containing colloidal silica also shifted to the left, when compared with the colloidal silica peak which existed at  $2\theta \sim 22^\circ$ . The shifting of the phenolic resin containing colloidal silica peak may have occurred due to the intercalation of silica into the phenolic resin. Thus, it could be inferred from the XRD diffractogram that colloidal silica microfillers are present and intercalated in the phenolic resin matrix [23], [112].

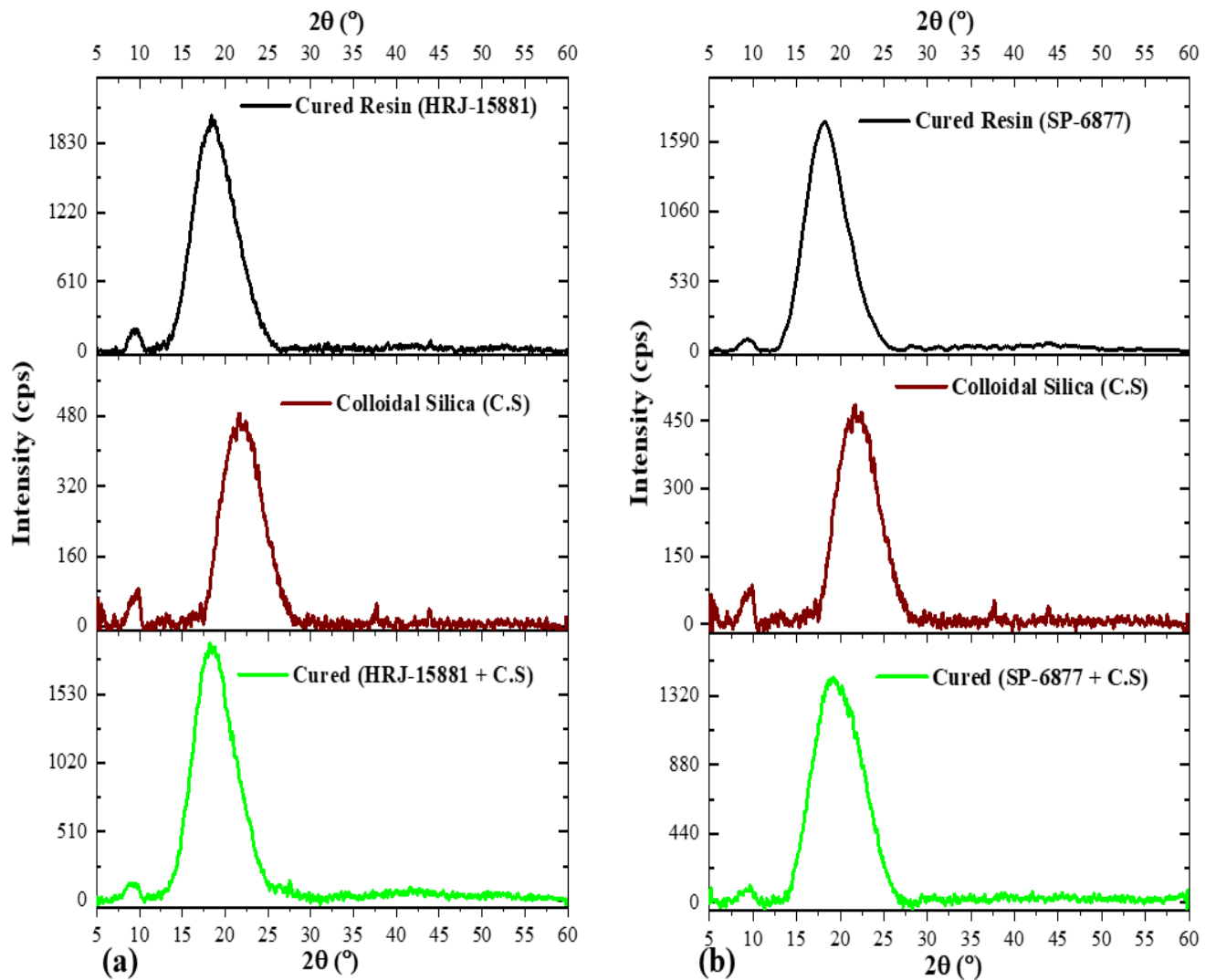


Figure 4.29. XRD diffractograms showing the effect of colloidal silica microfiller addition on the resins: (a) HRJ-15881 and (b) SP-6877 phenolic resin.

In general, from all the XRD diffractograms obtained, it could be inferred that the microfillers are present and intercalated in the phenolic resin matrix.

### 4.7.1 Crystallinity

The internal structure of carbonized materials is characterized by random mixing and interconnections of crystalline carbon nano-clusters and amorphous carbon nano-clusters [113]. The (002) peak strength is the sum of the crystalline and amorphous carbon [114]. As described in the works of Kang *et al.* [113] and Lu *et al.* [114], the relative fractions of these crystalline carbon nano-clusters and the amorphous carbon nano-clusters were calculated using the maximum intensity of the (002) peak. This approach was used to determine the degree of crystallinity of the polymers used in this study, as shown in Fig. 4.30.

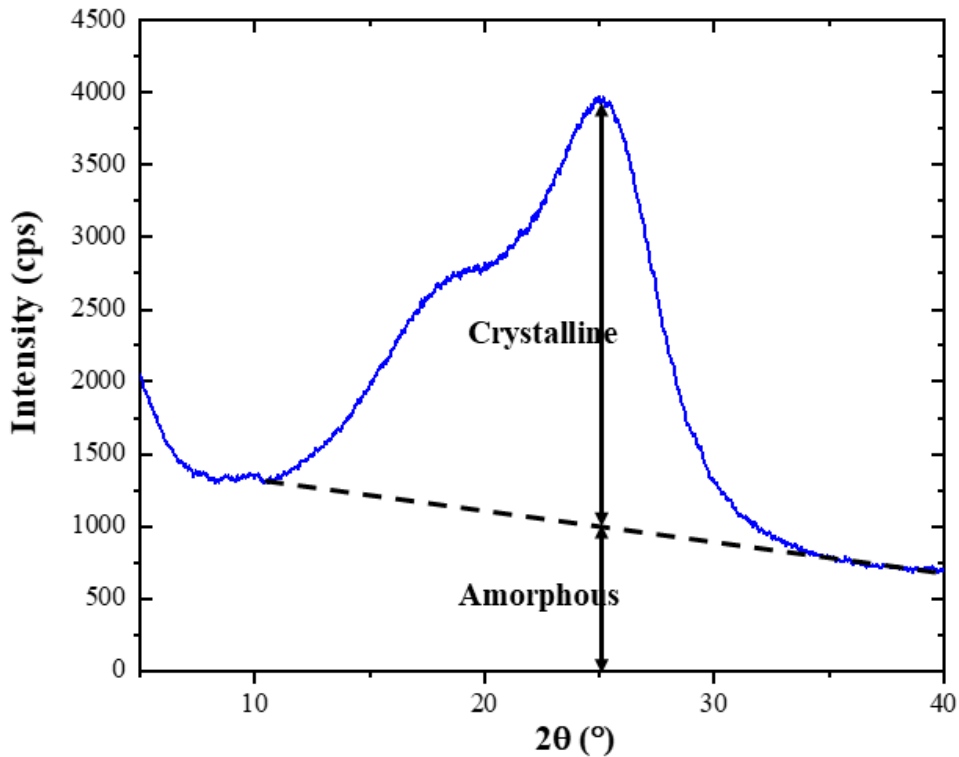


Figure 4.30. Determination of the percentage crystallinity and amorphous from an XRD diffractogram of CFRP made with SP-6877 without microfillers.

The degree of percentage crystallinity was calculated as follows:

$$\text{Crystalline fraction (\%)} = (I_{\text{crystalline}} / I_{\text{total}}) \times 100$$

$$\text{Amorphous fraction (\%)} = (I_{\text{amorphous}} / I_{\text{total}}) \times 100$$

The results of the calculated percentage crystallinity for the carbon fiber, phenolic resins with and without microfillers, and the CFRP with and without microfillers are presented in Table 4.5. The percentage crystallinity of the carbon fiber was determined to be 87.4% and amorphous content of 26.6%. The crystalline fractions of both cured phenolic resin are ~76% and 66% for SP-6877 resin and HRJ-15881 resin, respectively. This indicates that the cured phenolic resin is a highly crystalline polymer with moderate amorphous carbon content and the SP-6877 resin has higher crystallinity than the HRJ-15881 resin. These values are consistent with what Kang *et al.* [113] obtained in their research work, the authors obtained a crystalline fraction of 73% to 72.9% at a heating rate of 1 and 5 °C/min respectively, in relation to the present work that was carried out at a heating rate of 2 °C/min. The addition of carbon fiber to the phenolic resin to form the CFRP composites resulted in a percentage crystallinity value of 64.81% and 67.37% for the CFRP composite made with SP-6877 resin and HRJ-15881 resin respectively. When compared with the cured resin percentage crystallinity value, this translates to a decrease of 11.23% for SP-6877 resin and an increase of 1.44% for HRJ-15881 resin.

When compared with the CFRP without fillers, the addition of colloidal silica microfiller to the CFRP composite decreased the percentage crystallinity for the CFRP made with SP-6877 resin and increased the percentage crystallinity for the CFRP made with HRJ-15881 resin. When colloidal silica was added, the CFRP made with HRJ-15881 resin experienced a 3.5% increase, and the CFRP made with SP-6877 resin had a 3.6% decrease. In comparison to cured neat resin, the addition of colloidal silica to the HRJ-15881 resin increased its percentage crystallinity by 7.5%. On the contrary, the addition of colloidal silica microfillers to the SP-6877 resin decreased its percentage crystallinity by 1.2%.

Table 4.5. Amorphous and crystalline fraction of cured resin and composites.

Materials	SP-6877		HRJ-15881	
	Crystalline fraction ( $I_c$ ) (%)	Amorphous fraction ( $I_c$ ) (%)	Crystalline fraction ( $I_c$ ) (%)	Amorphous fraction ( $I_c$ ) (%)
Cured Resin	76.0	24.0	65.9	34.1
CFRP without microfillers	64.8	35.2	67.4	32.6
CFRP with colloidal silica	61.2	38.8	70.8	29.2
Cured (resin and colloidal silica)	74.9	25.1	73.4	26.6
CFRP with SiC	75.6	24.4	75.3	24.7
Cured (resin and SiC)	77.9	22.1	72.1	27.9

When compared with the CFRP without fillers, the addition of SiC microfiller to the CFRP composites increased the percentage crystallinity for the CFRP made with each of the two phenolic resins. The CFRP made with HRJ-15881 resin experienced a 7.93% increase in percentage crystallinity, while the CFRP made with SP-6877 experienced a 10.79% increase in percentage crystallinity. Similarly, the addition of SiC to both phenolic resin increased the percentage crystallinity for HRJ-15881 resin by 6.17% while that of SP-6877 resin increased by 1.86%. Sekhar *et al.* [23] observed an increase in the crystalline behavior of phenolic as a result of the addition of montmorillonite clay.

In summary, there was an increase in resin's percentage crystallinity when the SiC microfiller was added to either the SP-6877 resin or HRJ-15881 resin. However, only the HRJ-15881 resin experienced an increase in percentage crystallinity when colloidal silica was added. When SiC was added to the carbon fiber reinforced phenolic (CFRP), there was an increase in percentage crystallinity either when the CFRP was made from SP-6877 resin or HRJ-15881 resin. However, when the colloidal silica was added to the CFRP, only the CFRP made with HRJ-15881 resin experienced an increase in percentage crystallinity. In contrast, the CFRP made with SP-6877 resin experienced a decrease in percentage crystallinity. Thus, it could be inferred that the effect of filler addition to cured phenolic resin and carbon fiber reinforced phenolic matrix composite is

dependent on the phenolic resin and the type of microfillers added. To a great extent, the results obtained in the flexural strength, impact strength, and the crystallinity behavior of the CFRP composites are consistent with one another. There was an improvement in percentage crystallinity with SiC addition than with colloidal silica, which was confirmed by the improvement of the flexural and impact strength with SiC addition, as compared with the decrease in the flexural and impact strength with colloidal silica addition. Hence, the flexural and impact behavior of the CFRP composites with microfillers addition might be influenced by the effect of these additions on their percentage crystallinity.

Rahman *et al.* [115] fabricated SiC bulk samples from Allyhydridopolycarbosilane polymer precursor at three different processing temperatures 900 °C, 1150 °C, and 1400 °C respectively. They reported that at higher processing temperatures, the degree of the crystallinity and the Si-C bond content increases, suggesting that amorphous to crystalline conversion occurred at higher processing temperatures. As a result of these, mechanical properties such as elastic modulus and hardness were found to increase with the processing temperatures. Thus, it could be inferred that the improvement in flexural and dynamic impact properties obtained with CFRP composites that contained SiC microfillers, is as a result of the  $\alpha$ -SiC type microfiller used in this study which was formed at a temperature greater than 2500 °C, based on the information obtained about this processing temperature from the manufacturer (Washington Mills).

## **4.8 Fracture Analysis of the CFRP under Mechanical Loading**

### **4.8.1 Three-point flexural loading**

Optical micrographs depicting failure mode in the test specimens under three-point flexural load are presented in Figs. 4.31 and 4.32 for composites without and with SiC microfiller, respectively. Fiber breakage, delamination, matrix, and intra-ply cracking are the observed failure modes in all cases. For the specimens without SiC and those containing lower SiC addition ( $\leq 1$  wt.%), fiber breakage, matrix cracking, and delamination are the observed failure modes. With increasing SiC addition ( $\geq 1.5$  wt.%), the failure became more intense with the appearance of intra-ply cracking (Fig. 4.32). This more intense damage at higher SiC content ( $\geq 1.5$  wt.%) could be attributed to filler agglomeration and poor adhesion between agglomerated fillers and the phenolic matrix. Under the applied flexural load, the agglomeration sites for the SiC microfillers could serve as a

point where cracking or de-bonding occur, thereby interfering with the distribution of the flexural loads between the fiber and the matrix. So, the decrease in flexural properties at higher SiC addition ( $\geq 1.5$  wt.%) obtained in section 4.4 is in good agreement with the observed lower flexural strength at higher SiC addition ( $\geq 1.5$  wt.%).

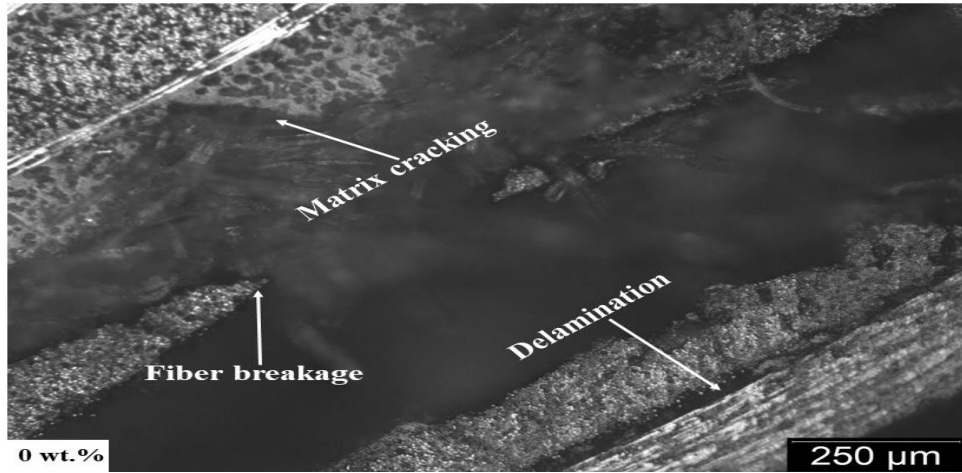


Figure 4.31. Optical micrograph showing damage in a composite test specimen containing no microfiller under three-point flexural loading.

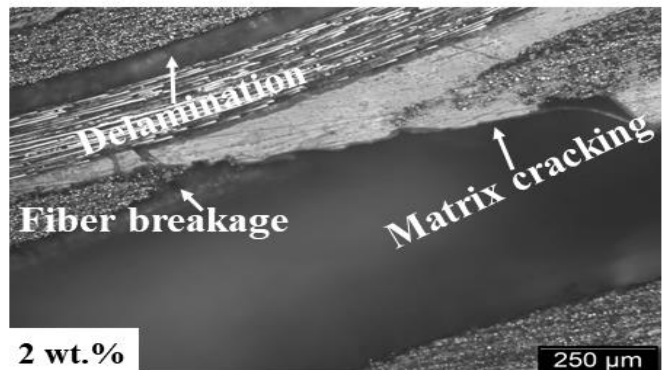
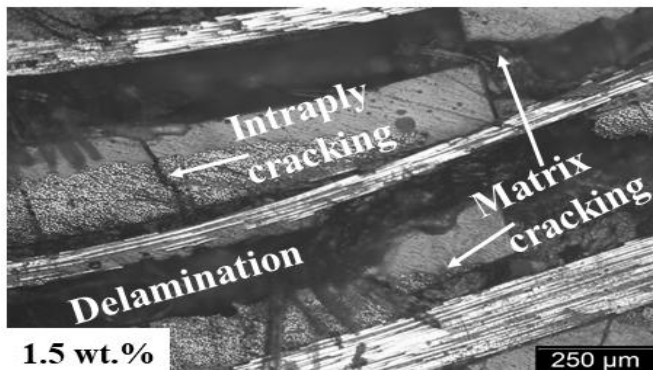
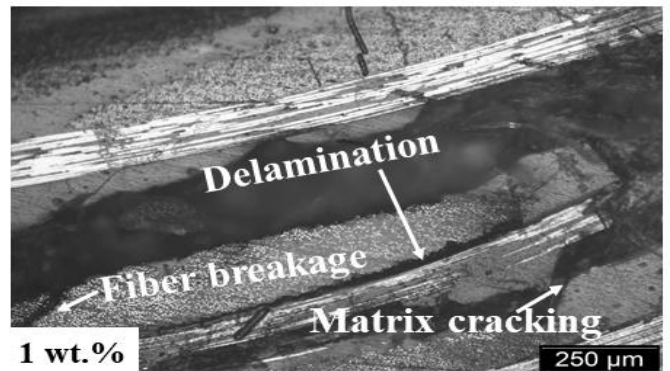
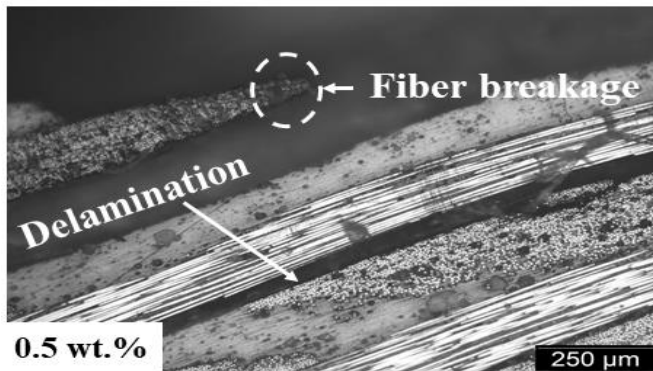


Figure 4.32. Optical micrographs showing damage in flexural test samples with SiC addition.

Two test specimens representing composite containing low (0.5 wt.%) and high (2.0 wt. %) SiC microfiller addition that failed under flexural load were further investigated using SEM. The obtained SEM micrographs showing the intensity of damage in the flexural specimens containing SiC addition are presented in Figs. 4.33 - 4.36. Figs. 4.33 and 4.34 show the SEM micrographs of the fractured CFRP composite containing 0.5 wt.% SiC, while Figs. 4.35 and 4.36 show the SEM micrographs of the fractured CFRP composite containing 2.0 wt.% SiC.

The SEM micrographs of the fractured CFRP specimens containing 0.5 wt.% SiC indicate delamination, fiber breakage, fiber pull-out, and matrix cracking as the predominant failure modes. More detailed microstructures of the fractured specimens at higher magnification are provided in Fig. 4.34. The individual fiber pull out, fiber breakage, delamination, and matrix cracking could be clearly observed. Also, from Fig. 4.34, it could be seen that despite the flexural fracture, the fibers that are pulled out are still well-positioned and secured in the phenolic resin. The SEM micrographs confirm good interfacial adhesion between the fibers and the phenolic resin matrix.

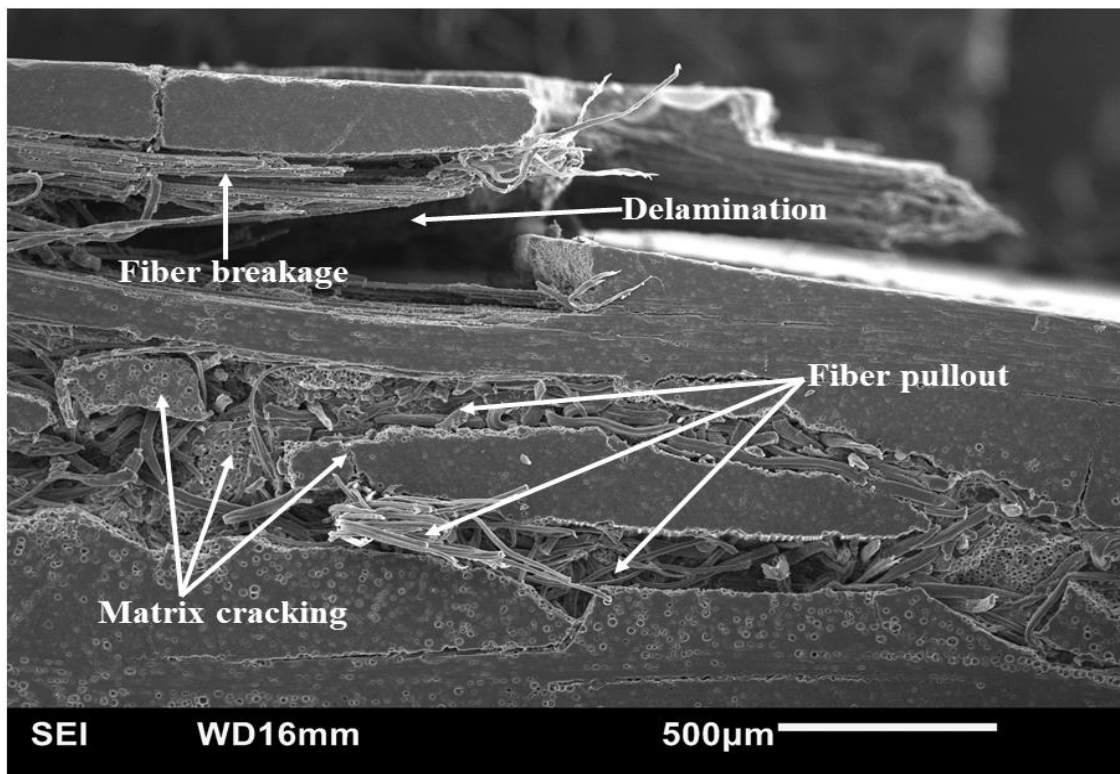


Figure 4.33. SEM micrograph showing damage in flexural test samples containing 0.5 wt.% SiC.

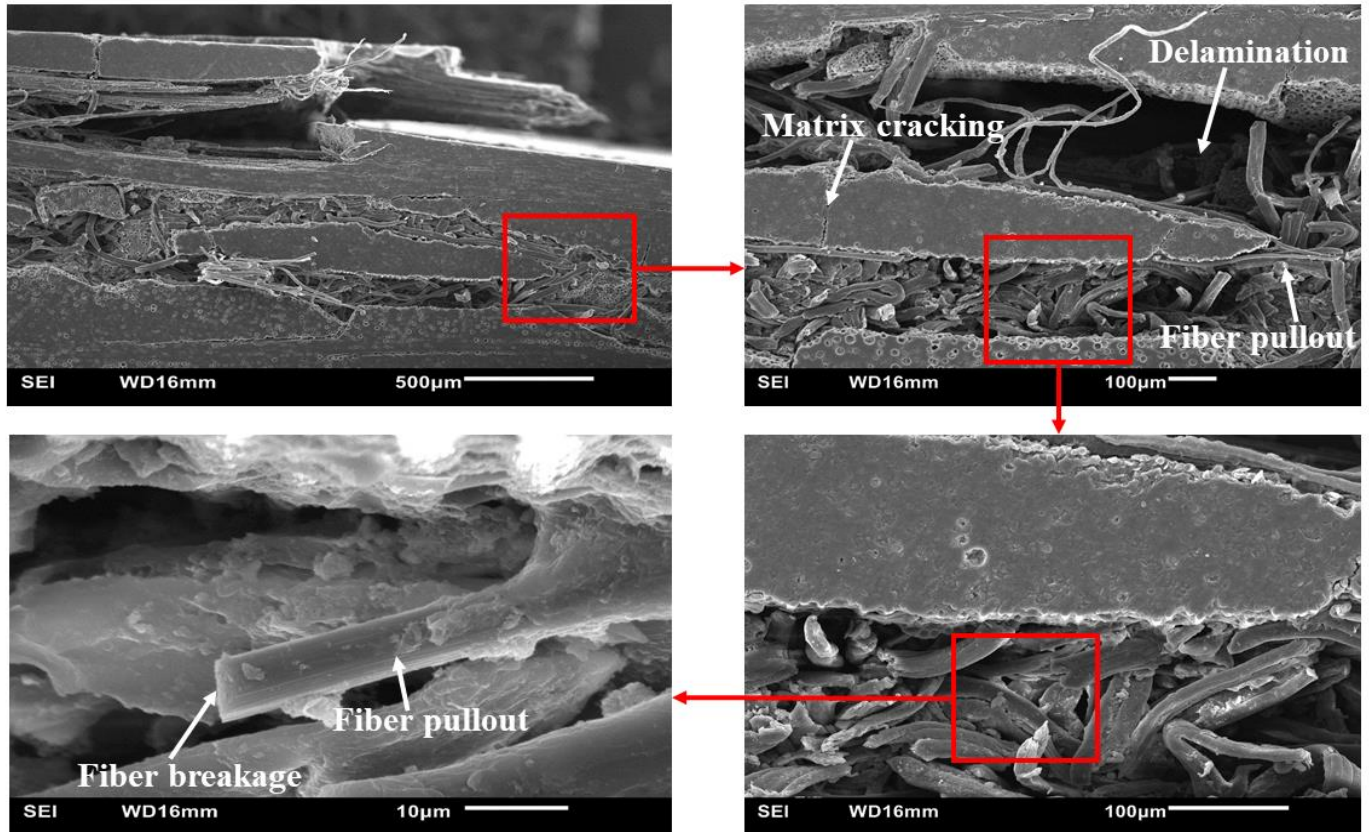


Figure 4.34. SEM micrographs showing detailed damage in flexural test samples containing 0.5 wt.% SiC.

When SiC addition to the CFRP was increased to 2 wt. %, failure became more intense with the fiber breakage, delamination, matrix cracking, and fiber pull out becoming more severe. Also, intra-ply cracking appeared as an additional failure mode (Fig. 4.35). Higher magnification SEM images indicating fiber pull out, fiber breakage, delamination, matrix, and intra-ply cracking are shown in Fig. 4.36. A greater amount of the fiber pull-outs can be observed compared with the CFRP composite containing 0.5 wt.% SiC. Overall, optical and SEM micrograph showed that the failure became more intense in the CFRP composite at higher SiC addition ( $\geq 1.5$  wt.%).

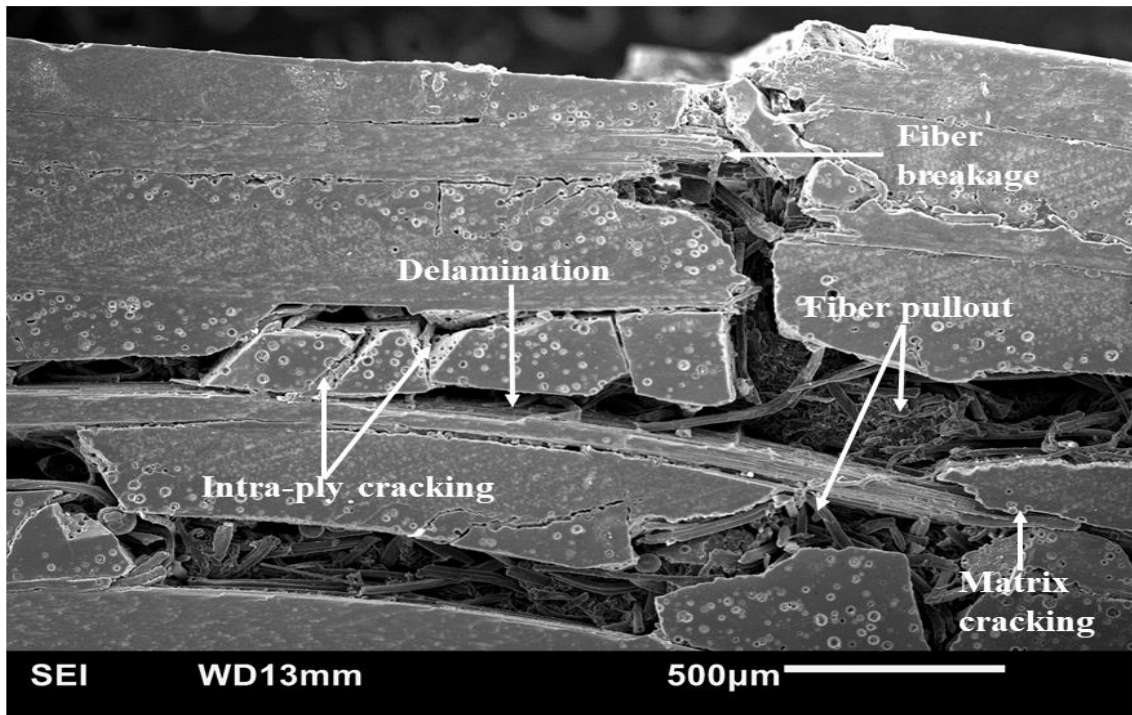


Figure 4.35. SEM micrograph showing damage in flexural test samples containing 2 wt.% SiC.

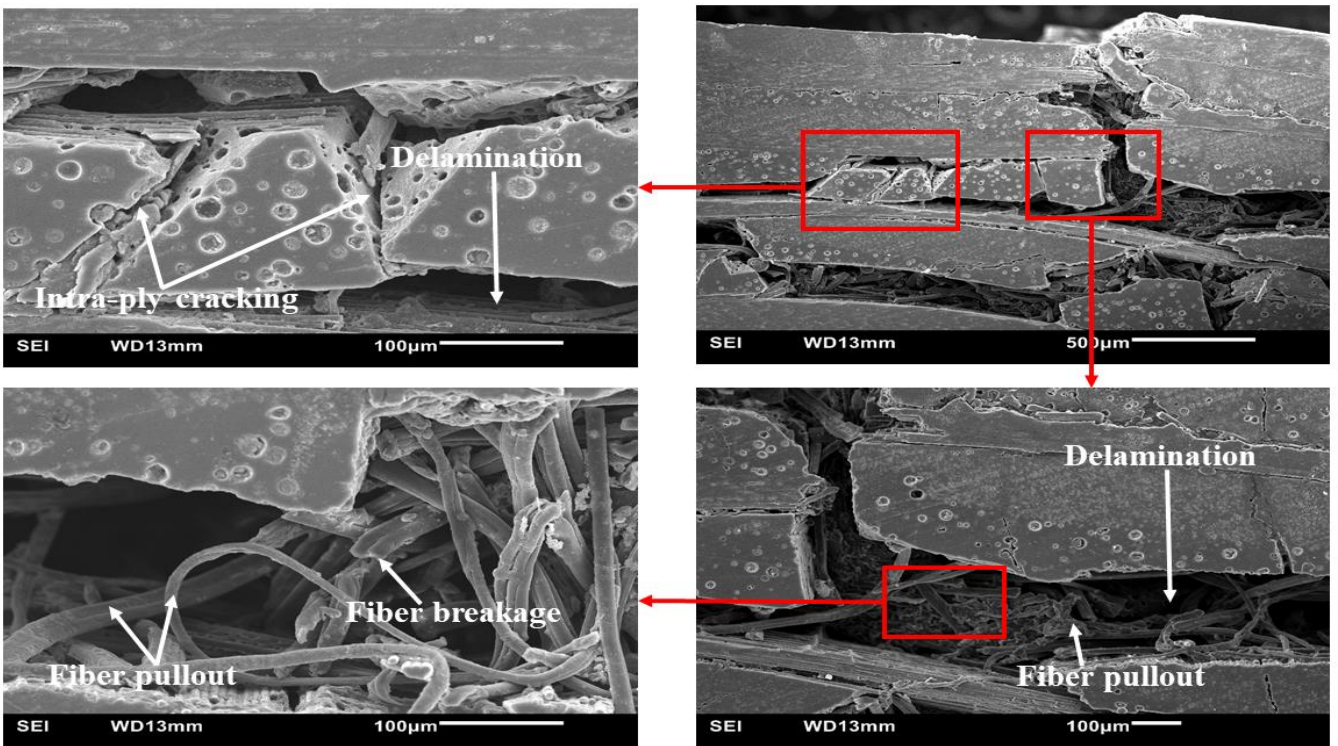


Figure 4.36. SEM micrographs showing detailed damage in flexural test samples containing 2 wt.% SiC.

#### 4.8.2 Dynamic impact loading

Table 4.6 provides an overview of the fractured state of the CFRP specimens after exposure to dynamic impact loads. At impact momentum of 15 kg m/s, no failure was observed in the CFRP for both phenolic resins, with and without microfillers addition. However, at impact momentum of 28 kg m/s and for the CFRP composite made with each phenolic resins containing SiC, failure occurred in composites containing 0.5 and 1.0 wt.% SiC addition. At higher SiC addition ( $\geq 1.5$  wt.%), the dynamic impact sample did not fail and retained its structural integrity. However, with colloidal silica addition to the CFRP composite made with each phenolic resins, no failure was observed up to 1.5 wt.% colloidal silica addition. For composites containing 2 wt.% colloidal silica addition, the dynamic impact sample failed.

Table 4.6. The results of the visual examination of impacted CFRP specimens showing whether fracture occurred or not.

Impact momentum	Filler addition	Specimen Fracture	
		HRJ-15881	SP-6877
15 kg m/s	None	No	No
28 kg m/s		Yes	Yes
15 kg m/s	0.5 wt. % SiC	No	No
	1.0 wt. % SiC	No	No
	1.5 wt. % SiC	No	No
	2.0 wt. % SiC	No	No
28 kg m/s	0.5 wt. % SiC	Yes	Yes
	1.0 wt. % SiC	Yes	Yes
	1.5 wt. % SiC	No	No
	2.0 wt. % SiC	No	No
15 kg m/s	0.5 wt. % colloidal silica	No	No
	1.0 wt. % colloidal silica	No	No
	1.5 wt. % colloidal silica	No	No
	2.0 wt. % colloidal silica	No	No
28 kg m/s	0.5 wt. % colloidal silica	No	No
	1.0 wt. % colloidal silica	No	No
	1.5 wt. % colloidal silica	No	No
	2.0 wt. % colloidal silica	Yes	Yes

Overviews of the fractured specimens under impact momentum of 28 kg m/s, as observed under a stereomicroscope, are presented in Figs. 4.37 - 4.39. Figure 4.37 shows the fracture surface of CFRP specimens containing no filler addition. Fig. 4.38 shows those of CFRP containing 0.5 wt.

% SiC, while Fig. 4.39 shows those of CFRP containing 2.0 wt. % SiC. In all cases, the failure was characterized by the sample splitting into two, with delamination being the major primary failure mode. Furthermore, the fracture surface of all the failed samples had an undulating rough ridged surface suggesting rupture of matrix and fiber bundles under the impact loading. This would be revealed more clearly when examined at higher magnifications under SEM. The rough ridged surface is more pronounced in the CFRP composite containing SiC. The composites containing colloidal silica and those without fillers exhibit similar fracture surface morphology.

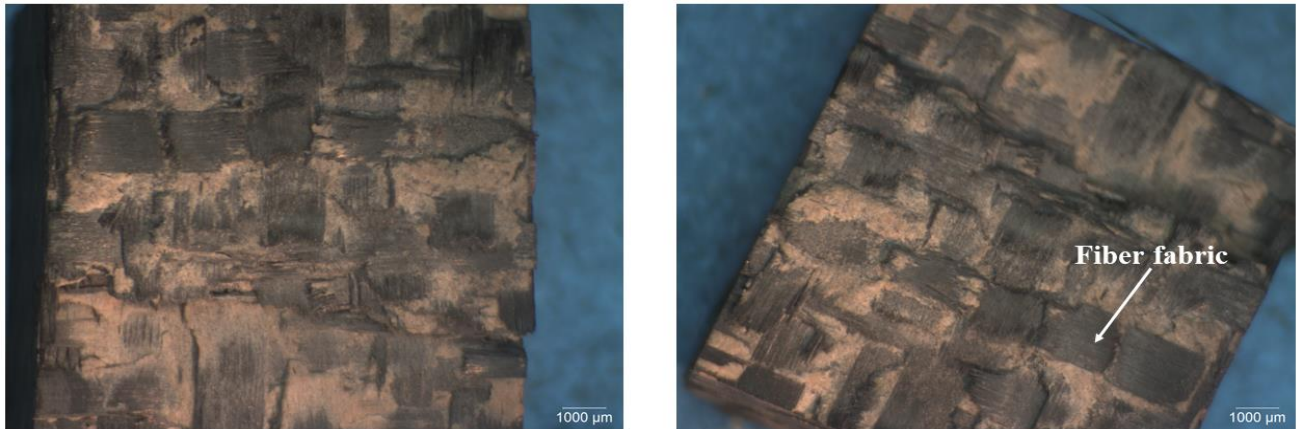


Figure 4.37. Optical macrographs showing impact failure of CFRP without microfillers; impacted at 28 kg m/s.



Figure 4.38. Optical macrograph showing impact failure of CFRP composite containing 0.5 wt.% SiC; impacted at 28 kg m/s.

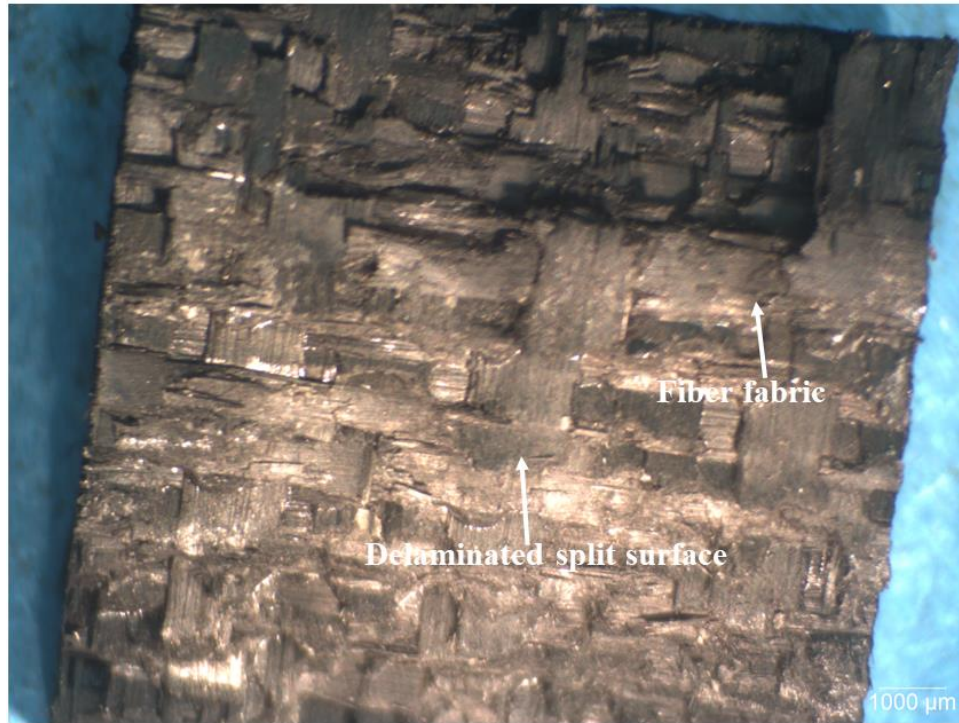


Figure 4.39. Optical macrograph showing impact failure of CFRP composite containing 2 wt.% colloidal silica; impacted at 28 kg m/s.

The SEM micrographs of the fracture of the surface of impacted CFRP composite; without fillers, with 0.5 wt.% SiC addition and 2 wt.% colloidal silica addition (impacted at 28 kg m/s) are presented in Figs. 4.40, 4.41, and 4.42 respectively. For the CFRP without fillers, the primary failure mode was specimen split by delamination. Fiber bundle breakage could also be observed. Furthermore, it could also be inferred from the SEM micrograph that despite fiber bundle breakage and delamination, the phenolic resin impregnated the fiber preform excellently, and there is evidence of good interfacial adhesion between the fiber and the matrix. This good interfacial adhesion might be the reason why the fiber is still packed in bundles despite rupture under the dynamic impact load.

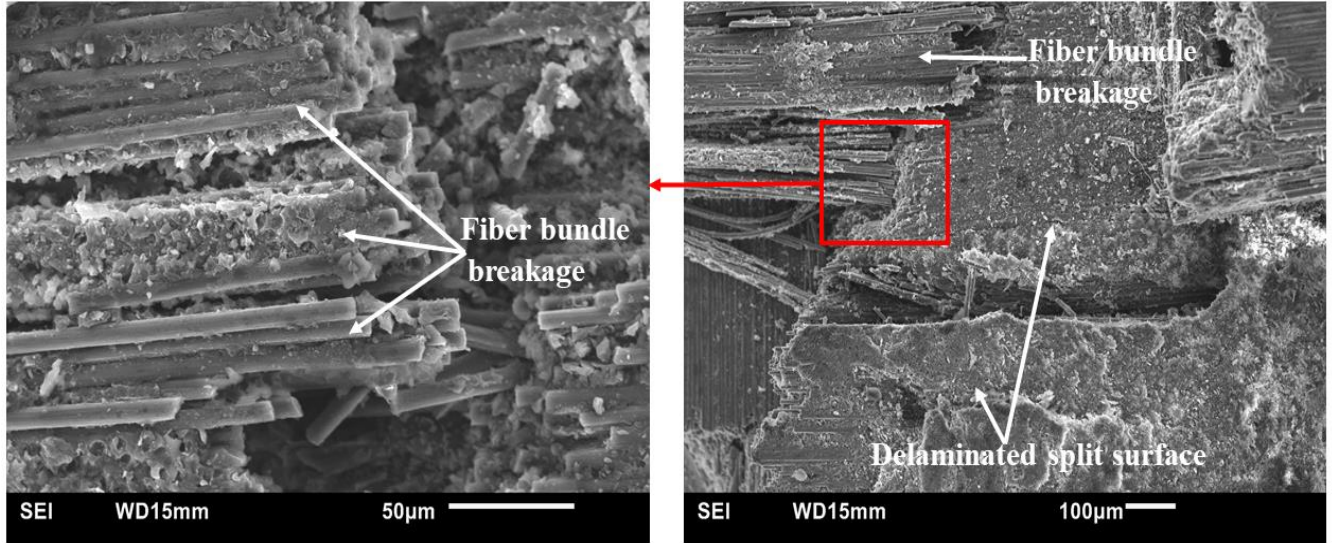


Figure 4.40. SEM fractographs obtained for CFRP without fillers after fracture under impact loading (28 kg m/s).

For the CFRP composite containing 0.5 wt.% SiC, the failure mode is also characterized by delamination and fiber bundle breakage. However, more fiber bundle breakage is observed when compared with the CFRP composite without fillers. Perhaps, the more fiber bundle breakage might be the reason for the undulating jagged ridged surface observed in the optical macrograph of the fracture surface. The SEM micrograph also indicates a good interfacial adhesion between the fiber and the phenolic resin matrix.

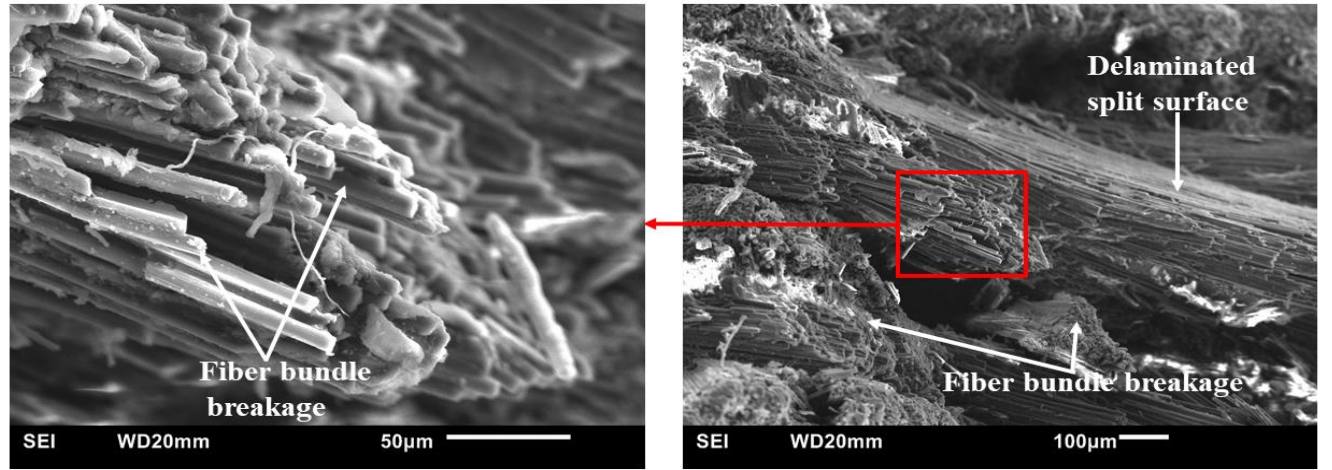


Figure 4.41. SEM fractographs obtained for CFRP composite containing 0.5 wt.% SiC after fracture under impact loading (28 kg m/s).

For the CFRP composite containing 2 wt.% colloidal silica, the failure mode is also characterized by delamination and fiber bundle breakage. However, a crack, which is an additional failure feature, is also observed. The crack, propagating perpendicular to the delaminated (fracture) surface, is shown in Fig. 4.42. It can be observed that the fracture surface was not as jagged, probably due to less fiber bundle breakage as compared with the CFRP composite containing 0.5 wt.% SiC. Also, the SEM micrographs indicate good interfacial adhesion between the fiber and the matrix and excellent resin impregnation of carbon fiber preform with the phenolic resins.

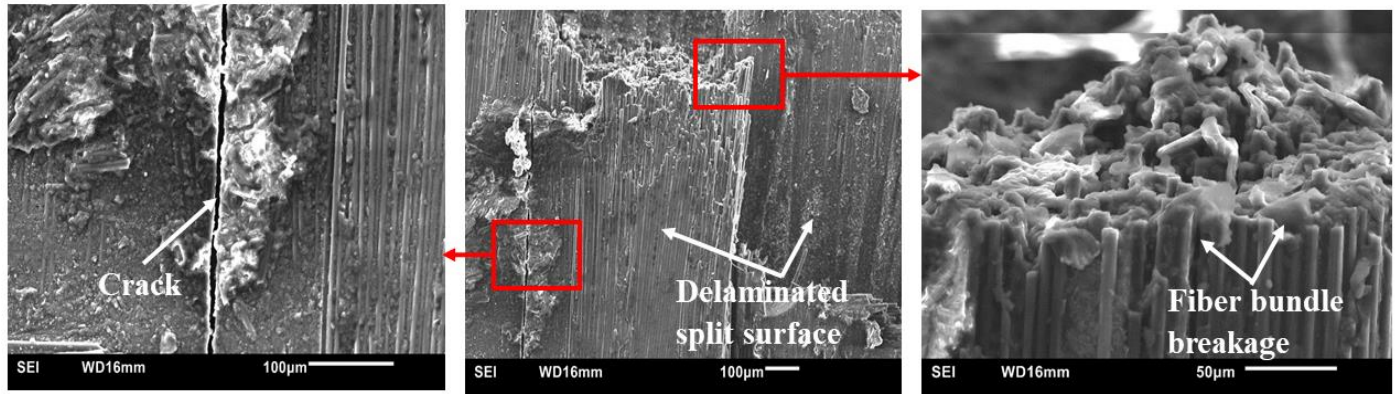


Figure 4.42. SEM fractographs obtained for CFRP composite containing 2 wt.% colloidal silica after fracture under impact loading (28 kg m/s).

## CHAPTER 5

### SUMMARY, CONCLUSIONS AND RECOMMENDATIONS

#### 5.1 Summary

In this MSc research study, carbon fiber reinforced phenolic matrix composite was developed using two variations of phenolic resins (SP-6877 and HRJ-15881) supplied by SI Group. The two resins have the same phenol and solid content but differ mainly in their viscosity and formaldehyde (HCHO) content. A 3K, 2x2 twill-weave carbon fiber fabric produced by Fibre Glast Developments Corporation was used as reinforcement for these resins. The phenolic resins were characterized using Thermogravimetric analysis (TGA), Fourier Transform Infrared Spectroscopy analysis (FTIR) and X-ray Diffraction (XRD). Layers of the carbon fiber fabric placed in a mold cavity were infiltrated with phenolic resin followed by curing in an autoclave at 120 °C under pressure (50 bar) in an argon atmosphere. Microstructural examination of the composite using both optical and scanning electron microscopes revealed good wetting and impregnation of the fiber with the phenolic resins. An excellent interfacial adhesion between the fiber and the phenolic matrix was observed. The mechanical properties of the composite were characterized using 3-point flexural test and dynamic impact test. The three-point flexural test was carried out using an Instron™ universal testing machine (Model 5500R) while the dynamic impact test was carried out using a Split Hopkinson pressure bar system (SHPB).

To investigate the effects of microfiller additions on the mechanical properties of the carbon fiber reinforced phenolic, 0.5, 1, 1.5, and 2 wt.% of SiC or colloidal silica were added to the phenolic resin before infiltration into the carbon fiber preforms. The results of the X-ray diffraction (XRD) analyses on composites containing microfillers produced suggest intercalation of the microfillers when added to the phenolic resins. The microstructures and mechanical properties of the carbon fiber reinforced phenolic matrix composites containing fillers are compared with those containing no fillers. The damage evolution in the composites during 3-point flexural and impact loading was investigated using a scanning electron microscope. The effect of the microfiller on the flexural behavior and impact resistance of carbon fiber reinforced phenolic matrix composites depend on the applied resin, the kind, and content of microfiller in the phenolic matrix. Despite intense effort to disperse the filler in the phenolic resins using both magnetic stirrer and ultrasonication, filler

agglomeration occurred at high filler contents. This impaired the mechanical behavior of the composites containing more than 1.0 % microfiller content.

## 5.2 Conclusions

Based on experimental results, the following conclusions drawn from this MSc research study:

1. Thermogravimetric analysis (TGA) indicates two prominent DTG peaks as the liquid resins were heated from room temperature to 1000 °C. They represent the peaks for cross-linking reactions and decomposition of cross-linked phenolic to amorphous carbon. A slight difference is observed in peaks' temperature, which may be due to the difference in the resins' solvent contents. The cross-linking reaction occurs for both phenolic resins in the temperature range 110-130 °C, and decomposition of the phenolic to form amorphous carbon begins around 450 °C. TG analysis of previously cured phenolic from the two resins indicates the same thermal behavior, i.e., it is not affected by the difference in the viscosity and formaldehyde content of the resins.
2. Without reinforcement with carbon fiber or microfillers, the flexural strength and flexural modulus of cured resin HRJ-15881, with higher viscosity and lower formaldehyde content, is higher than those of cured SP-S6877 resin.
3. The reinforcement of both phenolic resin with carbon fibers increased the flexural strength and flexural modulus of the cured resins by over 500%. Without microfillers addition, the CFRP made with SP-6877 resin (with lower viscosity and higher formaldehyde content) had better flexural strength and modulus than those made with HRJ-15881 resin with higher viscosity and lower formaldehyde content. This suggests that the resin with the lower viscosity and higher formaldehyde content produce CFRP with better resistance to flexural load.
4. With microfillers addition, the flexural strength of the CFRP increased with SiC addition up-to 1 wt.% SiC to the phenolic resin. On the contrary, flexural modulus did not increase. The flexural properties deteriorated with colloidal silica addition owing to its agglomeration as compared to the SiC microfiller.
5. The failure modes of the CFRP under 3-point flexural loading include fiber breakage, delamination, fiber pull-out, and matrix cracking in the CFRP without microfiller and at lower microfiller addition ( $\leq 1$  wt.%). However, the failure modes became more intense at

higher micro-filler addition ( $\geq 1.5$  wt.%) with the occurrence of extensive intra-ply (matrix) cracking.

6. Without microfillers, the CFRP made with HRJ-15881 resin (higher viscosity and lower formaldehyde content) exhibit a slightly higher impact strength than that made with SP-6877 resin at the two impact momenta (15 kg m/s and 28 kg m/s) applied in this study. With microfiller addition, and at impact momentum of 15 kg m/s, the dynamic impact strength of the CFRP composites made with HRJ-15881 resin increased with SiC addition up to 1.5 wt.% and while that of CFRP made with SP-6877 resin only increase by the addition of 0.5 wt.% SiC. However, the dynamic impact strength deteriorated with colloidal silica addition and for both of the phenolic resins.
7. At a more severe impact momentum of 28 kg m/s, impact strength of the CFRP increased at all SiC addition for the SP-6877 resin and only up to 0.5 wt.% for the HRJ-15881 resin. Similarly, the dynamic impact strength deteriorated with colloidal silica addition and for both of the phenolic resins.
8. At impact momentum of 15 kg m/s, CFRP with and without microfillers did not fracture for both applied phenolic resins.
9. At impact momentum of 28 kg m/s, the CFRP without fillers for both phenolic resin failed depending on the filler content. With SiC microfiller addition and for both of the phenolic resins, the CFRP fractured at lower SiC addition ( $\leq 1$  wt.%) and resisted fracture at higher SiC addition ( $\geq 1.5$  wt.%). With colloidal silica addition and for both phenolic resins, the CFRP resisted failure up to  $\leq 1.5$  wt.% colloidal silica addition and failed at 2 wt.%.
10. The carbon fiber reinforced CFRP, with or without microfiller, fractured under dynamic impact loading by fiber bundle rupture, matrix cracking, and delamination.
11. The percentage crystallinity of the phenolic increased when SiC microfiller was added to either the SP-6877 resin or HRJ-15881 resin. However, only the HRJ-15881 resin experienced an increase in percentage crystallinity when colloidal silica was added. When SiC was added to the carbon fiber reinforced phenolic (CFRP), there was an increase in percentage crystallinity either when the CFRP was made from SP-6877 resin or HRJ-15881 resin. However, when the colloidal silica was added to the CFRP, only the CFRP made with HRJ-15881 resin experienced an increase in percentage crystallinity. In contrast, the CFRP made with SP-6877 resin experienced a decrease in percentage crystallinity.

12. The effect of the addition of SiC and colloidal silica microparticles to phenolic resins on the flexural and impact behaviors of the CFRP produced from these resins is determined by, the type and the content of microparticle addition, viscosity, and formaldehyde content of the applied resins.

### **5.3 Recommendations for Future Work**

1. With the promising improvement in mechanical properties of carbon fiber reinforced phenolic offered by the SiC microfiller addition in this study, the possibilities of improvements in the flexural and impact properties of C/C composites, produced by pyrolysis of carbon fiber reinforced phenolic, with the addition of the SiC microfillers should be investigated. This shows the promise of leading to the development of improved and tough C/C composites that could resist dynamic impact failure in aerospace and other structural applications.
2. With the improvement in mechanical properties offered by the SiC microfillers, it would be interesting to try nanofillers (e.g., CNTs or nanoSiC) and investigate the possibilities of improvement in mechanical properties of the carbon fiber reinforced phenolic composites and C/C composites under these loading conditions. Carbon fiber reinforced phenolic matrix composites containing addition of these two nanofillers were produced shortly before the start of the pandemics and needed to be tested by future researchers in our group.
3. Since SiC and colloidal silica particles are so versatile as semiconductors and/or have excellent wear resistance, further investigations assessing the effects of their use as fillers on electrical properties and wear resistance of the carbon fiber reinforced phenolic matrix composites is recommended. This could usher in the development of new multifaceted materials that could be applicable in electronics and in other areas where exposure to abrasion is inevitable.
4. As surfactant helps lower the surface energy of fillers, facilitate their separation to prevent agglomeration, and enhance their dispersion during mixing with phenolic resins, it would be interesting to try the use of surfactant to aid in the dispersion of the fillers. This could further help in possibilities of improvement in properties.

## REFERENCES

- [1] P. Morgan, *Carbon Fibers and Their Composites*. Boca Raton Florida: Taylor & Francis Group, 2005.
- [2] R. M. Jones, *Mechanics of Composite Materials*, 2nd ed. Blacksburg, Virginia: Taylor & Francis, 1999.
- [3] A. Bhatnagar, *Lightweight ballistic composites, Military and law enforcement applications*. Cambridge England: Woodhead Publishing Limited, 2006.
- [4] L. Pilato, Phenolic resins: 100 Years and still going strong, *React. Functional Polym.*, vol. 73, pp. 270–277, 2012.
- [5] J. D. Buckley and D. D. Edie, *Carbon-Carbon Materials and Composites*. Park Ridge, New Jersey, U.S.A: Noyes Publications, 1993.
- [6] D. D. L. Chung, *Carbon Fiber Composites*. Newton, MA, USA: Butterworth-Heinemann, 1994.
- [7] P. R. Young, HPLC characterization of phenol-formaldehyde resole resin used in fabrication of shuttle booster nozzles, Final Report for NASA Grant NAG-1-1943, Emory, Virginia, 1999.
- [8] R. Atif and F. Inam, Reasons and remedies for the agglomeration of multilayered graphene and carbon nanotubes in polymers, *Beilstein J. Nanotechnol.*, vol. 7, pp. 1174–1196, 2016.
- [9] D. Bansal, S. Pillay, and U. Vaidya, Nanographene Reinforced Carbon-Carbon Composites, *Carbon N. Y.*, vol. 55, pp. 233–244, 2013.
- [10] A. Kaushik, P. Singh, G. Verma, and Rekhar, Morphology, X-ray Diffraction and Mechanical Properties of Resol-montmorillonite Clay Composites, *J. Thermoplast. Compos. Mater.*, vol. 23, January 2010, pp. 79–97, 2010.
- [11] Y. Ma, Y. Yang, C. Lu, X. Wen, X. Liu, and S. Wu, Enhanced thermal resistance of carbon/phenolic composites by addition of novel nano-g-C<sub>3</sub>N<sub>4</sub>, *Compos. Sci. Technol.*, vol. 180, December 2018, pp. 60–70, 2019.
- [12] C. Ma, Z. Ma, L. Gao, Y. Liu, J. Wang, M. Song, F. Wang, and H. Ishida, Laser ablation

- behavior of nano-copper particle-filled phenolic matrix nanocomposite coating, *Compos. Part B*, pp. 62–68, 2018.
- [13] J. Ding, T. Yang, Z. Huang, Y. Qin, and Y. Wang, Thermal stability and ablation resistance, and ablation mechanism of carbon-phenolic composites with different zirconium silicide particle loadings, *Compos. Part B*, vol. 154, pp. 313–320, 2018.
- [14] M. Ç. Tüzemen, E. Salamcı, and A. Avcı, Enhancing mechanical properties of bolted carbon/epoxy nanocomposites with carbon nanotube, nanoclay, and hybrid loading, *Compos. Part B Eng.*, vol. 128, pp. 146–154, 2017.
- [15] J. Ding, J. Sun, Z. Huang, and Y. Wang, Improved high-temperature mechanical property of carbon-phenolic composites by introducing titanium diboride particles, *Compos. Part B Eng.*, vol. 157, August 2018, pp. 289–294, 2019.
- [16] L. Duan, X. Zhao, and Y. Wang, Oxidation and ablation behaviors of carbon fiber/phenolic resin composites modified with borosilicate glass and polycarbosilane interface, *J. Alloys Compd.*, vol. 827, p. 154277, 2020.
- [17] Y. Ma, Y. Yang, C. Lu, X. Wen, X. Liu, K. Lu, S. Wu, and Q. Liu, Extraordinary improvement of ablation resistance of carbon/phenolic composites reinforced with low loading of graphene oxide, *Compos. Sci. Technol.*, vol. 167, pp. 53–61, 2018.
- [18] I. Srikanth, N. Padmavathi, S. Kumar, P. Ghosal, A. Kumar, and C. Subrahmanyam, Mechanical, thermal and ablative properties of zirconia, CNT modified carbon/phenolic composites, *Compos. Sci. Technol.*, vol. 80, pp. 1–7, 2013.
- [19] A. Naderi, S. Mazinani, S. Javad Ahmadi, M. Sohrabian, and R. Arasteh, Modified thermo-physical properties of phenolic resin/carbon fiber composite with nano zirconium dioxide, *J. Therm. Anal. Calorim.*, vol. 117, no. 1, pp. 393–401, 2014.
- [20] H. J. Song, Z. Z. Zhang, and Z. Z. Luo, A study of tribological behaviors of the phenolic composite coating reinforced with carbon fibers, *Mater. Sci. Eng. A*, vol. 445–446, pp. 593–599, 2007.
- [21] H. J. Song and Z. Z. Zhang, Study on the tribological behaviors of the phenolic composite coating filled with modified nano-TiO<sub>2</sub>, *Tribol. Int.*, vol. 41, no. 5, pp. 396–403, 2008.

- [22] G. Pelin, C. E. Pelin, A. Stefan, I. Dinca, A. Fikai, E. Andronescu, and R. Trusca, Influence of nanometric silicon carbide on phenolic resin composites properties, *Bull. Mater. Sci.*, vol. 39, no. 3, pp. 769–775, 2016.
- [23] N. C. Sekhar and L. A. Varghese, Mechanical, thermal, and rheological studies of phenolic resin modified with intercalated graphite prepared via liquid phase intercalation, *Polym. Test.*, vol. 79, July, 2019.
- [24] R. Hemanth, M. Sekar, and B. Suresha, Effects of Fibers and Fillers on Mechanical Properties of Thermoplastic Composites, *Indian J. Adv. Chem. Sci.*, vol. 2, pp. 28–35, 2014.
- [25] D. M. Marquis, É. Guillaume, and C. Chivas-joly, Properties of Nanofillers in Polymer, in *Nanocomposites and Polymers with Analytical Methods*, John Cuppoletti, Ed. InTech, p. 261, 2011.
- [26] I. Ozsoy, A. Demirkol, A. Mimaroglu, H. Unal, and Z. Demir, The influence of micro- And nano-filler content on the mechanical properties of epoxy composites, *Stroj. Vestnik/Journal Mech. Eng.*, vol. 61, no. 10, pp. 601–609, 2015.
- [27] G. L. Harris, Properties of Silicon Carbide. Washington DC, USA: INSPEC, the Institution of Electrical Engineers, London, United Kingdom, 1995.
- [28] B. E. Horacio and R. O. William, Colloidal Silica, Fundamental and applications. Delaware USA: Taylor & Francis, 2006.
- [29] R. Taylor, Fibre Composite Aircraft- Capability and Safety, Aviation Research and Analysis Report - AR-2007-021, Canberra City, Australian Capital Territory, Australia, 2008.
- [30] C. He, Y. Li, Z. Zhang, and Z. Sun, Impact damage modes and residual flexural properties of composites beam, *J. Reinf. Plast. Compos.*, vol. 27, no. 11, pp. 1163–1175, 2008.
- [31] G. A. O. Davies and X. Zhang, Impact damage prediction in carbon composite structures, *Int. J. Impact Eng.*, vol. 16, no. 1, pp. 149–170, 1995.
- [32] N. Z. Borba, J. Körbelin, B. Fiedler, J. F. dos Santos, and S. T. Amancio-Filho, Low-velocity impact response of friction riveted joints for aircraft application, *Mater. Des.*, vol.

186, 2020.

- [33] NASA Investigation Accident Board, Columbia Accident Investigation Report, Report-Volume I, Washington DC, USA, 2003.
- [34] A. K. Kaw, *Mechanics of Composite Materials*, 2nd ed. Boca Raton Florida: Taylor & Francis Group, 2006.
- [35] F. C. Campbell, *Manufacturing Processes for Advanced Composites*. Oxford, UK: Elsevier Advanced Technology, 2004.
- [36] I. M. Daniel and O. Ishai, *Engineering Mechanics of Composite Materials*. New York, USA: Oxford University Press Inc., 1994.
- [37] S. G. Advani and E. M. Sozer, *Process modeling in composites manufacturing*. New York, USA: Marcel Dekker Inc, 2003.
- [38] U.S Congress Office of Technology Assessment, *Advanced Materials by Design*, OTA- E-351, Washington DC, USA, Government Printing Office, 1988.
- [39] D. Chandramohan and A. J. Presin Kumar, Experimental data on the properties of natural fiber particle reinforced polymer composite material, *Data Br.*, vol. 13, pp. 460–468, 2017.
- [40] R. K. Roeder, M. M. Sproul, C. H. Turner, Hydroxyapatite whiskers provide improved mechanical properties in reinforced polymer composites, *J. Biomed. Mater. Res. - Part A*, vol. 67, no. 3, pp. 801–812, 2003.
- [41] P. K. Mallick, *Fiber-Reinforced Composites: Materials, Manufacturing, and Design*, 3rd ed. Boca Raton Florida: Taylor & Francis Group, 2007.
- [42] T. Windhorst and G. Blount, Carbon-Carbon composites: A summary of recent developments and applications, *Mater. Des.*, Vol. 18, no. 1, pp. 11-15, 1997.
- [43] K. Akato, Pretreatment and pyrolysis of rayon-based precursor for carbon fibers, Master's Thesis, University of Tennessee, Tennessee, USA, 2012.
- [44] NASA, *Silicon Carbide (SiC) Fiber- Reinforced SiC Matrix Composites*, Cleveland, Ohio, USA, 2017.

- [45] L. Pilato, *Phenolic Resins: A Century of Progress*. Bound Brook, New Jersey, USA, Springer, 2010.
- [46] B. Wielage, A. G. Odeshi, and H. Mucha, Ab Initio Investigation of Carbon Fibre Reinforced Plastics Applying Phenolic Resins, in *Proceedings of the 12th International Conference on Composite Materials, Paris, France, 5–9 July, 1999*, p. 1259.
- [47] W. J. Cantwell and J. Morton, Comparison of the low and high velocity impact response of cfrp, *Composites*, vol. 20, no. 6, pp. 545–551, 1989.
- [48] W. J. Cantwell and J. Morton, The impact resistance of composite materials - a review, *Composites*, vol. 22, no. 5, pp. 347–362, 1991.
- [49] S. X. Wang, L. Z. Wu, and L. Ma, Low-velocity impact and residual tensile strength analysis to carbon fiber composite laminates, *Mater. Des.*, vol. 31, no. 1, pp. 118–125, 2010.
- [50] R. K. Luo, E. R. Green, and C. J. Morrison, Impact damage analysis of composite plates, *Int. J. Impact Eng.*, vol. 22, no. 4, pp. 435–447, 1999.
- [51] R. Kayya, Numerical Modelling of Impact Damage on Carbon Fiber Reinforced Polymer Laminates, Master's Thesis, Ryerson University, Ontario, Canada, 2012.
- [52] A. Faggiani and B. G. Falzon, Predicting low-velocity impact damage on a stiffened composite panel, *Compos. Part A Appl. Sci. Manuf.*, vol. 41, no. 6, pp. 737–749, 2010.
- [53] G. A. Schoeppner and S. Abrate, Delamination threshold loads for low velocity impact on composite laminates, *Compos. Part A Appl. Sci. Manuf.*, vol. 31, no. 9, pp. 903–915, 2000.
- [54] F. E. Knock and John F. Glenn, Dental Material and Method. United States Patent Office, Serial No. 770,756, Delaware USA, p. 10, 1951.
- [55] American Composites Manufacturers Association, Additives & Fillers - Composite Materials|Composites Lab, *CompositeLab*, 2016. Available online: <http://compositeslab.com/composite-materials/additives-fillers/> (accessed Jun. 18, 2020).
- [56] Jan W V van Dijken, Conventional, Microfilled and Hybrid Composite Resins: Laboratory and Clinical Evaluations, UMEA University Odontological dissertations, University of Umea, Umea, Sweden, 1987.

- [57] V. Mittal, *Polymer Nanotube Nanocomposites Synthesis, Properties and Applications*. New Jersey, USA: John Wiley & Sons, 2010.
- [58] B. T. Marouf, Y. W. Mai, R. Bagheri, and R. A. Pearson, Toughening of epoxy nanocomposites: Nano and hybrid effects, *Polym. Rev.*, vol. 56, no. 1, pp. 70–112, 2016.
- [59] I. Khan, K. Saeed, and I. Khan, Nanoparticles: Properties, applications and toxicities, *Arab. J. Chem.*, vol. 12, no. 7, pp. 908–931, 2019.
- [60] V. T. Rathod, J. S. Kumar, and A. Jain, Polymer and ceramic nanocomposites for aerospace applications, *Appl. Nanosci.*, vol. 7, no. 8, pp. 519–548, 2017.
- [61] S. Vorozhtsov, I. Zhukov, A. Vorozhtsov, A. Zhukov, D. Eskin, and A. Kvetinskaya, Synthesis of micro-and nanoparticles of metal oxides and their application for reinforcement of Al-based alloys, *Adv. Mater. Sci. Eng.*, vol. 2015, 2015.
- [62] S. Bhaviripudi, E. Mile, S. A. Steiner III, A. T. Zare, M. S. Dresselhaus, A. M. Belcher, and J. Kong, CVD synthesis of single-walled carbon nanotubes from gold nanoparticle catalysts, *J. Am. Chem. Soc.*, vol. 129, no. 6, pp. 1516–1517, 2007.
- [63] A. M. Ealias and M. P. Saravanakumar, A review on the classification, characterisation, synthesis of nanoparticles and their application, *IOP Conf. Ser. Mater. Sci. Eng.*, vol. 263, no. 3, p. 032019, 2017.
- [64] Yury Gogotsi, *Carbon Nanomaterials*. Boca Raton Florida: Taylor & Francis Group, 2006.
- [65] A. Oberlin and M. Endo, Filamentous growth of carbon through benzene decomposition, *J. Cryst. Growth*, vol. 32, pp. 335–349, 1976.
- [66] M. Endo, S. Iijima, and M. S. Dresselhaus, *Carbon Nanotubes*, 1st ed. Exeter Great Britain: BPC Wheatons Ltd., 1996.
- [67] Sumio Iijima, Helical microtubules of graphitic carbon, *Nature*, vol. 354, 1991.
- [68] A. D. de Oliveira and C. A. Gonçalves Beatrice, Polymer Nanocomposites with Different types of Nanofiller, in *Nanocomposites, Recent Evolution*, S. Sivasankaran, Ed. London United Kingdom: Intechopen, 2019, p. 27.
- [69] S. G. Advani, *Processing and properties of nanocomposites*. Toh Tuck Link, Singapore:

World Scientific Publishing Co. Pte. Ltd., 2007.

- [70] P. L. De Andres, R. Ramírez, and J. A. Vergés, Strong covalent bonding between two graphene layers, *Phys. Rev. B - Condens. Matter Mater. Phys.*, vol. 77, no. 4, pp. 1–11, 2008.
- [71] SWOT Revision, “Intermolecular forces and chemical structures,” *Intermolecular forces and chemical structures*. Available Online:  
[http://www.swotrevision.com/pages/a%20level/chemistry/m1\\_part7.htm](http://www.swotrevision.com/pages/a%20level/chemistry/m1_part7.htm) (accessed Jun. 19, 2020).
- [72] S. Thomas, B. S. P. Harshita, P. Mishra, and S. Talegaonkar, Ceramic Nanoparticles: Fabrication Methods and Applications in Drug Delivery, *Curr. Pharm. Des.*, vol. 21, no. 42, pp. 6165–6188, 2015.
- [73] R. Betancourt-Galindo, P. Y. Reyes-Rodriguez, B. A. Puente-Urbina, C. A. Avila-Orta, O. S. Rodriguez-Fernandez, G. Cadenas-Pliego, R. H. Lira-Saldivar, and L. A. Garcia-Cerda, Synthesis of copper nanoparticles by thermal decomposition and their antimicrobial properties, *J. Nanomater.*, vol. 2014, pp. 7–11, 2014.
- [74] M. Salavati-Niasari, F. Davar, and N. Mir, Synthesis and characterization of metallic copper nanoparticles via thermal decomposition, *Polyhedron*, vol. 27, no. 17, pp. 3514–3518, 2008.
- [75] C. Y. Tai, C. Te Tai, M. H. Chang, and H. S. Liu, Synthesis of magnesium hydroxide and oxide nanoparticles using a spinning disk reactor, *Ind. Eng. Chem. Res.*, vol. 46, no. 17, pp. 5536–5541, 2007.
- [76] A. Ali, H. Zafar, M. Zia, I. U. Haq, A. R. Phull, J. S. Ali, and A. Hussain, Synthesis, characterization, applications, and challenges of iron oxide nanoparticles, *Nanotechnol. Sci. Appl.*, vol. 9, pp. 49–67, 2016.
- [77] J. Estelrich, E. Escribano, J. Queralt, and M. A. Busquets, Iron oxide nanoparticles for magnetically-guided and magnetically-responsive drug delivery, *Int. J. Mol. Sci.*, vol. 16, no. 4, pp. 8070–8101, 2015.
- [78] H. Hong, J. U. Kim, and T. Kim, Effective assembly of nano-ceramic materials for high and

- anisotropic thermal conductivity in a polymer composite, *Polymers (Basel)*, vol. 9, no. 9, p. 17, 2017.
- [79] P. Ma, N. A. Siddiqui, G. Marom, and J. Kim, Dispersion and functionalization of carbon nanotubes for polymer-based nanocomposites: A review, *Compos. Part A*, vol. 41, no. 10, pp. 1345–1367, 2010.
- [80] Branson, Branson Digital Ultrasonic Baths, *Digital Ultrasonic Cleaning Baths*. Available Online: <https://branson.com/en/product-features> (accessed Jun. 20, 2020).
- [81] B. Arman, Q. An, S. N. Luo, T. G. Desai, D. L. Tonks, T. Çağın, and W. A. Goddard III, Dynamic response of phenolic resin and its carbon-nanotube composites to shock wave loading, *J. Appl. Phys.*, vol. 109.
- [82] Exakt, Three roll mills, Exakt company. Available Online: [www.exakt.de](http://www.exakt.de) (accessed Jun. 16, 2020).
- [83] Y. A. Kim, T. Hayashi, Y. Fukai, M. Endo, and M. S. Dresselhaus, Effect of ball milling on morphology of cup-stacked carbon nanotubes, *Chem. Phys. Lett.*, vol. 355, April, pp. 279–284, 2002.
- [84] J. Y. Huang, Y. H. and M. H., Highly curved carbon nanostructures produced by ball-milling, *Chem. Phys. Lett.*, vol. 303, no. April, pp. 130–134, 1999.
- [85] V. Agubra, P. Owuor, and M. Hosur, Influence of Nanoclay Dispersion Methods on the Mechanical Behavior of E-Glass/Epoxy Nanocomposites, *Nanomaterials*, vol. 3, no. 3, pp. 550–563, 2013.
- [86] K. Masenelli-Varlot, L. Chazeau, C. Gauthier, A. Bogner, and J. Y. Cavallé, The relationship between the electrical and mechanical properties of polymer-nanotube nanocomposites and their microstructure, *Compos. Sci. Technol.*, vol. 69, no. 10, pp. 1533–1539, 2009.
- [87] M. Šupová, G. S. Martynková, and K. Barabaszová, Effect of Nanofillers Dispersion in Polymer Matrices: A Review, *Sci. Adv. Mater.*, vol. 3, no. 1, pp. 1–25, 2011.
- [88] M. Okamoto, S. Morita, H. Taguchi, and Y. Hoon, Synthesis and structure of smectic

- clay/poly (methyl methacrylate) and clay/polystyrene nanocomposites via in situ intercalative polymerization, *Polymer (Guildf)*., vol. 41, no. 41, pp. 3887–3890, 2000.
- [89] Z. P. Luo and J. H. Koo, Quantification of the layer dispersion degree in polymer layered silicate nanocomposites by transmission electron microscopy, *Polymer (Guildf)*., vol. 49, no. 49, pp. 1841–1852, 2008.
- [90] L. Leibler and L. Corte, Analysis of polymer blend morphologies from transmission electron micrographs, *Polymer (Guildf)*., vol. 46, pp. 6360–6368, 2005.
- [91] D. Wu, D. Gao, S. C. Mayo, J. Gotama, and C. Way, X-ray ultramicroscopy : A new method for observation and measurement of filler dispersion in thermoplastic composites, *Compos. Sci. Technol.*, vol. 68, pp. 178–185, 2008.
- [92] M. S. Dresselhaus, G. Dresselhaus, R. Saito, and A. Jorio, Raman spectroscopy of carbon nanotubes, *Phys. Rep.*, vol. 409, no. 2, pp. 47–99, 2005.
- [93] S. H. Yum, S. H. Kim, W. Il Lee, and H. Kim, Improvement of ablation resistance of phenolic composites reinforced with low concentrations of carbon nanotubes, *Compos. Sci. Technol.*, vol. 121, pp. 16–24, 2015.
- [94] G. Savage, Carbon-Carbon composites, 1st ed., London United Kingdom: Chapman & Hall, 1993.
- [95] A. P. Mouritz, Introduction to Aerospace Materials, Philadelphia USA, Woodhead Publishing, 2012.
- [96] Y. S. Lee, E. D. Wetzel, and N. J. Wagner, The ballistic impact characteristics of Kevlar woven fabrics impregnated with a colloidal shear thickening fluid, *J. Mater. Sci.*, vol. 38, no. 13, pp. 2825–2833, 2003.
- [97] W. Huang, Y. Wu, L. Qiu, C. Dong, J. Ding, and D. Li, Tuning Rheological Performance of Silica Concentrated Shear Thickening Fluid by Using Graphene Oxide, *Adv. Condens. Matter Phys.*, vol. 2015, p. 5, 2015.
- [98] E. E. Haro, A. G. Odeshi, and J. A. Szpunar, The energy absorption behavior of hybrid composite laminates containing nano-fillers under ballistic impact, *International Journal of*

- Impact Engineering*, vol. 96. pp. 11–22, 2016.
- [99] ASTM D790-17, Standard Test Methods for Flexural Properties of Unreinforced and Reinforced Plastics and Electrical Insulating Materials, ASTM International, West Conshohocken, PA, 2017.
- [100] C. Weinong and Song Bo, Split Hopkinson (Kolsky) Bar Design, Testing and Applications. New York, USA: Springer, 2011.
- [101] K. T. Ramesh, High Rates and Impact Experiments, in *Springer Handbook of Experimental Solid Mechanics*, J. Sharpe and N. William, Eds. Springer US, 2008, pp. 929–959.
- [102] R. F. Wei, J. X. Li, G. W. Tang, and D. Q. Cang, Strength and consolidation mechanism of iron ore and coal pellets, *Ironmak. Steelmak.*, vol. 41, no. 7, pp. 514–520, 2014.
- [103] I. Poljanšek and M. Krajnc, Characterization of phenol-formaldehyde prepolymer resins by in line FT-IR spectroscopy, *Acta Chim. Slov.*, vol. 52, no. 3, pp. 238–244, 2005.
- [104] K. A. Trick and T. E. Saliba, Mechanisms of the pyrolysis of phenolic resin in a carbon/phenolic composite, *Carbon N. Y.*, vol. 33, no. 11, pp. 1509–1515, 1995.
- [105] W. O. De Souza, K. Garcia, C. F. De Avila Von Dollinger, and L. C. Pardini, Electrical behavior of carbon fiber/phenolic composite during pyrolysis, *Mater. Res.*, vol. 18, no. 6, pp. 1209–1216, 2015.
- [106] J. Zhang, G. Mei, Z. Xie, and S. Zhao, Curing mechanism of phenolic resin binder for oxide-carbon refractories, *ISIJ Int.*, vol. 56, no. 1, pp. 44–49, 2016.
- [107] G. Bhatia, R. K. Aggarwal, M. Malik, and O. P. Bahl, Conversion of phenol formaldehyde resin to glass-like carbon, *J. Mater. Sci.*, vol. 19, no. 3, pp. 1022–1028, 1984.
- [108] T. Žukas, V. Jankauskaite, K. Žukiene, and A. Baltušnikas, The influence of nanofillers on the mechanical properties of carbon fiber reinforced methyl methacrylate composite, *Mater. Sci.*, vol. 18, no. 3, pp. 250–255, 2012.
- [109] G. Foti, Silicon carbide : from amorphous to crystalline material, *Appl. Surf. Sci.*, vol. 184, pp. 20–26, 2001.
- [110] T. Muranaka, Y. Kikuchi, T. Yoshizawa, N. Shirakawa, and J. Akimitsu, Superconductivity

- in carrier-doped silicon carbide, *Sci. Technol. Adv. Mater.*, vol. 9, no. 4, p. 044204, 2008.
- [111] J. W. Anthony, R. A. Bideaux, K. W. Bladh, and M. C. Nichols, Handbook of Mineralogy, Mineralogical Society of America, Vol. 2. Chantilly, VA 20151-1110, USA: Mineral Data Publishing, 1995.
- [112] S. Ki Park, P. Nakhanivej, J. S. Yeon, K. H. Shin, W. M. Dose, M. D. Volder, J. B. Lee, H. S. Park, Electrochemical and structural evolution of structured V<sub>2</sub>O<sub>5</sub> microspheres during Li-ion intercalation, *J. Energy Chem.*, vol. 55, pp. 108–113, 2021.
- [113] D. S. Kang, S. M. Lee, S. H. Lee, and J. S. Roh, X-ray diffraction analysis of the crystallinity of phenolic res-in-derived carbon as a function of the heating rate during the carbonization process, *Carbon Lett.*, vol. 27, no. 1, pp. 108–111, 2018.
- [114] L. Lu, V. Sahajwalla, C. Kong, and D. Harris, Quantitative X-ray diffraction analysis and its application to various coals, *Carbon N. Y.*, vol. 39, no. 12, pp. 1821–1833, 2001.
- [115] A. Rahman, S. C. Zunjarrao, and R. P. Singh, Effect of degree of crystallinity on elastic properties of silicon carbide fabricated using polymer pyrolysis, *J. Eur. Ceram. Soc.*, vol. 36, no. 14, pp. 3285–3292, 2016.

## APPENDIX A

### CALIBRATION OF THE SHPB

This section focuses only on the calibration of the Split Hopkinson pressure bar (SHPB). Before assessing the impact behavior of the carbon fiber reinforced phenolic (CFRP), the SHPB was equipped with steel bars, which were used for high strain rate testing of metals. As the dynamic impact samples used in this study was CFRP and owing to the difference in behavior and morphology of CFRP and metals, the incident and transmitted bars used for the dynamic impact test of the CFRP were made of 7075-T651 aluminum alloy. Hence, the need for re-calibration of the SHPB. Working standard operating procedures (SOP) of the SHPB have been developed already by a former student of this research group; Dr. Ahmed Tihamiyu. It is pertinent to note that either with the different incident and transmitted bars from steel or aluminum, the computations of the data remains the same and the calibration of the SHPB in this study followed the same guidelines as outlined in the SOP.

#### **Calibration of SHPB to generate conversion factor of voltage to strain amplitude**

Kindly follow the SHPB procedure in section 4 of the SHPB SOP but take note of the following:

- The calibrations are conducted without the CFRP sample, however, ensure that the ends of the bars are in contact. So, at the corresponding firing pressure, the incident and transmitted bars come into contact with one another. In this study, firing pressures of 50, 60, 70, 80, 90, 100, 110, and 120 kPa were used to obtain the conversion factor of the voltage to the strain amplitude.

Data analysis to generate the conversion factor is highlighted below:

- a. Figure B.1 is a sample of an analyzed data for calibration. Follow these sequence on an excel sheet to analyze raw data generated from every calibrating impact pressures
- b. The essence of column D is to convert column A (seconds) to micro-seconds for ease of analysis.
- c. The essence of columns D, E, and F is to ensure both raw data graph (volts 1 and 2) starts from the origin (zero).
- d. Values in columns G and H are the peak (maximum) values of volts 1 and 2 (columns E and F) respectively.

- e. Once all maximum values of volts 1 and 2 have been generated, create a new excel sheet as shown in Fig. B.2
- f. As shown in Fig. B.2, strain amplitude (column G) is calculated using;  $\epsilon = \frac{1}{2} \frac{V_{st}}{C_B}$ , Where  $V_{st}$  is the striking velocity (column D) and  $C_B$ ; elastic bar wave speed of the bar material (7075-T651 aluminum alloy).
- g. The velocity of elastic waves in the bar,  $C_B$  can be calculated using equation A.1 below:

$$C_B = \sqrt{(E_B/\rho)} \quad (A.1)$$

Where elastic modulus ( $E_B$ ) for 7075-T651 aluminum alloy is given as 71 GPa and density ( $\rho$ ) is given as 2700 kg m<sup>-3</sup>.  $C_B$ , when calculated, was approximately 5128 m/s.

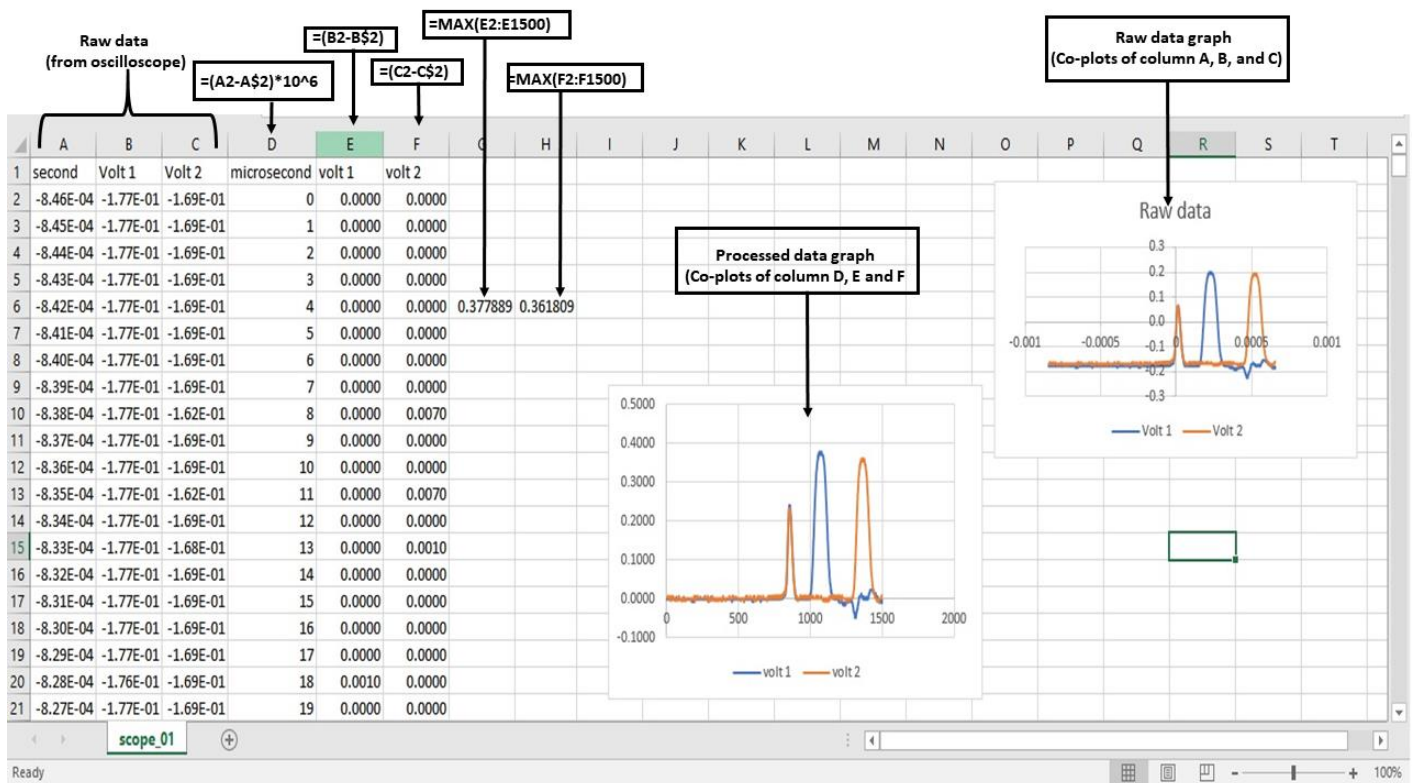


Figure A.1. Calibration raw data from oscilloscope at firing pressure of 50 kPa.

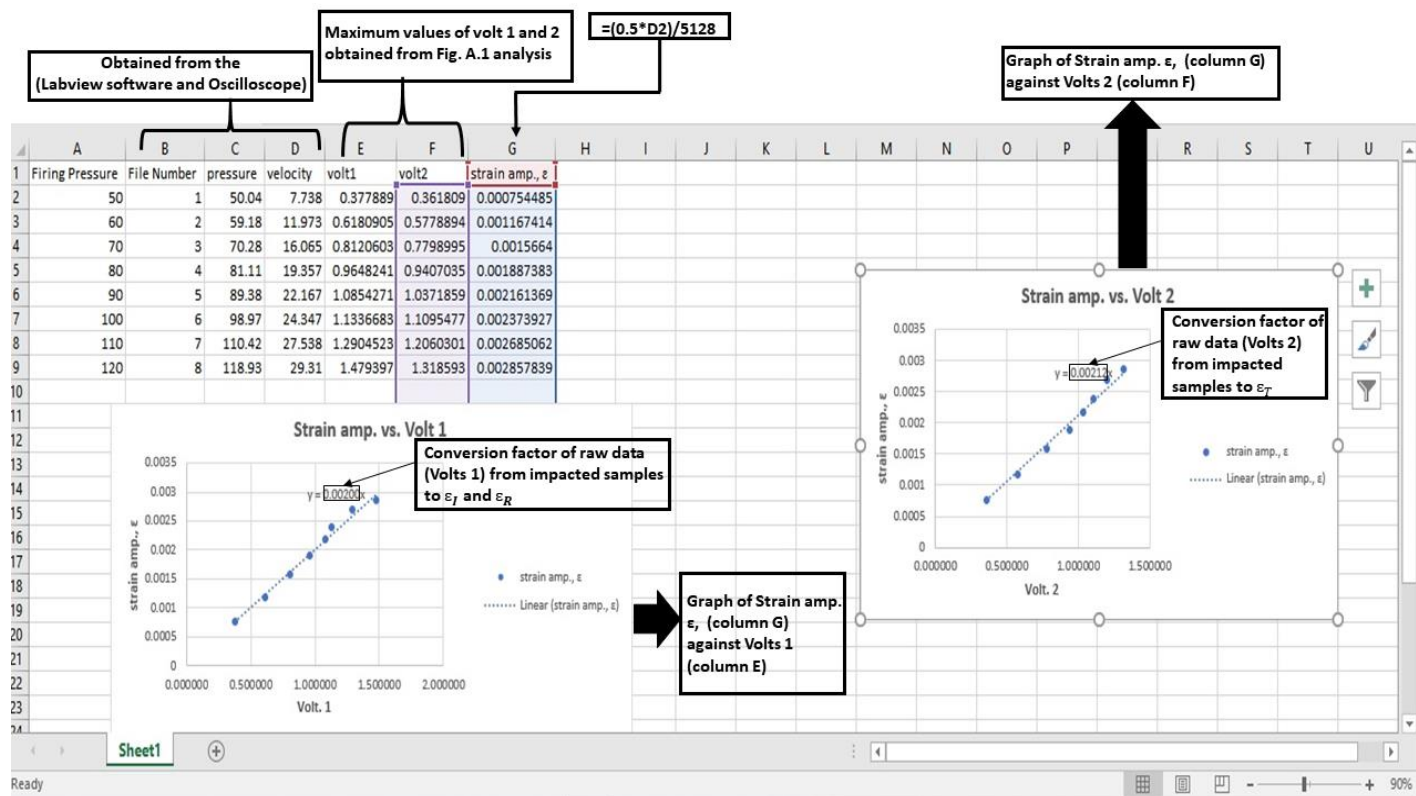


Figure A.2. Computed conversion factor of voltage to strain amplitude at different impact pressures.

After generating the conversion factor of voltage to strain amplitude for the incident, reflected and transmitted pulses. The subsequent steps as outlined in the SOP of the SHPB can be followed for the data computation.

## APPENDIX B

### RAMP AND SOAK PROGRAM OF THE AUTOCLAVE USED FOR THE CFRP

This section focuses on the ramp and soak program of the Parr 4848 reactor Autoclave, used for curing the manufactured carbon fiber reinforced phenolic (CFRP) composite. The schematics and details of the curing have been discussed in Chapter three of this thesis. The CFRP was cured by ramping at 2 °C/min from RT to 120 °C, held at 120 °C for 1 hr and cooled down to RT from 120 °C at a heating rate of 2 °C/min. However, Table B.1 explains in detail, the ramp and soak program input into the Autoclave to execute the curing of the CFRP.

Table B.1. Ramp and soak program of the CFRP used for manufacturing.

<b>Variable</b>	<b>Value</b>	<b>Meaning</b>
Ptrn	00	Pattern 0
SP00	22	Setpoint of 22 °C *Room temperature (First step is a soak by default)
tI00	00:01	Hold for 1-min
SP01	120	Setpoint of 120 °C
tI01	00:49	Ramp to setpoint in 49 min. (corresponds to a heating rate of 2 °C/min from RT to 120 °C)
SP02	120	Setpoint of 120 °C
tI02	01:00	Soak at 120 °C for 1 hr
SP03	22	Setpoint of 22 °C
tI03	00:49	Ramp to setpoint in 49 min. (corresponds to a cooling rate of 2 °C/min from 120 °C to RT)
SP04	22	Setpoint of 22 °C
tI04	00:00	
SP05	22	Setpoint of 22 °C
tI05	00:00	
SP06	22	Setpoint of 22 °C
tI06	00:00	
SP07	22	Setpoint of 22 °C

tI07	00:00	
PSy0	3	Execute steps 0-3**
CyC0	0	Do not re-cycle program
Lin0	Off	Do not execute another program upon completion

A room temperature (RT) of 22 °C was used in this study, however, this value varies based on the thermocouple reading of the Autoclave reactor. It is also pertinent to note that if the RT temperature changes, the tI01 will change and its value would depend on the heating rate used. For example, if a manufacturing process curing cycle is expected to be from RT to 150 °C with a heating rate of 2 °C/min. Assuming the thermocouple reading of the RT is 26 °C, the tI01 will be equivalent to 62 min. Kindly refer to the Standard Operating Procedure (SOP) of the Parr 4848 Autoclave reactor which I developed in conjunction with the laboratory manager, at the University of Saskatchewan Engineering Building, Room 2C24, to obtain more information that might be required.